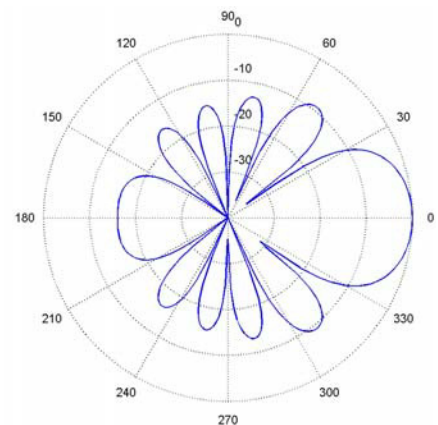
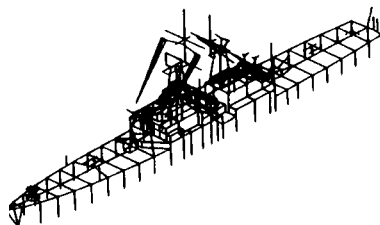
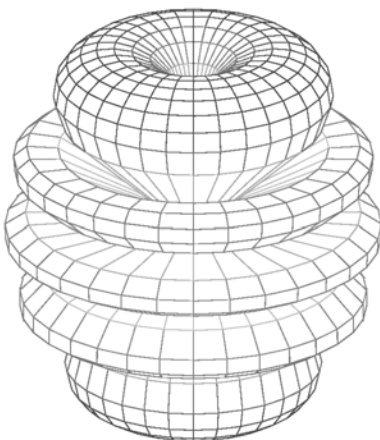
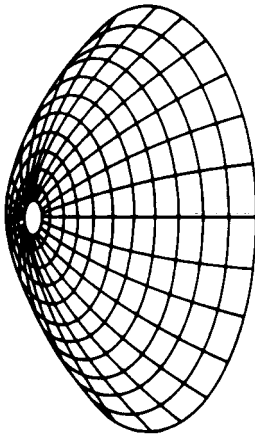
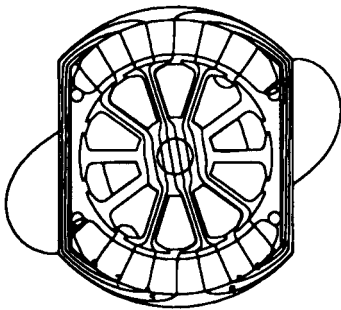
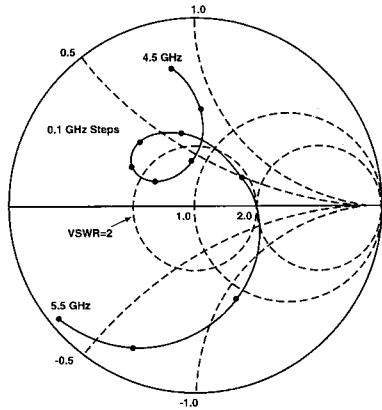


Applied Computational Electromagnetics Society Journal



Editor-in-Chief
Ataf Z. Elsherbeni

November 2004
Vol. 19 No. 3
ISSN 1054-4887

GENERAL PURPOSE AND SCOPE: The Applied Computational Electromagnetics Society (*ACES*) Journal hereinafter known as the *ACES Journal* is devoted to the exchange of information in computational electromagnetics, to the advancement of the state-of-the art, and the promotion of related technical activities. A primary objective of the information exchange is the elimination of the need to “re-invent the wheel” to solve a previously-solved computational problem in electrical engineering, physics, or related fields of study. The technical activities promoted by this publication include code validation, performance analysis, and input/output standardization; code or technique optimization and error minimization; innovations in solution technique or in data input/output; identification of new applications for electromagnetics modeling codes and techniques; integration of computational electromagnetics techniques with new computer architectures; and correlation of computational parameters with physical mechanisms.

SUBMISSIONS: The *ACES Journal* welcomes original, previously unpublished papers, relating to applied computational electromagnetics. Typical papers will represent the computational electromagnetics aspects of research in electrical engineering, physics, or related disciplines. However, papers which represent research in applied computational electromagnetics itself are equally acceptable.

Manuscripts are to be submitted through the upload system of *ACES* web site <http://aces.ee.olemiss.edu> See “Information for Authors” on inside of back cover and at *ACES* web site. For additional information contact the Editor-in-Chief:

Dr. Atef Elsherbeni

Department of Electrical Engineering
The University of Mississippi
University, MS 386377 USA
Phone: 662-915-5382 Fax: 662-915-7231
Email: atef@olemiss.edu

SUBSCRIPTIONS: All members of the Applied Computational Electromagnetics Society who have paid their subscription fees are entitled to receive the *ACES Journal* with a minimum of three issues per calendar year and are entitled to download any published journal article available at <http://aces.ee.olemiss.edu>.

Back issues, when available, are \$15 each. Subscriptions to *ACES* is through the web site. Orders for back issues of the *ACES Journal* and changes of addresses should be sent directly to *ACES* Executive Officer:

Dr. Richard W. Adler

ECE Department, Code ECAB
Naval Postgraduate School
833 Dyer Road, Room 437
Monterey, CA 93943-5121 USA
Fax: 831-649-0300
Email: rwa@attglobal.net

Allow four week’s advance notice for change of address. Claims for missing issues will not be honored because of insufficient notice or address change or loss in mail unless the Executive Officer is notified within 60 days for USA and Canadian subscribers or 90 days for subscribers in other countries, from the last day of the month of publication. For information regarding reprints of individual papers or other materials, see “Information for Authors”.

LIABILITY. Neither *ACES*, nor the *ACES Journal* editors, are responsible for any consequence of misinformation or claims, express or implied, in any published material in an *ACES Journal* issue. This also applies to advertising, for which only camera-ready copies are accepted. Authors are responsible for information contained in their papers. If any material submitted for publication includes material which has already been published elsewhere, it is the author’s responsibility to obtain written permission to reproduce such material.

APPLIED COMPUTATIONAL ELECTROMAGNETICS SOCIETY JOURNAL

Editor-in-Chief
Atef Z. Elsherbeni

November 2004
Vol. 19 No. 3

ISSN 1054-4887

The ACES Journal is abstracted in INSPEC, in Engineering Index, and in DTIC.

The first, fourth, and sixth illustrations on the front cover have been obtained from the Department of Electrical Engineering at the University of Mississippi.

The third and fifth illustrations on the front cover have been obtained from Lawrence Livermore National Laboratory.

The second illustration on the front cover has been obtained from FLUX2D software, CEDRAT S.S. France, MAGSOFT Corporation, New York.

THE APPLIED COMPUTATIONAL ELECTROMAGNETICS SOCIETY

<http://aces.ee.olemiss.edu>

ACES JOURNAL EDITORS

EDITOR-IN-CHIEF/ACES/JOURNAL

Atef Elsherbeni

University of Mississippi, EE Dept.
University, MS 38677, USA

EDITORIAL ASSISTANT

Matthew J. Inman

University of Mississippi, EE Dept.
University, MS 38677, USA

EDITOR-IN-CHIEF, EMERITUS

David E. Stein

USAF Scientific Advisory Board
Washington, DC 20330, USA

ASSOCIATE EDITOR-IN-CHIEF

Alexander Yakovlev

University of Mississippi, EE Dept.
University, MS 38677, USA

EDITOR-IN-CHIEF, EMERITUS

Ducan C. Baker

EE Dept. U. of Pretoria
0002 Pretoria, South Africa

EDITOR-IN-CHIEF, EMERITUS

Allen Glisson

University of Mississippi, EE Dept.
University, MS 38677, USA

MANAGING EDITOR

Richard W. Adler

833 Dyer Rd, Rm 437 EC/AB
NPS, Monterey, CA 93943-5121, USA

EDITOR-IN-CHIEF, EMERITUS

Robert M. Bevensee

Box 812
Alamo, CA 94507-0516, USA

EDITOR-IN-CHIEF, EMERITUS

Ahmed Kishk

University of Mississippi, EE Dept.
University, MS 38677, USA

ACES JOURNAL ASSOCIATE EDITORS

Giandomenico Amendola

Universita' della Calabria
Rende , Italy

John Beggs

NASA Langley Research Center
Hampton, VA, USA

John Brauer

Ansoft Corporation
Milwaukee, WI, USA

Magda El-Shenawee

University of Arkansas
Fayetteville AR, USA

Pat Foster

Microwave & Antenna Systems
Gt. Malvern, Worc. UK

Cynthia M. Furse

Utah State University
Logan UT, USA

Christian Hafner

Swiss Federal Inst. of Technology
Zurich, Switzerland

Michael Hamid

University of South Alabama,
Mobile, AL, USA

Andy Harrison

Radiance
Huntsville, AL

Chun-Wen Paul Huang

Anadigics, Inc.
Warren, NJ, USA

Todd H. Hubing

University of Missouri-Rolla
Rolla, MO, USA

Nathan Ida

The University of Akron
Akron, OH, USA

Yasushi Kanai

Niigata Institute of Technology
Kashiwazaki, Japan

Leo C. Kempel

Michigan State University
East Lansing MI, USA

Andrzej Krawczyk

Institute of Electrical Engineering
Warszawa, Poland

Stanley Kubina

Concordia University
Montreal, Quebec, Canada

Samir F. Mahmoud

Kuwait University
Safat, Kuwait

Ronald Marhefka

Ohio State University
Columbus, OH, USA

Edmund K. Miller

LASL
Santa Fe, NM, USA

Krishna Naishadham

Wright State University
Dayton, OH, USA

Giuseppe Pelosi

University of Florence
Florence, Italy

Vicente Rodriguez

ETS-Lindgren
Cedar Park, TX, USA

Harold A. Sabbagh

Sabbagh Associates
Bloomington, IN, USA

John B. Schneider

Washington State University
Pullman, WA, USA

Abdel Razek Sebak

University of Manitoba
Winnipeg, MB, Canada

Amr M. Sharawee

American University
Cairo, Egypt

Norio Takahashi

Okayama University
Tsushima, Japan

THE APPLIED COMPUTATIONAL ELECTROMAGNETICS SOCIETY

JOURNAL

Vol. 19 No. 3

November 2004

TABLE OF CONTENTS

“Development and Application of a Fast Multipole Method in a Hybrid FEM/MoM Field Solver” C. Guo and T. H. Hubing.....	126
“Inverse Scattering of a Dielectric Sphere Partially Buried in a Ground Plane Using a Radial Basis Function Network” C. Loo and M. Hamid.....	135
“Recent Advances in Sensitivity Analysis with Frequency-Domain Full-Wave EM Solvers” S. M. Ali, N. K. Nikolova, and M. H. Bakr.....	147
“Advanced FVTD Simulation of Dielectric Resonator Antennas and Feed Structures” C. Fumeaux, D. Baumann, and R. Vahldieck.....	155
“Analysis of a Suspended Strip in a Circular Cylindrical Waveguide” H. A. Ragheb and E. Hassan.....	165
“RCS of Two Lossy Dielectric Loaded Semi-Elliptic Channels in a Conducting Plane ” A. K. Hamid.....	170
“Design of Circular Polarized Antennas Using Genetic Algorithm Based on Curved Wire Analysis” M. A. Mangoud.....	177
“Comparison of Return Loss Calculations with Measurements of Narrow-Band Microstrip Patch Antennas” H. Abdallah, W. Wasylkiwskyj, K. Parikh, and A. Zaghloul.....	184
“Adaptive Neuro-Fuzzy Inference System for Computing the Resonant Frequency of Circular Microstrip Antennas” K. Guney and N. Sarikaya.....	188
“Modelisation of Probe Feed Excitation Using Iterative Method” H. Zairi, A. Gharsallah, A. Gharbi, and H. Baudrand.....	198

Development and Application of a Fast Multipole Method in a Hybrid FEM/MoM Field Solver

Chunlei Guo and Todd H. Hubing
 Department of Electrical and Computer Engineering
 University of Missouri-Rolla
 Rolla, MO 65409

ABSTRACT

Hybrid FEM/MoM methods combine the finite element method (FEM) and the method of moments (MoM) to model inhomogeneous unbounded problems. These two methods are coupled by enforcing the continuity of tangential fields on the boundary that separates the FEM and MoM regions. When modeling complex geometries with many elements on the boundary, the MoM part of the problem is the bottleneck of the hybrid method since it requires $O(N^2)$ memory and $O(N^3)$ computation time. This paper presents a hybrid FEM/MoM formulation applying the fast multipole method (FMM) that greatly reduces the memory requirement associated with MoM part. Two practical electromagnetic problems are presented to validate this method.

INTRODUCTION

The hybrid finite-element-method/method-of-moments (FEM/MoM) has been used to analyze a variety of electromagnetic scattering and radiation problems effectively. FEM is used to model detailed structures with complex inhomogeneities and MoM is used to model larger metallic structures and to provide an exact radiation boundary condition to terminate the FEM mesh. These two methods are coupled by enforcing tangential field continuity on the boundary separating the FEM and MoM regions. Both the FEM and MoM are powerful methods, but each of these methods has its own advantages and disadvantages. MoM handles unbounded problems very effectively but is less efficient when complex inhomogeneities are present. Inhomogeneities are easily handled by FEM. However, FEM is most suitable for bounded problems. Hence, methods that combine MoM and FEM are advantageous for treating electromagnetic problems involving unbounded, complex structures.

The FEM part of the hybrid method produces a sparse matrix, which requires $O(N)$ memory, where N is the total number of unknowns in the FEM region. On the other hand, the MoM part of

the hybrid method produces a dense matrix, which requires $O(N_s^2)$ memory and $O(N_s^3)$ CPU time, where N_s is the total number of unknowns on the MoM boundary. The final system of equations produced by the hybrid method consists of a partially full, partially sparse matrix. An iterative solver is usually preferred to solve this matrix equation. However, the computational effort primarily associated with the MoM part limits the size of the problems that can be solved.

Rokhlin introduced a fast multipole method to speed up the matrix-vector multiplication that arises in the iterative solution of MoM equations [1]. This method has been applied to electromagnetic scattering computation by Engheta [2], Lu [3], and Song [4] *et al.* The memory required for matrix-vector multiplications can be reduced from $O(N_s^2)$ in MoM to $O(N_s^{1.5})$ by using a two-level FMM, and to $O(N_s \log N_s)$ by using a multilevel version of the FMM method.

In this paper, a two-level FMM is implemented in a hybrid FEM/MoM method. Section II describes the formulation of the hybrid FEM/MoM and the related formulation using the FMM method. Preconditioning techniques to improve the condition of the resulting system of equations are also discussed. Section III presents numerical results using the FMM-enhanced hybrid FEM/MoM method.

FORMULATION

The FMM method provides an efficient technique for performing matrix-vector multiplications for MoM matrices. This section describes the hybrid FEM/MoM formulation with FMM applied to the evaluation of the MoM integrals.

The Hybrid FEM/MoM Formulation

In the hybrid FEM/MoM, an electromagnetic problem is divided into an interior equivalent part and an exterior equivalent part. The interior part is modeled using the FEM and the exterior part is

modeled using a surface integral equation method. The two equivalent parts are coupled by enforcing the continuity of tangential fields on the FEM and MoM boundaries [5].

FEM is used to analyze the interior equivalent part by solving the weak form of the vector wave equation [6]:

$$\int_V \left[\left(\frac{\nabla \times \mathbf{E}(\mathbf{r})}{j\omega\mu_0\mu_r} \right) \bullet (\nabla \times \mathbf{w}(\mathbf{r}) + j\omega\varepsilon_0\varepsilon_r\mathbf{E}(\mathbf{r}) \bullet \mathbf{w}(\mathbf{r})) \right] dV \quad (1)$$

$$= \int_S (\hat{n} \times \mathbf{H}(\mathbf{r})) \bullet \mathbf{w}(\mathbf{r}) dS - \int_V \mathbf{J}^{\text{int}}(\mathbf{r}) \bullet \mathbf{w}(\mathbf{r}) dV$$

where S is the surface enclosing volume V , $\mathbf{w}(\mathbf{r})$ is the weighting function, and \mathbf{J}^{int} is an impressed source inside volume V . A Galerkin procedure is usually used to test equation (1). The resulting FEM matrix equation has the form,

$$\begin{bmatrix} A_{ii} & A_{is} \\ A_{si} & A_{ss} \end{bmatrix} \begin{bmatrix} E_i \\ E_s \end{bmatrix} = \begin{bmatrix} 0 & 0 \\ 0 & B_{ss} \end{bmatrix} \begin{bmatrix} 0 \\ J_s \end{bmatrix} + \begin{bmatrix} g_i \\ g_s \end{bmatrix} \quad (2)$$

where $\{E_i\}$ is a set of unknowns for the electric field within the FEM volume; $\{E_s\}$ and $\{J_s\}$ are sets of unknowns for the electric field and the electric current density on the dielectric surface, respectively; A_{ii} , A_{is} , A_{si} , A_{ss} and B_{ss} are sparse coefficient matrices; and g_i and g_s are source terms.

The exterior equivalent problem can be analyzed by using an electric field integral equation (EFIE), magnetic field integral equation (MFIE), or both, i.e., combined field integral equation (CFIE). Both the EFIE and MFIE equations are prone to errors at frequencies corresponding to the resonant frequencies of the closed surface. However, proper formulation of the CFIE is free of such errors [6]. The EFIE is in the form [7],

$$\mathbf{E}^{\text{inc}}(\mathbf{r}) = \frac{1}{2} \mathbf{E}(\mathbf{r}) + \int_S [\mathbf{M}(\mathbf{r}') \times \nabla' G_0(\mathbf{r}, \mathbf{r}')] \quad (3)$$

$$+ jk_0\eta_0 \mathbf{J}(\mathbf{r}') G_0(\mathbf{r}, \mathbf{r}')$$

$$- j \frac{\eta_0}{k_0} \nabla' \bullet \mathbf{J}(\mathbf{r}') \nabla' G_0(\mathbf{r}, \mathbf{r}') dS', \quad \mathbf{r} \in S$$

where k_0 and η_0 are the wavenumber and the intrinsic wave impedance in free-space. The MFIE is the dual of the EFIE [7],

$$\mathbf{H}^{\text{inc}}(\mathbf{r}) = \frac{1}{2} \mathbf{H}(\mathbf{r}) + \int_S [-\mathbf{J}(\mathbf{r}') \times \nabla' G_0(\mathbf{r}, \mathbf{r}')] \quad (4)$$

$$+ j \frac{k_0}{\eta_0} \mathbf{M}(\mathbf{r}') G_0(\mathbf{r}, \mathbf{r}')$$

$$- j \frac{1}{k_0\eta_0} \nabla' \bullet \mathbf{M}(\mathbf{r}') \nabla' G_0(\mathbf{r}, \mathbf{r}') dS', \quad \mathbf{r} \in S.$$

The integral term in equations (3) and (4) is a principal-value integral, i.e., the singularity at $\mathbf{r} = \mathbf{r}'$ is excluded.

The equivalent currents on the boundary are represented by a series of basis functions. In this case, triangular basis functions, $\mathbf{f}(\mathbf{r})$, (RWG basis functions) were employed [8],

$$\mathbf{J}(\mathbf{r}) = \sum_{n=1}^{N_s} (J_s) \mathbf{f}_n(\mathbf{r}) \quad (5)$$

$$\mathbf{M}(\mathbf{r}) = \sum_{n=1}^{N_s} (E_s) \mathbf{f}_n(\mathbf{r}) \quad (6)$$

where N_s is the total number of unknowns on the surface S . The EFIE and MFIE in equations (3) and (4) have four different discrete forms using different testing functions [9]. Two of them, TE and NE, are described in the following sections. In both cases, the resulting MoM matrix equation has the following structure,

$$[C] [J_s] = [D] [E_s] - [F]. \quad (7)$$

The TE form

One method of discretizing the EFIE is known as the TE form (short for $\hat{t} \cdot \mathbf{E}$ where \hat{t} denotes a unit vector tangential to S). In this form, the EFIE in Equation (3) is tested using functions $\mathbf{f}(\mathbf{r})$. The elements in matrices $[C]$, $[D]$ and $[F]$ are then given by [10],

$$C_{mn} = -jk_0\eta_0 \int_{S_m} \mathbf{f}_m(\mathbf{r}) \bullet \left[\int_{S_n} \mathbf{f}_n(\mathbf{r}') G_0(\mathbf{r}, \mathbf{r}') dS' \right] dS \quad (8)$$

$$+ j \frac{\eta_0}{k_0} \int_{S_m} \nabla \bullet \mathbf{f}_m(\mathbf{r}) \left[\int_{S_n} (\nabla' \bullet \mathbf{f}_n(\mathbf{r}')) G_0(\mathbf{r}, \mathbf{r}') dS' \right] dS$$

$$D_{mn} = \int_{S_m} \mathbf{f}_m(\mathbf{r}) \bullet \left[\int_{S_n} \mathbf{f}_n(\mathbf{r}') \times \nabla' G_0(\mathbf{r}, \mathbf{r}') dS' + \frac{1}{2} \mathbf{w}_n(\mathbf{r}) \right] dS \quad (9)$$

$$F_m = \int_{S_m} \mathbf{f}_m(\mathbf{r}) \bullet \mathbf{E}^{\text{inc}}(\mathbf{r}) dS. \quad (10)$$

In equation (8), the ∇ operator has been transferred to the testing function $\mathbf{f}_m(\mathbf{r})$ so that C_{mn} has an R^{-1} singularity that can be evaluated analytically [8].

The NE form

In this form, the EFIE in Equation (3) is tested using functions $\hat{\mathbf{n}} \times \mathbf{f}(\mathbf{r})$, where $\hat{\mathbf{n}}$ is a unit normal vector pointing outward from the boundary surface. The elements in the matrices $[C]$, $[D]$ and $[F]$ are given by [10],

$$C_{mn} = -jk_0 \eta_0 \int_{S_m} \mathbf{f}_m(\mathbf{r}) \cdot \left[\hat{\mathbf{n}} \times \int_{S_n} \mathbf{f}_n(\mathbf{r}') G_0(\mathbf{r}, \mathbf{r}') dS' \right] dS \quad (11)$$

$$+ j \frac{\eta_0}{k_0} \int_{S_m} \mathbf{f}_m(\mathbf{r}) \cdot \left[\hat{\mathbf{n}} \times \int_{S_n} (\nabla' \cdot \mathbf{f}_n(\mathbf{r}')) \nabla' G_0(\mathbf{r}, \mathbf{r}') dS' \right] dS$$

$$D_{mn} = \int_{S_m} \mathbf{f}_m(\mathbf{r}) \cdot \left[\hat{\mathbf{n}} \times \int_{S_n} \mathbf{f}_n(\mathbf{r}') \times \nabla' G_0(\mathbf{r}, \mathbf{r}') dS' - \frac{1}{2} \mathbf{f}_n(\mathbf{r}) \right] dS \quad (12)$$

$$F_m = \int_{S_m} \mathbf{f}_m(\mathbf{r}) \cdot [\hat{\mathbf{n}} \times \mathbf{E}^{\text{inc}}(\mathbf{r})] dS. \quad (13)$$

The matrix elements in TH and NH forms can be derived from those in TE and NE forms.

Note that neither the FEM matrix equation (2) nor the MoM matrix equation (7) can be solved independently. They are coupled through the J_s and E_s terms. Three different formulations, the combined formulation, the inward-looking formulation and the outward-looking formulation, can be used to solve the coupled system [6], [13].

Application of the FMM Method

To apply the FMM, the N_s basis functions are divided into M localized groups, labeled by an index l , each supporting N_s/M basis functions. For nearby group pairs (l, l') , the matrix elements are calculated using the numerical evaluation of equations (8)–(13). For non-nearby groups (l, l') , let \mathbf{r}_m be the observation point, \mathbf{r}_n be the source point, \mathbf{r}_l be the center of l group which contains \mathbf{r}_m , and $\mathbf{r}_{l'}$ is the center of l' group which contains \mathbf{r}_n ,

$$\begin{aligned} \mathbf{r}_{mn} &= \mathbf{r}_m - \mathbf{r}_n \\ &= \mathbf{r}_m - \mathbf{r}_l + \mathbf{r}_l - \mathbf{r}_{l'} + \mathbf{r}_{l'} - \mathbf{r}_n \\ &= \mathbf{r}_{ll'} + \mathbf{r}_{ml} - \mathbf{r}_{nl'} \end{aligned} \quad (14)$$

For simplicity, the same subscripts used to label basis functions are employed to label the source

and observation points here. Equation (14) breaks the path from the source point \mathbf{r}_n to the observation point \mathbf{r}_m into three parts: the path from the source point to the center of the l' group, the path from the center of the l' group to the center of the l group, and the path from the center of the l group to the observation point. The scalar Green's function between the source point and the observation point can be approximated as [3],

$$\begin{aligned} G_0(\mathbf{r}_m, \mathbf{r}_n) &= \frac{e^{-jk_0 r_{mn}}}{4\pi r_{mn}} \\ &\approx \frac{-jk_0}{16\pi^2} \oint e^{-jk_0(\mathbf{r}_m - \mathbf{r}_{l'})} T_L(k_0 r_{ll'}, \hat{\mathbf{k}} \cdot \hat{\mathbf{r}}_{ll'}) d^2 \hat{\mathbf{k}} \end{aligned} \quad (15)$$

where $\oint d^2 \hat{\mathbf{k}}$ is a surface integral over a unit sphere, and

$$T_L(\kappa, \cos \theta) = \sum_{l=0}^L (-j)^l (2l+1) h_l^{(2)}(\kappa) P_l(\cos \theta) \quad (16)$$

where $h_l^{(2)}(x)$ is a spherical Hankel function of the second kind and $P_l(x)$ is a Legendre polynomial.

Substituting (15) into equations (8), (9), (11), and (12), we can get the matrix elements in TE and TH form using the approximate Green's function. These elements seem to be more complicated than their counterparts obtained using the MoM method, but they can be evaluated more efficiently.

The TE form

The elements in matrices $[C]$ and $[D]$ are approximated by,

$$\begin{aligned} C_{mn} &= -\left(\frac{k_0}{4\pi}\right)^2 \eta_0 \oint \mathbf{U}_{ml}^{C,TE} \cdot T_L(k_0 r_{ll'}, \hat{\mathbf{k}} \cdot \hat{\mathbf{r}}_{ll'}) \mathbf{V}_{nl} d^2 \hat{\mathbf{k}} \\ &\quad + \frac{\eta_0}{(2\pi)^2} \oint U_{ml}^C T_L(k_0 r_{ll'}, \hat{\mathbf{k}} \cdot \hat{\mathbf{r}}_{ll'}) \mathbf{V}_{nl} d^2 \hat{\mathbf{k}} \end{aligned} \quad (17)$$

$$D_{mn} = \left(\frac{k_0}{4\pi}\right)^2 \oint \mathbf{U}_{ml}^{D,TE} \cdot T_L(k_0 r_{ll'}, \hat{\mathbf{k}} \cdot \hat{\mathbf{r}}_{ll'}) \mathbf{V}_{nl} d^2 \hat{\mathbf{k}} \quad (18)$$

where

$$\mathbf{U}_{ml}^{C,TE} = \int_{S_m} e^{-jk_0 \cdot \mathbf{r}_m} \mathbf{f}_m(\mathbf{r}) dS \quad (19)$$

$$\mathbf{V}_{nl} = \int_{S_n} e^{jk_0 \cdot \mathbf{r}_n} \mathbf{f}_n(\mathbf{r}) dS \quad (20)$$

$$U_{ml}^C = \int_{S_m} e^{-jk_0 \cdot \mathbf{r}_{ml}} dS \quad (21)$$

$$V_{nl'} = \int_{S_n} e^{jk_0 \cdot \mathbf{r}_{nl'}} dS \quad (22)$$

$$\mathbf{U}_{ml}^{D,TE} = \hat{\mathbf{k}} \times \mathbf{U}_{ml}^{C,TE} \quad (23)$$

Equation (17) requires both a vector dot product of \mathbf{U}_{ml}^C with $\mathbf{V}_{nl'}$ and a scalar product of U_{ml}^C with $V_{nl'}$.

The NE form

Similarly, the elements in matrices $[C]$ and $[D]$ in equations (11) and (12) are given by,

$$C_{mn} = \left(\frac{k_0}{4\pi} \right)^2 \eta_0 \oint \mathbf{U}_{ml}^{C,NH} \cdot \mathbf{T}_L(k_0 \mathbf{r}_{ll'}, \hat{\mathbf{k}} \cdot \hat{\mathbf{r}}_{ll'}) \mathbf{V}_{nl'} d^2 \hat{\mathbf{k}} - \frac{j2k_0 \eta_0}{(4\pi)^2} \oint U_{ml}^{C,NH} \mathbf{T}_L(k_0 \mathbf{r}_{ll'}, \hat{\mathbf{k}} \cdot \hat{\mathbf{r}}_{ll'}) V_{nl'} d^2 \hat{\mathbf{k}} \quad (24)$$

$$D_{mn} = \left(\frac{k_0}{4\pi} \right)^2 \oint \mathbf{U}_{ml}^{D,NH} \cdot \mathbf{T}_L(k_0 \mathbf{r}_{ll'}, \hat{\mathbf{k}} \cdot \hat{\mathbf{r}}_{ll'}) \mathbf{V}_{nl'} d^2 \hat{\mathbf{k}} \quad (25)$$

where

$$\mathbf{U}_{ml}^{C,NH} = \mathbf{U}_{ml}^{C,TE} \times \hat{\mathbf{n}} \quad (26)$$

$$U_{ml}^{C,NH} = \hat{\mathbf{k}} \cdot \mathbf{U}_{ml}^{C,NH} \quad (27)$$

$$\mathbf{U}_{ml}^{D,NH} = \hat{\mathbf{k}} \times \mathbf{U}_{ml}^{C,NH} \quad (28)$$

Figure 1 illustrates how the computational complexity can be reduced by applying FMM, which applies approximate Green's functions to the evaluation of MoM integrals. In this figure, a hollow circle represents a source point, a solid circle represents an observation point, a hollow square represents a group center for a few source points, a solid square represents a group center for a few observation points, and a line that connects a circle with a circle or a square represents a matrix element resulting from the direct interaction from the two connecting objects. Using the MoM method, the four points illustrated in Fig. 1(a) generate a matrix with $4 \times 4 = 16$ elements. Using the FMM method however, every two points are grouped together, and only the group center has a one-to-one interaction with the other group centers. The matrix illustrated in Fig. 1(b) has only 12 elements since the number of one-to-one interactions is reduced. When there are more

groups and more points per group, this reduction can be much more significant.

An iterative solver based on the inward-looking formulation or the combined formulation is usually preferred for the solution of the hybrid FEM/MoM matrix equation when the FMM method is employed. The combined formulation was used in this study since it doesn't require a direct inverse of the FEM matrix.

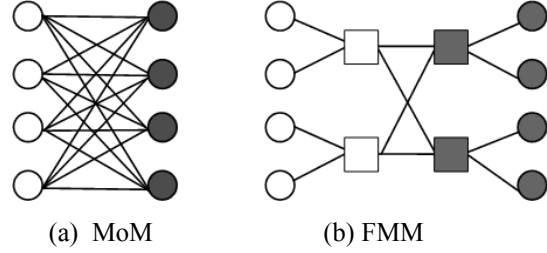


Figure 1. Computational complexity reduction by using FMM.

The hybrid FEM/MoM matrix equation employing the combined formulation is given by,

$$\begin{bmatrix} A_{ii} & A_{is} & 0 \\ A_{si} & A_{ss} & -B_{ss} \\ 0 & D & -C \end{bmatrix} \begin{bmatrix} E_i \\ E_s \\ J_s \end{bmatrix} = \begin{bmatrix} g_i \\ g_s \\ F \end{bmatrix} \quad (29)$$

In practice when the FMM method is employed, the C and D matrix elements resulting from far groups in equation (29) are not generated explicitly using equations (17), (18), (24), and (25). Instead, these equations are used to generate the matrix-vector multiplication directly [3]. So the explicit C and D matrices are sparse and contain only elements resulting from the nearby groups generated using the MoM method, denoted as C_{near} and D_{near} , respectively. Thus, the near matrix LHS' is given by

$$[LHS'] = \begin{bmatrix} A_{ii} & A_{is} & 0 \\ A_{si} & A_{ss} & -B_{ss} \\ 0 & D_{near} & -C_{near} \end{bmatrix} \quad (30)$$

Preconditioning technique

The convergence of an iterative solution is strongly dependent on the condition of the matrix and the iterative solver used. The coefficient matrices generated by hybrid FEM/MoM techniques often have very large condition numbers. Without a preconditioner, the iterative solver may converge very slowly, or not at all. A good preconditioner should be easy to construct, require little memory and improve the convergence rate significantly.

Diagonal and block diagonal preconditioners have been widely used in the past [4]. LU and incomplete LU (ILU) factorization are commonly used to construct these preconditioners [15]. Matrix LHS' in equation (30) and the preconditioner LU matrices are usually the major memory consumers for an iterative solver. Special techniques must be applied to reduce the memory requirements of the preconditioner for electrically large problems [16].

In this study, a biconjugate gradient stabilized (BICGSTAB) solver was implemented. BICGSTAB is a popular and stable Krylov subspace method for the iterative solution of linear systems. A preconditioner using the absorbing boundary condition (ABC) to provide a physical approximation of the MoM boundary was also employed [17, 18].

NUMERICAL RESULTS

EMAP5 (Electromagnetic Analysis Program Version 5) is a hybrid FEM/MoM modeling code that has been used to model signal integrity, scattering and radiation problems [19]. On a personal computer with 1 GByte of memory, EMAP5 is generally limited to the solution of problems with no more than 3600 boundary elements. The fast multipole method described in the previous section was implemented in EMAP5 in order to model larger problems. This section describes two practical examples. A commercial mesh generator was used to discretize the problems presented in this paper. Results obtained from the FMM-enhanced EMAP5 (EMAP5-FMM) are compared to results obtained using other well-established codes or analytical results.

The first sample problem is to model the input impedance of a printed circuit board (PCB) power bus structure. As shown in Fig. 2, the board dimensions are 10 cm × 8 cm × 2 mm. The top and bottom planes are perfect electric conductors (PECs). The dielectric between the PEC layers has a relative dielectric constant of 4.2 and a loss tangent of 0.02. An ideal current source is used to excite the structure at the point ($x_i = 3$ cm, $y_i = 2$ cm). The frequency range of interest is from 30 MHz to 5 GHz.

The MoM boundary was chosen to be the physical boundary of the board. The mesh density used for this problem was 12 elements per wavelength at 5 GHz. The discretization of this problem is summarized in Table 1. The total number of unknowns is given by the sum of the number of E_i , E_d , J_h and J_c elements. The TE form

is sufficient to generate a stable solution for this problem.

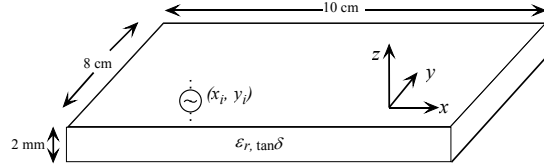


Figure 2. A PCB power bus structure.

In order to achieve a good approximation in equation (15), the size of a group should be proportional to the wavelength, so the number of groups varies with frequency. The number of groups generated for this structure at different frequencies is shown in Figure 3. At lower frequencies (e.g. below 1.5 GHz), the structure is electrically small, and the size of all groups must be much smaller than a wavelength. In this situation, the approximation in equation (15) becomes numerically unstable due to the divergent behavior of the spherical Hankel function when its order is much larger than its argument. It is invalid to use equation (15) in such cases, and all the elements must be in the same group (i.e., the matrix elements should be evaluated using MoM integrals). As the frequency increases, the wavelength decreases and the software assigns more groups to this structure. Figure 4 shows the groups of surface triangles at 5 GHz using different shades of gray to represent different groups. There are a total of 30 groups.

Table 1. Discretization of the problems

	Problem 1	Problem 2
Number of nodes	798	7,854
Number of tetrahedral elements	2,189	23,376
Number of triangles	1,580	9,186
Number of inner edges (E_i)	1,406	15,533
Number of FEM boundary edges (E_d)	144	13,779
Number of MoM boundary edges (J_h+J_c)	2,370	13,779
Total number of unknowns	3,920	43,091

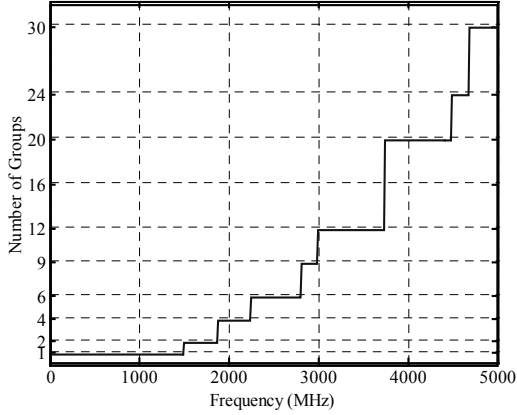


Figure 3. Number of groups at different frequencies for sample problem 1.

Groups (l, l') are defined as near groups when the following criteria are satisfied,

$$D = |\mathbf{r}_{ll'}| < 1.5 \max(d) \quad (39)$$

where D is the distance between two groups, $\max(d)$ is the maximum size of a group.

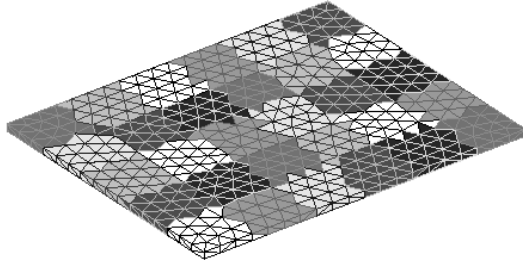


Figure 4. Mesh and groups for problem 1 at 5 GHz.

Since there are a total of 3920 unknowns in this structure, the near matrix LHS' in equation (30) can be used to build the preconditioner without exceeding the memory limit on a personal computer. Since the C and D matrices are dominated by the near group contributions evaluated using MoM, an ILU factorization on LHS' reduces the condition number of the matrix on the left hand side of equation (29) and the number of iterations significantly.

Figure 5 shows a plot of the memory required by LHS' and using ILU factorization on LHS' as a preconditioner. In this study, ILU factorization based on drop tolerance was adopted [15]. The memory required to evaluate equations (19), (20), (26), and (27) is negligible since no matrix elements are generated explicitly. The general

behavior of the memory requirement versus frequency is directly related to the number of groups shown in Fig. 3. As frequency goes up, there are more groups, and more interactions between group pairs may be evaluated using the FMM method, thus the memory required to store the near matrix is reduced. Below 2.8 GHz, although the number of groups varies from 1 to 9, the groups are so close to each other that the interaction between them has to be evaluated by the MoM integrals, so the memory required to store the near matrix is about the same. The memory required by the near matrix at 5 GHz is less than half of that required at 30 MHz. The memory required to store the ILU factorization is generally lower when the memory required by the near matrix is reduced.

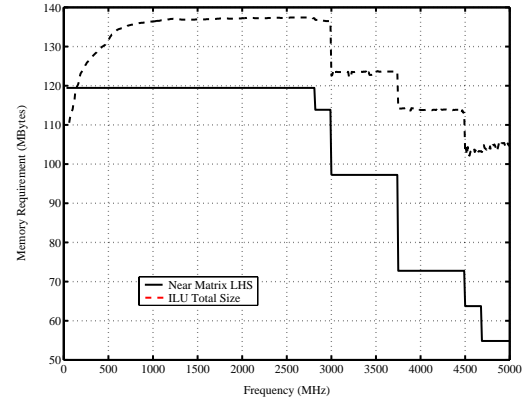


Figure 5. Memory cost of the near matrix and preconditioner.

To validate the EMAP5-FMM result, a cavity model was also used to calculate the input impedance of the same rectangular power bus structure. The cavity model has been widely used to analyze PCB power-return plane structures [20], [21]. For a thin power-return plane pair with a reasonably good dielectric and PEC conductors, the input impedance is approximately determined as,

$$Z_{in} = j\omega\mu h \sum_{m=0}^{\infty} \sum_{n=0}^{\infty} \frac{\chi_{mn}^2 \cos^2(k_{xm} x_s) \cos^2(k_{yn} y_s)}{ab(k_{xm}^2 + k_{yn}^2 + \gamma^2)}. \quad (40)$$

A more detailed explanation of equation (40) can be found in [21]. Figure 6 compares the EMAP5-FMM result with the cavity model result. Although the cavity model does not account for the radiation from printed circuit board structures, there is good agreement between the two methods up to 5 GHz.

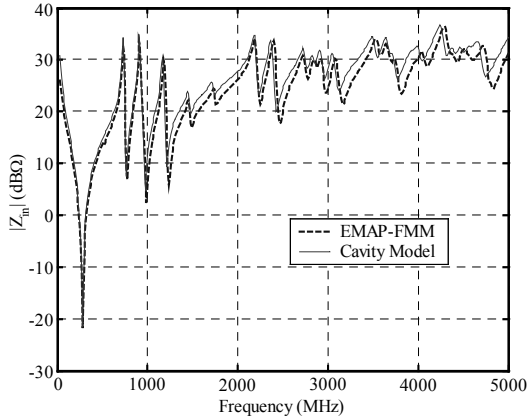


Figure 6. Input impedance comparison using EMAP5-FMM and cavity model.

The second sample problem is to calculate the bistatic radar cross section (RCS) of a perfectly conducting sphere. The radius of the sphere is 15 cm. The frequency of interest is 3 GHz. In this case, due to the large number of elements required, it is not possible to build a preconditioner from the matrix LHS' that fits in the physical memory of a personal computer. However, it is possible to construct an alternative preconditioner based on the FEM submatrix and an absorbing boundary condition (FEM-ABC) that is very memory efficient. In order to apply the ABC, the MoM boundary must be moved away from the PEC conductor and a specific CFIE form (TENH) is used [18]. An air sphere with a radius of 16 cm forms the MoM boundary, as shown in Fig. 7. More information on how to choose the location of the ABC can be found in [17].

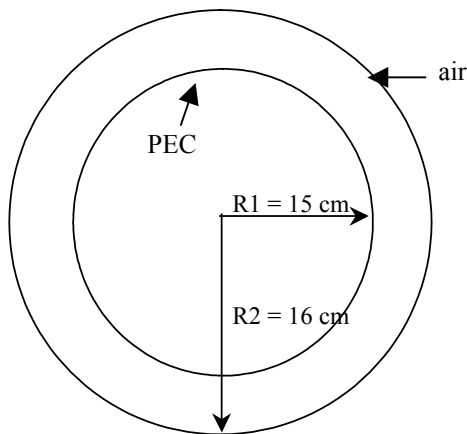


Figure 7. A perfectly conducting sphere.

Table 1 summarizes the discretization of this problem. The air layer generates 23,376 tetrahedral elements and 15,533 FEM inner edges. The triangular mesh density used for this problem is 10 elements per wavelength. If the MoM matrix is

calculated directly using the MoM method, the memory requirement for the $[C]$ and $[D]$ matrices is about 6 GBytes, which greatly exceeds the physical memory of the personal computer used for this modeling.

Figure 8 illustrates the triangular surface mesh on the air sphere. There are a total of 194 groups on the surface. Ideally, groups on the surface of a symmetric structure like a sphere would have a similar number of elements. However, the grouping algorithm that we used produced several groups with only a few elements. A better grouping algorithm would balance the number of elements in each group. Nevertheless, the FMM algorithm performed very well for these examples.

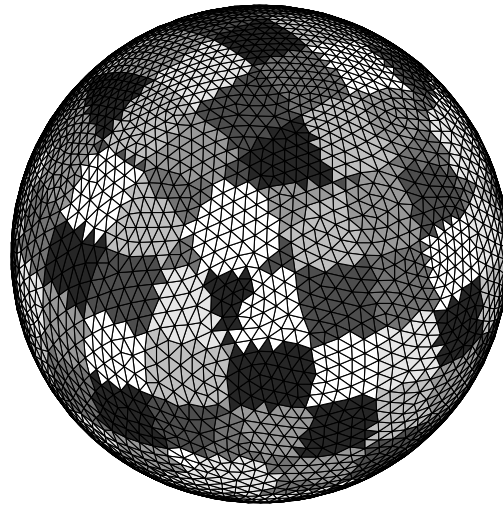


Figure 8. The meshes and groups for problem 2.

The memory required to store the near matrix LHS' in this case is about 1.2 GBytes, which is only 1/5 of that required to store the $[C]$ and $[D]$ matrices obtained by the MoM. However, this memory requirement is close to the limit of the personal computer used for this modeling. It is not possible to generate a preconditioner using ILU factorization of the near matrix LHS' on the same computer due to its huge memory requirement. Using a FEM-ABC preconditioner and techniques reported in [18], the memory required for the preconditioner is only about 0.02 GBytes and the BICGSTAB solution converges to a tolerance of 10^{-3} in 26 steps.

Analytical results for the RCS of this geometry can be obtained using the Mie series [22]. Figure 9 shows that the bistatic RCS results obtained using EMAP5-FMM agree with the Mie series results very well.

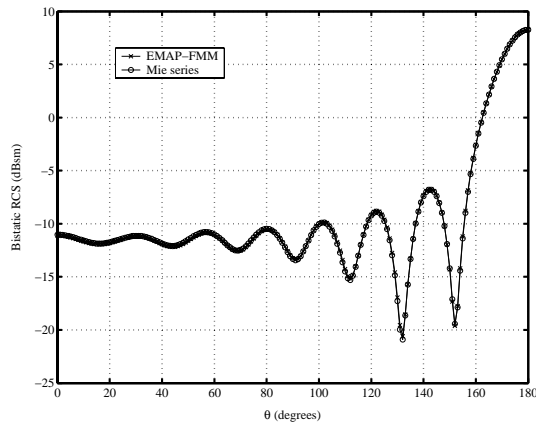


Figure 9. The bistatic RCS results of a perfect conducting sphere.

CONCLUSION

The fast multipole method was combined with a hybrid FEM/MoM method in this paper. Incorporating FMM allows an efficient evaluation of the surface integral and reduces the memory required to model structures with a large number of boundary elements. Two practical problems were investigated to validate the formulation and to demonstrate the memory efficiency of FMM. Good agreement was achieved between the FMM-enhanced hybrid FEM/MoM method and other analytical results.

For the first sample problem with 2,370 MoM boundary edges, the near matrix in the FMM employs about half of the memory required to store the fully-populated matrix generated by the MoM at 5 GHz. For the second sample problem with 13,779 MoM boundary edges, the near matrix uses about $1/5$ of the memory required to store the dense matrix generated by the MoM. If the FMM were applied to larger problems with more MoM boundary edges, we would expect even greater memory efficiency to be achieved.

Besides the near matrix, the preconditioner also usually requires a lot of memory in an iterative solver. Since the condition number of the matrices generated by the hybrid method is usually very large, the preconditioner is crucial for the efficient convergence of the iterative solver. A good preconditioner will reduce the required iterations dramatically and require very little memory and little time to construct. Without an effective preconditioner, the modeling of the second sample problem would have been much more difficult on a personal computer.

The FMM method implemented in this study does not work very well for electrically small structures due to the divergent nature of the spherical Hankel function used in this method. Electrically small structures that have many elements due to their geometric complexity are best modeled by locating the FEM/MoM boundary far from the complex part of the geometry. This minimizes the number of MoM boundary elements required and the total memory required to solve the problem.

The FMM method is designed to model electrically large structures with a large number of boundary elements. Its multilevel versions have been successfully employed to model structures such as aircraft with more than 10^7 boundary elements [11]. For electrically large geometries, a hybrid FEM/MoM technique incorporating FMM is capable of solving much larger problems in less memory than a standard FEM/MoM approach.

ACKNOWLEDGEMENT

The authors wish to express their thanks to Professor W. C. Chew of University of Illinois at Urbana-Champaign for providing the Mie series code.

REFERENCES

- [1] V. Roklin, "Rapid solution of integral equations of scattering theory in two dimensions," *J. Comput. Phys.*, vol. 86, pp. 414–439, Feb. 1990.
- [2] N. Engheta, W.D. Murphy, V. Rokhlin and M.S. Vassiliou, "The fast multipole method for electromagnetic scattering problems," *IEEE Trans. Antennas Propagat.*, vol. 40, no. 6, pp. 634–641, June 1992.
- [3] N. Lu and J. Jin, "Application of fast multipole method to finite-element boundary-integral solution of scattering problems," *IEEE Trans. Antennas Propagat.*, vol. 44, no. 6, pp. 781–786, June 1996.
- [4] J. M. Song and W.C. Chew, "MLFMA for electromagnetic scattering from large complex objects," *IEEE Trans. Antennas Propag.*, vol. 45, pp. 1488–1493, Oct. 1997.
- [5] J. L. Volakis, T. Özdemir, and J. Gong, "Hybrid finite-element methodologies for antennas and scattering," *IEEE Trans. Antennas Propagat.*, vol. 45, pp. 493–507, Mar. 1997.

- [6] A. F. Peterson, S. L. Ray, and R. Mittra, *Computational Methods for Electromagnetics*, New York: IEEE Press and Oxford University Press, 1997.
- [7] J. J. H. Wang, *Generalized Moment Methods in Electromagnetics*, New York: John Wiley & Sons, 1990.
- [8] S. M. Rao, D. R. Wilton, and A. W. Glisson, "Electromagnetic scattering by surfaces of arbitrary shape," *IEEE Trans. Antennas Propagat.*, vol. 30, pp. 409–418, May 1982.
- [9] X.-Q. Sheng, J.-M. Jin, J. Song, C.-C. Lu, and W.C. Chew, "On the formulation of hybrid finite-element and boundary-integral methods for 3-D scattering," *IEEE Trans. Antennas Propagat.*, vol. 46, pp. 303–311, Mar. 1998.
- [10] Y. Ji, "Development and applications of a hybrid finite-element method/method-of-moments tool to model electromagnetic compatibility and signal integrity problems in printed circuit boards," Ph. D. dissertation, University of Missouri-Rolla, 2000.
- [11] W. C. Chew, J.-M. Jin, E. Michielssen and J. Song, *Fast and Efficient Algorithms in Computational Electromagnetics*, Norwood, MA: Artech House Inc, 2001.
- [12] R. Coifman, V. Roklin, and S. Wandzura, "The fast multipole method for the wave equation: a pedestrian prescription," *IEEE Antennas Propag. Mag.*, vol. 35, pp. 7–12, June 1993.
- [13] Y. Ji, H. Wang and T. H. Hubing, "A novel preconditioning technique and comparison of three formulations for the hybrid FEM/MoM method," *Appl. Comput. Electromagn. Soc. (ACES) J.*, vol. 15, pp. 103–114, July 2000.
- [14] J. M. Song and W.C. Chew, "Fast multipole method solution using parametric geometry," *Micro. Opt. Tech. Lett.*, vol. 7, pp. 760–765, Nov. 1994.
- [15] Y. Saad, *Iterative Methods for Sparse Linear Systems*, Boston: PWS Publishing Company, 1996.
- [16] A. Heldring, J. M. Rius and L. Ligthart, "New block ILU preconditioner scheme for numerical analysis of very large electromagnetic problems," *IEEE Trans. Magn.*, vol. 38, no. 2, pp. 337–340, Mar. 2002.
- [17] J. Liu and J.-M. Jin, "A highly effective preconditioner for solving the finite element-boundary integral matrix equation of 3-D scattering," *IEEE Trans. Antennas Propagat.*, vol. 50, no. 9, pp. 1212–1221, Sep. 2002.
- [18] C. Guo and T. H. Hubing, "Effective preconditioners for the solution of hybrid FEM/MoM matrix equations using combined formulations", submitted to *Appl. Comput. Electromagn. Soc. (ACES) J.*
- [19] Y. Ji and T. H. Hubing, "EMAP5: A 3D hybrid FEM/MoM code," *Appl. Comput. Electromagn. Soc. (ACES) J.*, vol. 15, pp. 1–12, Mar. 2000.
- [20] Y. T. Lo, D. Solomon, and W. F. Richards, "Theory and experiment on microstrip antennas," *IEEE Trans. Antennas Propagat.*, vol. 27, no. 2, pp. 137–145, March 1979.
- [21] M. Xu and T. Hubing, "Estimating the power bus impedance of printed circuit boards with embedded capacitance," *IEEE Trans. Adv. Packag.*, vol. 25, no. 3, pp. 424–432, Aug. 2002.
- [22] W. C. Chew, *Waves and Fields in Inhomogeneous Media*, New York: IEEE Press, 1995.



Chunlie Guo earned his BSEE and MSEE degrees from Tsinghua University in 1998 and 2000, respectively. He is currently pursuing a Ph.D. degree in Electrical Engineering at the University of Missouri-Rolla. His graduate research is focused on the development of numerical modeling techniques for analyzing signal integrity and electromagnetic compatibility problems.



Todd Hubing received his BSEE degree from MIT in 1980, his MSEE degree from Purdue University in 1982, and his Ph.D. in Electrical Engineering from North Carolina State University in 1988.

From 1982 to 1989, he was an electromagnetic compatibility engineer for IBM in Research Triangle Park, NC. He is currently a Professor of Electrical and Computer Engineering at the University of Missouri-Rolla. He serves on the Board of Directors and is a Past President of the IEEE EMC Society.

Inverse Scattering of a Dielectric Sphere Partially Buried in a Ground Plane Using a Radial Basis Function Network

C. Loo and M. Hamid

University of South Alabama, Department of Electrical Engineering
Mobile, Alabama, 36688, U.S.A.

e-mail: mhamid@usouthal.edu

ABSTRACT

An analytic solution of the problem of electromagnetic scattering by a dielectric spherical scatterer resting on, or partially buried in, an infinite perfectly conducting ground plane is approximated by partially truncated sphere and is formulated using the method of images. The scattered field coefficients are solved exactly so that the scattered field can be evaluated everywhere. In particular, the scattering cross section can be calculated as a function of the sphere radius and permittivity as well as the truncated sphere distance for any specified angle of incidence. The solution of this problem is relevant to analyze the scattering by complex three-dimensional bodies, plastic mines, icebergs, rough surfaces, etc., in which the flat background can be modeled by the ground plane while the complex body can be simulated by a sphere or a system of spheres partially truncated and resting on the ground plane. In order to solve the inverse scattering problem, we employ a radial basis function network to take the scattered field complex coefficients for the TE and TM polarization case as the network inputs to predict the three outputs of the electrical radius, burial distance, and relative permittivity of the sphere. The trained network is able to retrieve the three aforementioned parameters from new data which is different from the learning data.

1. INTRODUCTION

The solution to the problem of electromagnetic inverse scattering by a partially buried dielectric sphere in an infinite plane is relevant to analyze the scattering by complex three-dimensional bodies, plastic mines, icebergs, rough surfaces, etc., in which the flat background can be modeled by the ground plane and the complex body can be simulated by a sphere or a system of spheres partially buried in the ground plane. Generally, in these applications, the detection of the dielectric characterization of the target needs to be performed directly "on field". Therefore, the development of an accurate and also fast numerical algorithm for these inverse scattering problems is essential. Analytical and numerical techniques of solving the inverse scattering problem are computationally intensive as they require matrix inversion, recurrence relations or graphical inversion methods [2-4]. In the past few years, neural network

technique has been used for solving inverse scattering problems with respect to overcoming the drawback of directly solving the inverse problem [5-8]. This technique is simple, straightforward and allows a sensible reduction in the computational time and, consequently, it permits to obtain very fast solutions. This is an interesting property for all those problems requiring an analysis performed directly "on field".

The problem of forward electromagnetic scattering by a partially buried dielectric sphere in an infinite plane using truncated sphere as an approximation has been solved by Hamid and Hamid [1] (depicted in Figure 1). They solved the problem but did not carry out their solution to the same extent as reported here. The rigorous analytic solution of the problem is formulated using the method of images. The incident wave is assumed a uniform plane electromagnetic wave of arbitrary angle of incidence. The method of images is applied to replace the partially buried sphere in a ground plane by two overlapping spheres of equal size, or by two touching spheres of equal size, if the sphere is resting on the ground plane. And a supplementary incident plane electromagnetic wave is added such that the total electric field is satisfied at all points where the ground plane is located in the original problem. The incident, supplementary and scattered fields are expressed in terms of appropriate spherical wave functions. To impose the boundary conditions on the surfaces of the spheres, the translational addition theorem for the spherical wave functions is used to express the coordinate system of the scattered field from one sphere in terms of the coordinate system of the other sphere leading to a matrix equation, which can be inverted numerically to recover the scattered field coefficients.

In this paper, we improved the solution to the aforementioned scattering problem by employing the re-derived vector translational addition coefficients functions by Xu, which are quite similar to Cruzan's formula, in order to overcome the problem associate with Cruzan's formula in producing zero value for TE case [10]. The scattered field coefficients generated by exact methods are obtained, from which the scattered field can be evaluated everywhere. In particular, the scattering cross section can be calculated as a function of the sphere radius and permittivity as well as the burial distance for any specified angle of incidence.

where $\hat{k}^i = k \sin(\pi - \alpha) \hat{x} + k \cos(\pi - \alpha) \hat{z}$

The incident plane wave can be expressed with reference to the spherical coordinate system of the sphere center O_1 as:

$$e^{jkr \cos \alpha} = \sum_{n=0}^{\infty} \sum_{m=-n}^{m=n} j^n (2n+1) \frac{(n-m)!}{(n+m)!} P_n^m(\cos \alpha) P_n^m(\cos \theta) j_n(kr) e^{jm\phi} \quad (3)$$

where P_n^m is the associated Legendre function of the first kind while j_n is the spherical Bessel function of the first kind.

Expressing the incident wave in the form of spherical wave expansion (SWE) based on scalar spherical wave mode coefficients (SSWMC) and vector spherical wave functions (VSWF), the fields due to the incident wave on the sphere are:

$$\vec{E}_i(r_1, \theta_1, \phi_1) = \sum_{n=1}^{\infty} \sum_{m=-n}^{m=n} \left[P_1(m, n) \vec{N}_{mn}^{(1)}(r_1, \theta_1, \phi_1) + Q_1(m, n) \vec{M}_{mn}^{(1)}(r_1, \theta_1, \phi_1) \right] \quad (4)$$

$$\eta \vec{H}_i(r_1, \theta_1, \phi_1) = j \sum_{n=1}^{\infty} \sum_{m=-n}^{m=n} \left[P_1(m, n) \vec{M}_{mn}^{(1)}(r_1, \theta_1, \phi_1) + Q_1(m, n) \vec{N}_{mn}^{(1)}(r_1, \theta_1, \phi_1) \right] \quad (5)$$

The fields due to the image of the incident wave on the sphere are:

$$\vec{E}_i(r_1, \theta_1, \phi_1) = \sum_{n=1}^{\infty} \sum_{m=-n}^{m=n} \left[P_2(m, n) \vec{N}_{mn}^{(1)}(r_1, \theta_1, \phi_1) + Q_2(m, n) \vec{M}_{mn}^{(1)}(r_1, \theta_1, \phi_1) \right] \quad (6)$$

$$\eta \vec{H}_i(r_1, \theta_1, \phi_1) = j \sum_{n=1}^{\infty} \sum_{m=-n}^{m=n} \left[P_2(m, n) \vec{M}_{mn}^{(1)}(r_1, \theta_1, \phi_1) + Q_2(m, n) \vec{N}_{mn}^{(1)}(r_1, \theta_1, \phi_1) \right] \quad (7)$$

The fields due to the incident wave on the image sphere are:

$$\vec{E}_i(r_2, \theta_2, \phi_2) = \sum_{n=1}^{\infty} \sum_{m=-n}^{m=n} \left[P_3(m, n) \vec{N}_{mn}^{(1)}(r_2, \theta_2, \phi_2) + Q_3(m, n) \vec{M}_{mn}^{(1)}(r_2, \theta_2, \phi_2) \right] \quad (8)$$

$$\eta \vec{H}_i(r_2, \theta_2, \phi_2) = j \sum_{n=1}^{\infty} \sum_{m=-n}^{m=n} \left[P_3(m, n) \vec{M}_{mn}^{(1)}(r_2, \theta_2, \phi_2) + Q_3(m, n) \vec{N}_{mn}^{(1)}(r_2, \theta_2, \phi_2) \right] \quad (9)$$

The fields due to the image of incident wave on image sphere are:

$$\vec{E}_i(r_2, \theta_2, \phi_2) = \sum_{n=1}^{\infty} \sum_{m=-n}^{m=n} \left[P_4(m, n) \vec{N}_{mn}^{(1)}(r_2, \theta_2, \phi_2) + Q_4(m, n) \vec{M}_{mn}^{(1)}(r_2, \theta_2, \phi_2) \right] \quad (10)$$

$$\eta \vec{H}_i(r_2, \theta_2, \phi_2) = j \sum_{n=1}^{\infty} \sum_{m=-n}^{m=n} \left[P_4(m, n) \vec{M}_{mn}^{(1)}(r_2, \theta_2, \phi_2) + Q_4(m, n) \vec{N}_{mn}^{(1)}(r_2, \theta_2, \phi_2) \right] \quad (11)$$

where $\vec{M}_{mn}^{(1)}$ and $\vec{N}_{mn}^{(1)}$ are the spherical vector wave functions of the first kind defined in terms of the spherical Bessel functions given as:

$$M_{mn} = \begin{bmatrix} \frac{m}{\sin \theta} z_n(kR) P_n^m(\cos \theta) \hat{\theta} \\ -z_n(kR) \frac{\partial}{\partial \theta} P_n^m(\cos \theta) \hat{\phi} \end{bmatrix} e^{im\phi} \quad (12)$$

$$N_{mn} = \begin{bmatrix} \frac{n(n+1)}{kR} z_n(kR) P_n^m(\cos \theta) \hat{r} \\ + \frac{1}{kR} \frac{\partial}{\partial R} [R z_n(kR)] \frac{\partial}{\partial \theta} P_n^m(\cos \theta) \hat{\theta} \\ + \frac{m}{kR \sin \theta} \frac{\partial}{\partial R} [R z_n(kR)] P_n^m(\cos \theta) \hat{\phi} \end{bmatrix} e^{im\phi} \quad (13)$$

for $M_{mn}^{(1)}$ and $N_{mn}^{(1)}$, $z_n(kR) = j_n(kR)$,

for $M_{mn}^{(3)}$ and $N_{mn}^{(3)}$, $z_n(kR) = h_n^{(1)}(kR)$,

while $P(m, n)$ and $Q(m, n)$ are known incident field coefficients for an arbitrary angle of incidence and may be written in the form:

$$P(m, n) = -j^n \frac{(2n+1)(n-m)!m}{n(n+1)(n+m)! \sin \alpha} P_n^m(\cos \alpha) \quad (14)$$

$$Q(m, n) = -j^n \frac{(2n+1)(n-m)!}{n(n+1)(n+m)!} \times \frac{\partial}{\partial \alpha} P_n^m(\cos \alpha) \quad (15)$$

$$P_1(m, n) = e^{jkd \cos \alpha} P(m, n) \quad (16)$$

$$Q_1(m, n) = e^{jkd \cos \alpha} P(m, n) \quad (17)$$

$$P_2(m, n) = (-1)^{(m+n)} e^{-jkd \cos \alpha} P(m, n) \quad (18)$$

$$Q_2(m, n) = (-1)^{(m+n)} e^{-jkd \cos \alpha} Q(m, n) \quad (19)$$

$$P_3(m, n) = e^{-jkd \cos \alpha} P(m, n) \quad (20)$$

$$Q_3(m, n) = e^{-jkd \cos \alpha} Q(m, n) \quad (21)$$

$$P_4(m, n) = (-1)^{(m+n)} e^{jkd \cos \alpha} P(m, n) \quad (22)$$

$$Q_4(m, n) = (-1)^{(m+n)} e^{jkd \cos \alpha} Q(m, n) \quad (23)$$

The scattered fields from the dielectric sphere are:

$$\vec{E}_s(r_1, \theta_1, \phi_1) = \sum_{n=1}^{\infty} \sum_{m=-n}^{m=n} \left[A_E^s(m, n) \vec{N}_{mn}^{(3)}(r_1, \theta_1, \phi_1) + A_M^s(m, n) \vec{M}_{mn}^{(3)}(r_1, \theta_1, \phi_1) \right] \quad (24)$$

$$\eta \vec{H}_s(r_1, \theta_1, \phi_1) = j \sum_{n=1}^{\infty} \sum_{m=-n}^{m=n} \left[A_E^s(m, n) \vec{M}_{mn}^{(3)}(r_1, \theta_1, \phi_1) + A_M^s(m, n) \vec{N}_{mn}^{(3)}(r_1, \theta_1, \phi_1) \right] \quad (25)$$

The scattered fields from the image sphere are:

$$\vec{E}_s(r_2, \theta_2, \phi_2) = \sum_{n=1}^{\infty} \sum_{m=-n}^{m=n} \left[B_E^s(m, n) \vec{N}_{mn}^{(3)}(r_2, \theta_2, \phi_2) + B_M^s(m, n) \vec{M}_{mn}^{(3)}(r_2, \theta_2, \phi_2) \right] \quad (26)$$

$$\eta \vec{H}_s(r_2, \theta_2, \phi_2) = j \sum_{n=1}^{\infty} \sum_{m=-n}^{m=n} \left[B_E^s(m, n) \vec{M}_{mn}^{(3)}(r_2, \theta_2, \phi_2) + B_M^s(m, n) \vec{N}_{mn}^{(3)}(r_2, \theta_2, \phi_2) \right] \quad (27)$$

The transmitted fields in the dielectric sphere are:

$$\vec{E}_t(r_1, \theta_1, \phi_1) = \sum_{n=1}^{\infty} \sum_{m=-n}^{m=n} \left[A_E^t(m, n) \vec{N}_{mn}^{(1)}(r_1, \theta_1, \phi_1) + A_M^t(m, n) \vec{M}_{mn}^{(1)}(r_1, \theta_1, \phi_1) \right] \quad (28)$$

$$\eta \vec{H}_t(r_1, \theta_1, \phi_1) = j \sum_{n=1}^{\infty} \sum_{m=-n}^{m=n} \left[A_E^t(m, n) \vec{M}_{mn}^{(1)}(r_1, \theta_1, \phi_1) + A_M^t(m, n) \vec{N}_{mn}^{(1)}(r_1, \theta_1, \phi_1) \right] \quad (29)$$

The transmitted fields in the image sphere are:

$$\vec{E}_t(r_2, \theta_2, \phi_2) = \sum_{n=1}^{\infty} \sum_{m=-n}^{m=n} \left[B_E^t(m, n) \vec{N}_{mn}^{(1)}(r_2, \theta_2, \phi_2) + B_M^t(m, n) \vec{M}_{mn}^{(1)}(r_2, \theta_2, \phi_2) \right] \quad (30)$$

$$\eta \vec{H}_t(r_2, \theta_2, \phi_2) = j \sum_{n=1}^{\infty} \sum_{m=-n}^{m=n} \left[B_E^t(m, n) \vec{M}_{mn}^{(1)}(r_2, \theta_2, \phi_2) + B_M^t(m, n) \vec{N}_{mn}^{(1)}(r_2, \theta_2, \phi_2) \right] \quad (31)$$

Note that in the transmitted fields, k is replaced by k_2 . $k_2 = \sqrt{\epsilon_r} k$, if the dielectric sphere is a perfect dielectric with no magnetic losses. To impose the boundary condition at $r_l = a$, the outgoing scattered fields from the image sphere must be expressed in terms of incoming fields to the real sphere and vice versa, hence we apply the spherical vector translational addition theorem, i. e.

$$\vec{M}_{mn}^{(3)}(r_2, \theta_2, \phi_2) = \sum_{\nu=1}^{\infty} \sum_{\mu=-\nu}^{\mu=\nu} \left[A_{\mu\nu}^{mn}(d_{12}, \theta_{12}, \phi_{12}) \vec{M}_{\mu\nu}^{(1)}(r_1, \theta_1, \phi_1) + B_{\mu\nu}^{mn}(d_{12}, \theta_{12}, \phi_{12}) \vec{N}_{\mu\nu}^{(1)}(r_1, \theta_1, \phi_1) \right] \quad (32)$$

$$\vec{N}_{mn}^{(3)}(r_2, \theta_2, \phi_2) = \sum_{\nu=1}^{\infty} \sum_{\mu=-\nu}^{\mu=\nu} \left[A_{\mu\nu}^{mn}(d_{12}, \theta_{12}, \phi_{12}) \vec{N}_{\mu\nu}^{(1)}(r_1, \theta_1, \phi_1) + B_{\mu\nu}^{mn}(d_{12}, \theta_{12}, \phi_{12}) \vec{M}_{\mu\nu}^{(1)}(r_1, \theta_1, \phi_1) \right] \quad (33)$$

$$\bar{M}_{mn}^{(3)}(r_1, \theta_1, \phi_1) = \sum_{v=1}^{\infty} \sum_{\mu=-v}^{\mu=v} (-1)^{n+v} \begin{bmatrix} A_{\mu\nu}^{mn}(d_{21}, \theta_{21}, \phi_{21}) \bar{M}_{\mu\nu}^{(1)}(r_2, \theta_2, \phi_2) \\ + B_{\mu\nu}^{mn}(d_{21}, \theta_{21}, \phi_{21}) \bar{N}_{\mu\nu}^{(1)}(r_2, \theta_2, \phi_2) \end{bmatrix} \quad (34)$$

$$\bar{N}_{mn}^{(3)}(r_1, \theta_1, \phi_1) = \sum_{v=1}^{\infty} \sum_{\mu=-v}^{\mu=v} (-1)^{n+v} \begin{bmatrix} A_{\mu\nu}^{mn}(d_{21}, \theta_{21}, \phi_{21}) \bar{N}_{\mu\nu}^{(1)}(r_2, \theta_2, \phi_2) \\ + B_{\mu\nu}^{mn}(d_{21}, \theta_{21}, \phi_{21}) \bar{M}_{\mu\nu}^{(1)}(r_2, \theta_2, \phi_2) \end{bmatrix} \quad (35)$$

where $A_{\mu\nu}^{mn}$ and $A_{\mu\nu}^{mn}$ are Xu's translation addition theorem coefficients given in the Appendix and

$$d_{12} = d_{21} = \sqrt{(x_2 - x_1)^2 + (y_2 - y_1)^2 + (z_2 - z_1)^2}$$

$$\theta_{12} = \cos^{-1} \left(\frac{z_2 - z_1}{d_{12}} \right), \quad \theta_{21} = \cos^{-1} \left(\frac{z_1 - z_2}{d_{21}} \right)$$

$$\phi_{12} = \tan^{-1} \left(\frac{y_2 - y_1}{x_2 - x_1} \right), \quad \phi_{21} = \tan^{-1} \left(\frac{y_1 - y_2}{x_1 - x_2} \right).$$

In our case, since the image sphere is always positioned below the real sphere on the conducting ground, θ_{12} , θ_{21} , ϕ_{12} , and ϕ_{21} are equal to zero and $d_{12} = -d_{21} = 2d$.

The boundary condition on the surface of the dielectric sphere and its image requires continuity of the tangential electric and magnetic field. Hence,

$$\hat{r}_1 \times \begin{bmatrix} \bar{E}_i(a, \theta, \phi_1) + \bar{E}'_i(a, \theta, \phi_1) \\ + \bar{E}_s(a, \theta, \phi_1) + \bar{E}'_s(a, \theta, \phi_1) \end{bmatrix} = \hat{r}_1 \times \bar{E}_i(a, \theta, \phi_1) \quad (36)$$

$$\hat{r}_1 \times \frac{1}{\eta_1} \begin{bmatrix} \bar{H}_i(a, \theta, \phi_1) + \bar{H}'_i(a, \theta, \phi_1) \\ + \bar{H}_s(a, \theta, \phi_1) + \bar{H}'_s(a, \theta, \phi_1) \end{bmatrix} = \hat{r}_1 \times \frac{1}{\eta_2} \bar{H}_i(a, \theta, \phi_1) \quad (37)$$

$$\hat{r}_2 \times \begin{bmatrix} \bar{E}_i(a, \theta_2, \phi_2) + \bar{E}'_i(a, \theta_2, \phi_2) \\ + \bar{E}_s(a, \theta_2, \phi_2) + \bar{E}'_s(a, \theta_2, \phi_2) \end{bmatrix} = \hat{r}_2 \times \bar{E}_i(a, \theta_2, \phi_2) \quad (38)$$

$$\hat{r}_2 \times \frac{1}{\eta_1} \begin{bmatrix} \bar{H}_i(a, \theta_2, \phi_2) + \bar{H}'_i(a, \theta_2, \phi_2) \\ + \bar{H}_s(a, \theta_2, \phi_2) + \bar{H}'_s(a, \theta_2, \phi_2) \end{bmatrix} = \hat{r}_2 \times \frac{1}{\eta_2} \bar{H}_i(a, \theta_2, \phi_2) \quad (39)$$

where \hat{r}_1 and \hat{r}_2 are the outward unit normal to the surface of the dielectric sphere and its image, respectively. From the boundary condition above, the electric and magnetic fields on the surface of the sphere and its image can be expressed as:

$$\bar{E}^{Total}(a, \theta, \phi) = \bar{E}_i(a, \theta, \phi) + \bar{E}'_i(a, \theta, \phi) + \bar{E}_s(a, \theta, \phi) + \bar{E}'_s(a, \theta, \phi) \quad (40)$$

$$\bar{H}^{Total}(a, \theta, \phi) = \bar{H}_i(a, \theta, \phi) + \bar{H}'_i(a, \theta, \phi) + \bar{H}_s(a, \theta, \phi) + \bar{H}'_s(a, \theta, \phi) \quad (41)$$

and

$$\bar{E}^{Total}(a, \theta', \phi') = \bar{E}_i(a, \theta', \phi') + \bar{E}'_i(a, \theta', \phi') + \bar{E}_s(a, \theta', \phi') + \bar{E}'_s(a, \theta', \phi') \quad (42)$$

$$\bar{H}^{Total}(a, \theta', \phi') = \bar{H}_i(a, \theta', \phi') + \bar{H}'_i(a, \theta', \phi') + \bar{H}_s(a, \theta', \phi') + \bar{H}'_s(a, \theta', \phi') \quad (43)$$

From the boundary condition 1, we have:

$$\hat{r}_1 \times \sum_{n=1}^{\infty} \sum_{m=-n}^{m=n} \begin{bmatrix} \left\{ P_1(m, n) \bar{N}_{mn}^{(1)}(a, \theta_1, \phi_1) + Q_1(m, n) \bar{M}_{mn}^{(1)}(a, \theta_1, \phi_1) \right\} \\ + \left\{ P_2(m, n) \bar{N}_{mn}^{(1)}(a, \theta_1, \phi_1) + Q_2(m, n) \bar{M}_{mn}^{(1)}(a, \theta_1, \phi_1) \right\} \\ + \left\{ A_E^s(m, n) \bar{N}_{mn}^{(3)}(a, \theta_1, \phi_1) + A_M^s(m, n) \bar{M}_{mn}^{(3)}(a, \theta_1, \phi_1) \right\} + \\ \left. \left. \left. \left. B_E^s(m, n) \sum_{v=1}^{\infty} \sum_{\mu=-v}^{\mu=v} \left[A_{\mu\nu}^{mn}(d_{12}, \theta_{12}, \phi_{12}) \bar{N}_{\mu\nu}^{(1)}(a, \theta_1, \phi_1) \right] \right. \right. \right. \right. \\ \left. \left. \left. \left. + B_{\mu\nu}^{mn}(d_{12}, \theta_{12}, \phi_{12}) \bar{M}_{\mu\nu}^{(1)}(a, \theta_1, \phi_1) \right] \right. \right. \right. \\ \left. \left. \left. \left. + B_M^s(m, n) \sum_{v=1}^{\infty} \sum_{\mu=-v}^{\mu=v} \left[A_{\mu\nu}^{mn}(d_{12}, \theta_{12}, \phi_{12}) \bar{M}_{\mu\nu}^{(1)}(a, \theta_1, \phi_1) \right] \right. \right. \right. \\ \left. \left. \left. \left. + B_{\mu\nu}^{mn}(d_{12}, \theta_{12}, \phi_{12}) \bar{N}_{\mu\nu}^{(1)}(a, \theta_1, \phi_1) \right] \right. \right. \right. \end{bmatrix}$$

$$= \hat{r}_1 \times \sum_{n=1}^{\infty} \sum_{m=-n}^{m=n} \left[A_E^s(m, n) \bar{N}_{mn}^{(1)}(a, \theta_1, \phi_1) + A_M^s(m, n) \bar{M}_{mn}^{(1)}(a, \theta_1, \phi_1) \right] \quad (44)$$

From the boundary condition 2, we have:

$$\hat{r}_1 \times \frac{1}{\eta_1} \sum_{n=1}^{\infty} \sum_{m=-n}^{m=n} \left\{ \begin{aligned} & \left\{ P_1(m, n) \bar{M}_{mn}^{(1)}(a, \theta_1, \phi_1) + Q_1(m, n) \bar{N}_{mn}^{(1)}(a, \theta_1, \phi_1) \right\} \\ & + \left\{ P_2(m, n) \bar{M}_{mn}^{(1)}(a, \theta_1, \phi_1) + Q_2(m, n) \bar{N}_{mn}^{(1)}(a, \theta_1, \phi_1) \right\} \\ & + \left\{ A_E^s(m, n) \bar{M}_{mn}^{(3)}(a, \theta_1, \phi_1) + A_M^s(m, n) \bar{N}_{mn}^{(3)}(a, \theta_1, \phi_1) \right\} + \\ & \left. \left. \left. \left. B_E^s(m, n) \sum_{v=1}^{\infty} \sum_{\mu=-v}^{\mu=v} \left[A_{\mu\nu}^{mn}(d_{12}, \theta_{12}, \phi_{12}) \bar{M}_{\mu\nu}^{(1)}(a, \theta_1, \phi_1) \right] \right. \right. \right. \right. \\ & \left. \left. \left. \left. + B_{\mu\nu}^{mn}(d_{12}, \theta_{12}, \phi_{12}) \bar{N}_{\mu\nu}^{(1)}(a, \theta_1, \phi_1) \right] \right. \right. \right. \\ & \left. \left. \left. \left. + B_M^s(m, n) \sum_{v=1}^{\infty} \sum_{\mu=-v}^{\mu=v} \left[A_{\mu\nu}^{mn}(d_{12}, \theta_{12}, \phi_{12}) \bar{N}_{\mu\nu}^{(1)}(a, \theta_1, \phi_1) \right] \right. \right. \right. \\ & \left. \left. \left. \left. + B_{\mu\nu}^{mn}(d_{12}, \theta_{12}, \phi_{12}) \bar{M}_{\mu\nu}^{(1)}(a, \theta_1, \phi_1) \right] \right. \right. \right. \end{aligned} \right\} \quad (45)$$

From the boundary condition 3, we have:

$$\hat{r}_2 \times \sum_{n=1}^{\infty} \sum_{m=-n}^{m=n} \left\{ \begin{aligned} & \left\{ P_3(m, n) \bar{N}_{mn}^{(1)}(a, \theta_2, \phi_2) + Q_3(m, n) \bar{M}_{mn}^{(1)}(a, \theta_2, \phi_2) \right\} \\ & + \left\{ P_4(m, n) \bar{N}_{mn}^{(1)}(a, \theta_2, \phi_2) + Q_4(m, n) \bar{M}_{mn}^{(1)}(a, \theta_2, \phi_2) \right\} \\ & + \left\{ B_E^s(m, n) \bar{N}_{mn}^{(3)}(a, \theta_2, \phi_2) + B_M^s(m, n) \bar{M}_{mn}^{(3)}(a, \theta_2, \phi_2) \right\} + \\ & \left. \left. \left. \left. A_E^s(m, n) \sum_{v=1}^{\infty} \sum_{\mu=-v}^{\mu=v} (-1)^{n+v} \left[A_{\mu\nu}^{mn}(d_{21}, \theta_{21}, \phi_{21}) \bar{N}_{\mu\nu}^{(1)}(a, \theta_2, \phi_2) \right] \right. \right. \right. \right. \\ & \left. \left. \left. \left. + B_{\mu\nu}^{mn}(d_{21}, \theta_{21}, \phi_{21}) \bar{M}_{\mu\nu}^{(1)}(a, \theta_2, \phi_2) \right] \right. \right. \right. \\ & \left. \left. \left. \left. + A_M^s(m, n) \sum_{v=1}^{\infty} \sum_{\mu=-v}^{\mu=v} (-1)^{n+v} \left[A_{\mu\nu}^{mn}(d_{21}, \theta_{21}, \phi_{21}) \bar{M}_{\mu\nu}^{(1)}(a, \theta_2, \phi_2) \right] \right. \right. \right. \\ & \left. \left. \left. \left. + B_{\mu\nu}^{mn}(d_{21}, \theta_{21}, \phi_{21}) \bar{N}_{\mu\nu}^{(1)}(a, \theta_2, \phi_2) \right] \right. \right. \right. \end{aligned} \right\} \quad (46)$$

From the boundary condition 4, we have:

$$\hat{r}_2 \times \frac{1}{\eta_1} \sum_{n=1}^{\infty} \sum_{m=-n}^{m=n} \left\{ \begin{aligned} & \left\{ P_3(m, n) \bar{M}_{mn}^{(1)}(a, \theta_2, \phi_2) + Q_3(m, n) \bar{N}_{mn}^{(1)}(a, \theta_2, \phi_2) \right\} \\ & + \left\{ P_4(m, n) \bar{M}_{mn}^{(1)}(a, \theta_2, \phi_2) + Q_4(m, n) \bar{N}_{mn}^{(1)}(a, \theta_2, \phi_2) \right\} \\ & + \left\{ B_E^s(m, n) \bar{M}_{mn}^{(3)}(a, \theta_2, \phi_2) + B_M^s(m, n) \bar{N}_{mn}^{(3)}(a, \theta_2, \phi_2) \right\} + \\ & \left. \left. \left. \left. A_E^s(m, n) \sum_{v=1}^{\infty} \sum_{\mu=-v}^{\mu=v} (-1)^{n+v} \left[A_{\mu\nu}^{mn}(d_{21}, \theta_{21}, \phi_{21}) \bar{M}_{\mu\nu}^{(1)}(a, \theta_2, \phi_2) \right] \right. \right. \right. \right. \\ & \left. \left. \left. \left. + B_{\mu\nu}^{mn}(d_{21}, \theta_{21}, \phi_{21}) \bar{N}_{\mu\nu}^{(1)}(a, \theta_2, \phi_2) \right] \right. \right. \right. \\ & \left. \left. \left. \left. + A_M^s(m, n) \sum_{v=1}^{\infty} \sum_{\mu=-v}^{\mu=v} (-1)^{n+v} \left[A_{\mu\nu}^{mn}(d_{21}, \theta_{21}, \phi_{21}) \bar{N}_{\mu\nu}^{(1)}(a, \theta_2, \phi_2) \right] \right. \right. \right. \\ & \left. \left. \left. \left. + B_{\mu\nu}^{mn}(d_{21}, \theta_{21}, \phi_{21}) \bar{M}_{\mu\nu}^{(1)}(a, \theta_2, \phi_2) \right] \right. \right. \right. \end{aligned} \right\} \quad (47)$$

Applying the orthogonality properties of the spherical wave functions yields the solution for the scattered field coefficients

$$A_E^s(m, n) = \nu_n(\alpha) \left\{ \begin{aligned} & P_1(m, n) + P_2(m, n) \\ & + \sum_{v=1}^{\infty} \sum_{\mu=-v}^{\mu=v} \left[A_{\mu\nu}^{mn}(d_{12}, \theta_{12}, \phi_{12}) B_E^s(\mu, \nu) \right] \\ & + \sum_{v=1}^{\infty} \sum_{\mu=-v}^{\mu=v} \left[B_{\mu\nu}^{mn}(d_{12}, \theta_{12}, \phi_{12}) B_M^s(\mu, \nu) \right] \end{aligned} \right\} \quad (48)$$

$$A_M^s(m, n) = u_n(\alpha) \left\{ \begin{aligned} & Q_1(m, n) + Q_2(m, n) \\ & + \sum_{v=1}^{\infty} \sum_{\mu=-v}^{\mu=v} \left[A_{\mu\nu}^{mn}(d_{12}, \theta_{12}, \phi_{12}) B_M^s(\mu, \nu) \right] \\ & + \sum_{v=1}^{\infty} \sum_{\mu=-v}^{\mu=v} \left[B_{\mu\nu}^{mn}(d_{12}, \theta_{12}, \phi_{12}) B_E^s(\mu, \nu) \right] \end{aligned} \right\} \quad (49)$$

$$B_E^s(m, n) = \nu_n(\alpha) \left\{ \begin{aligned} & P_3(m, n) + P_4(m, n) + \\ & \sum_{v=1}^{\infty} \sum_{\mu=-v}^{\mu=v} (-1)^{n+v} \left[A_{\mu\nu}^{mn}(d_{21}, \theta_{21}, \phi_{21}) A_E^s(\mu, \nu) \right] \\ & + \sum_{v=1}^{\infty} \sum_{\mu=-v}^{\mu=v} \left[B_{\mu\nu}^{mn}(d_{21}, \theta_{21}, \phi_{21}) A_M^s(\mu, \nu) \right] \end{aligned} \right\} \quad (50)$$

$$B_M^s(m, n) = u_n(\alpha) \left\{ \begin{aligned} & Q_3(m, n) + Q_4(m, n) + \\ & \sum_{v=1}^{\infty} \sum_{\mu=-v}^{\mu=v} (-1)^{n+v} \left[A_{\mu\nu}^{mn}(d_{21}, \theta_{21}, \phi_{21}) A_M^s(\mu, \nu) \right] \\ & + \sum_{v=1}^{\infty} \sum_{\mu=-v}^{\mu=v} \left[B_{\mu\nu}^{mn}(d_{21}, \theta_{21}, \phi_{21}) A_E^s(\mu, \nu) \right] \end{aligned} \right\} \quad (51)$$

where $v_n(\alpha)$ and $u_n(\alpha)$ are the electric and magnetic scattering coefficients for a single dielectric sphere, which are given by

$$v_n(ka) = -\frac{j_n(mka)[ka j_n(ka)]' - j_n(ka)[mka j_n(mka)]'}{j_n(mka)[ka h_n^{(1)}(ka)]' - h_n^{(1)}(ka)[mka j_n(mka)]'} \quad (52)$$

$$u_n(ka) = -\frac{j_n(ka)[mka j_n(mka)]' - m^2 j_n(mka)[ka j_n(ka)]'}{h_n^{(1)}(ka)[mka j_n(mka)]' - m^2 j_n(mka)[ka h_n^{(1)}(ka)]'} \quad (53)$$

where $ka = 2\pi a / \lambda$ and $m = k_2 / k = \sqrt{\epsilon_2 / \epsilon}$ is the refractive index of the dielectric, which may be real or complex depending on whether the dielectric is lossless or lossy, while ϵ_2 and ϵ are the permittivities of the sphere and the surrounding medium, respectively. Equations (48) to (51) above can be written in matrix form as

$$[A_E^S] = v_n(P_1 + P_2) + v_n[A^{12}][B_E^S] + v_n[B^{12}][B_M^S] \quad (54)$$

$$[A_M^S] = u_n(Q_1 + Q_2) + u_n[A^{12}][B_M^S] + u_n[B^{12}][B_E^S] \quad (55)$$

$$[B_E^S] = v_n(P_3 + P_4) + v_n[A^{21}][A_E^S] + v_n[B^{21}][A_M^S] \quad (56)$$

$$[B_M^S] = u_n(Q_3 + Q_4) + u_n[A^{21}][A_M^S] + u_n[B^{21}][A_E^S] \quad (57)$$

Equations (54) to (57) are a set of complex linear algebraic equations, and should be solved simultaneously to yield the unknown scattering coefficients. The above system may be rewritten in the following form

$$\begin{bmatrix} -I & 0 & v_n[A^{12}] & v_n[B^{12}] \\ 0 & -I & u_n[B^{12}] & u_n[A^{12}] \\ v_n[A^{21}] & v_n[B^{21}] & -I & 0 \\ u_n[B^{21}] & u_n[A^{21}] & 0 & -I \end{bmatrix} \begin{bmatrix} [A_E^S] \\ [A_M^S] \\ [B_E^S] \\ [B_M^S] \end{bmatrix} = \begin{bmatrix} v_n(P_1 + P_2) \\ u_n(Q_1 + Q_2) \\ v_n(P_3 + P_4) \\ u_n(Q_3 + Q_4) \end{bmatrix} \quad (58)$$

where $[A^{12}]$, $[A^{21}]$, $[B^{12}]$ and $[B^{21}]$ are matrices associated with the translation addition coefficients. And $[A_E^S]$, $[A_M^S]$, $[B_E^S]$ and $[B_M^S]$ are column matrices containing the scattering coefficients. The above equation can now be solved directly by either using Cramer's rule or by multiplication of the inverse matrix of the diagonal matrix on the left side of equation (58). In addition, the infinite series must be truncated to a finite number of terms $n = \nu = M$ and $m = \mu = 2M + 1$. Solution of equation (58) yields the scattered coefficients in equations (24), (25), (26), and (27). For our case of θ_{pq} and ϕ_{pq} equal to zero, the above system ($\mu = m$) could be solved for each m independently, since there is no coupling between azimuthal modes. Once the scattered field coefficients are computed, the total scattered field can be determined everywhere from the expressions:

$$\vec{E}_{Total}^S(r_1, \theta_1, \phi_1) = \sum_{n=1}^{\infty} \sum_{m=-n}^{m=n} \begin{bmatrix} P_2(m, n) \bar{N}_{mn}^{(3)}(r_1, \theta_1, \phi_1) \\ + Q_2(m, n) \bar{N}_{mn}^{(3)}(r_1, \theta_1, \phi_1) \\ + A_E^S(m, n) \bar{M}_{mn}^{(3)}(r_1, \theta_1, \phi_1) \\ + A_M^S(m, n) \bar{M}_{mn}^{(3)}(r_1, \theta_1, \phi_1) \\ + B_E^S(m, n) \bar{N}_{mn}^{(3)}(r_2, \theta_2, \phi_2) \\ + B_M^S(m, n) \bar{M}_{mn}^{(3)}(r_2, \theta_2, \phi_2) \end{bmatrix} \quad (65)$$

$$\eta \vec{H}_{Total}^S(r_1, \theta_1, \phi_1) = j \sum_{n=1}^{\infty} \sum_{m=-n}^{m=n} \begin{bmatrix} P_2(m, n) \bar{M}_{mn}^{(3)}(r_1, \theta_1, \phi_1) \\ + Q_2(m, n) \bar{N}_{mn}^{(3)}(r_1, \theta_1, \phi_1) \\ + A_E^S(m, n) \bar{M}_{mn}^{(3)}(r_1, \theta_1, \phi_1) \\ + A_M^S(m, n) \bar{N}_{mn}^{(3)}(r_1, \theta_1, \phi_1) \\ + B_E^S(m, n) \bar{M}_{mn}^{(3)}(r_2, \theta_2, \phi_2) \\ + B_M^S(m, n) \bar{N}_{mn}^{(3)}(r_2, \theta_2, \phi_2) \end{bmatrix} \quad (66)$$

3. FAR-FIELD APPROXIMATIONS

As shown in the previous section, both of the individual scattered fields from component spheres are solved in respective sphere-centered coordinate systems. Following the solution of boundary conditions for all partial scattering coefficients, the next step is to construct a single-field representation for the total scattered field from an aggregate of two spheres as a whole. This step is important for navigating towards a complete two-sphere scattering solution. Of particular interest are the far zone scattered fields. In the far field approximation ($kr_1 \gg 1$, and $kr_2 \gg 1$) we have,

$$r_1 = r + d \cos \theta, \quad r_2 = r - d \cos \theta \quad (67)$$

$$\theta \approx \theta_1 \approx \theta_2 \quad (68)$$

$$h_n^{(1)}(kr_1) \approx (-j)^{(n+1)} \frac{e^{jkr_1}}{kr_1}, \quad h_n^{(1)}(kr_2) \approx (-j)^{(n+1)} \frac{e^{jkr_2}}{kr_2} \quad (69)$$

$$\frac{[kr_1 h_n^{(1)}(kr_1)]'}{kr_1} \approx (-j)^n \frac{e^{jkr_1}}{kr_1}, \quad \frac{[kr_2 h_n^{(1)}(kr_2)]'}{kr_2} \approx (-j)^n \frac{e^{jkr_2}}{kr_2} \quad (70)$$

Referring to a common coordinate centered at O as shown in Fig. 1, the total scattered field can also be expanded in VSWF with a very simple transformation involving only a simple phase term. This is because the translation of VSWF between displaced coordinate systems has an obviously correct asymptotic form valid in the far zone:

$$M_{mn}^{(3)}(r_1, \theta_1, \phi_1) = e^{jkd \cos \theta} M_{mn}^{(3)}(r, \theta, \phi), \quad r \rightarrow \infty \quad (71)$$

$$N_{mn}^{(3)}(r_1, \theta_1, \phi_1) = e^{jkd \cos \theta} N_{mn}^{(3)}(r, \theta, \phi), \quad r \rightarrow \infty \quad (72)$$

$$M_{mn}^{(3)}(r_2, \theta_2, \phi_2) = e^{-jkd \cos \theta} M_{mn}^{(3)}(r, \theta, \phi), \quad r \rightarrow \infty \quad (73)$$

$$N_{mn}^{(3)}(r_2, \theta_2, \phi_2) = e^{-jkd \cos \theta} N_{mn}^{(3)}(r, \theta, \phi), \quad r \rightarrow \infty. \quad (74)$$

Substituting the above equations into equations (24) and (26), and summing both equations together yields the total scattered electric field in the far zone.

$$E_{Total}^S = \frac{e^{jkr}}{kr} \left\{ \begin{aligned} & [F_{\theta_1}(\theta, \phi) + F_{\theta_2}(\theta, \phi) + F_{\theta_3}(\theta, \phi)] \hat{\theta} \\ & + [F_{\phi_1}(\theta, \phi) + F_{\phi_2}(\theta, \phi) + F_{\phi_3}(\theta, \phi)] \hat{\phi} \end{aligned} \right\} \quad (75)$$

where

$$F_{\theta_1}(\theta, \phi) = \sum_{n=1}^{\infty} \sum_{m=-n}^n j^{-n+1} \begin{bmatrix} -P(m, n) \frac{\partial}{\partial \theta} P_n^m(\cos \theta) \\ + Q(m, n) \frac{m}{\sin \theta} P_n^m(\cos \theta) \end{bmatrix} \cos m \phi \quad (76)$$

$$F_{\phi_1}(\theta, \phi) = \sum_{n=1}^{\infty} \sum_{m=-n}^n j^{-n+1} \begin{bmatrix} P(m, n) \frac{m}{\sin \theta} P_n^m(\cos \theta) \\ + Q(m, n) \frac{\partial}{\partial \theta} P_n^m(\cos \theta) \end{bmatrix} \sin m \phi \quad (77)$$

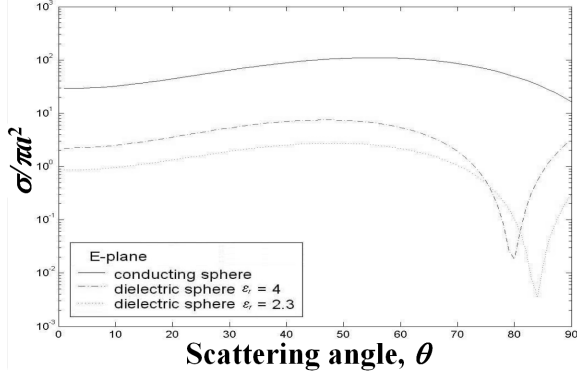


Fig. 3. Normalized bistatic cross-sections in the E plane of a partially buried dielectric sphere vs. the scattering angle θ for $ka = 1.0$, $d = a$, and $\epsilon_r = \infty, 4, 2.3$.

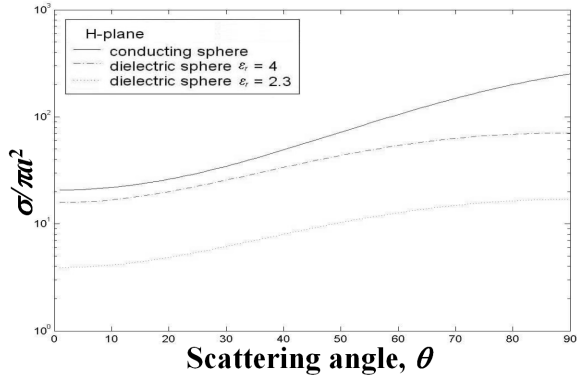


Fig. 4. Normalized bistatic cross-sections in the H plane of a partially buried dielectric sphere vs. the scattering angle θ for $ka = 1.0$, $d = a$, and $\epsilon_r = \infty, 4, 2.3$.

$$F_{\theta 2}(\theta, \phi) = \sum_{n=1}^{\infty} \sum_{m=-n}^n j^{-n+1} \left[\begin{array}{l} -A_E^S(m, n) \frac{\partial}{\partial \theta} P_n^m(\cos \theta) \\ + A_M^S(m, n) \frac{m}{\sin \theta} P_n^m(\cos \theta) \end{array} \right] \cos m\phi e^{jkd \cos \theta} \quad (78)$$

$$F_{\phi 2}(\theta, \phi) = \sum_{n=1}^{\infty} \sum_{m=-n}^n j^{-n+1} \left[\begin{array}{l} A_E^S(m, n) \frac{m}{\sin \theta} P_n^m(\cos \theta) \\ + A_M^S(m, n) \frac{\partial}{\partial \theta} P_n^m(\cos \theta) \end{array} \right] \sin m\phi e^{jkd \cos \theta} \quad (79)$$

$$F_{\theta 3}(\theta, \phi) = \sum_{n=1}^{\infty} \sum_{m=-n}^n j^{-n+1} \left[\begin{array}{l} -B_E^S(m, n) \frac{\partial}{\partial \theta} P_n^m(\cos \theta) \\ + B_M^S(m, n) \frac{m}{\sin \theta} P_n^m(\cos \theta) \end{array} \right] \cos m\phi e^{-jkd \cos \theta} \quad (80)$$

$$F_{\phi 3}(\theta, \phi) = \sum_{n=1}^{\infty} \sum_{m=-n}^n j^{-n+1} \left[\begin{array}{l} B_E^S(m, n) \frac{m}{\sin \theta} P_n^m(\cos \theta) \\ + B_M^S(m, n) \frac{\partial}{\partial \theta} P_n^m(\cos \theta) \end{array} \right] \sin m\phi e^{-jkd \cos \theta} \quad (81)$$

Often the scattered radiation is most conveniently measured by the bistatic radar cross-section. The bistatic radar cross-section is defined as

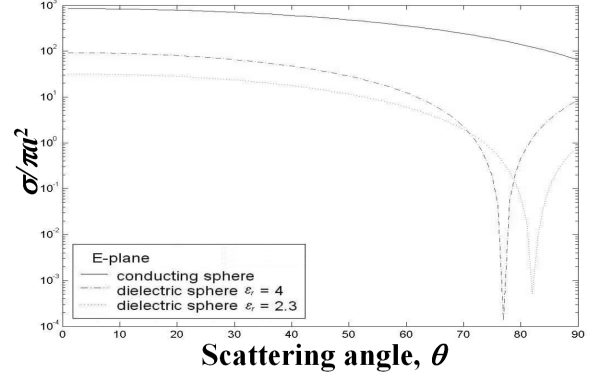


Fig. 5. Normalized bistatic cross-sections in the E plane of a partially buried dielectric sphere vs. the scattering angle θ for $ka = 1.0$, $d = 0.5a$, and $\epsilon_r = \infty, 4, 2.3$.

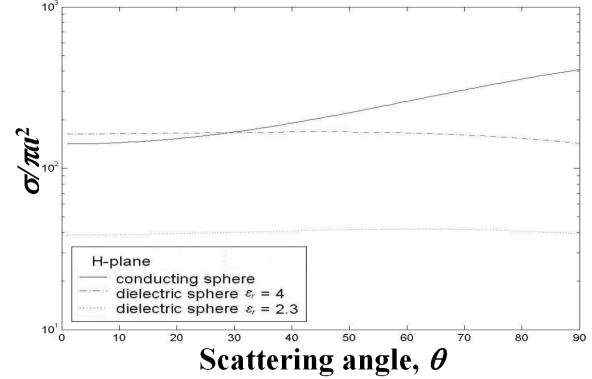


Fig. 6. Normalized bistatic cross-sections in the H plane of a partially buried dielectric sphere vs. the scattering angle θ for $ka = 1.0$, $d = 0.5a$, and $\epsilon_r = \infty, 4, 2.3$.

$$\sigma(\theta, \phi) = \lim_{r \rightarrow \infty} 4\pi^2 \left| E_{Total}^S \cdot \hat{t} \right|^2 / |E_i|^2 \quad (82)$$

with the unit vector \hat{t} denoting the direction of polarization of the receiver at the observation point. When \hat{t} has the same direction as E_{Total}^S , the normalized

$$\text{bistatic radar cross-section is given by} \quad (83)$$

$$\frac{\sigma(\theta, \phi)}{\pi a^2} = \frac{4}{(ka)^2} \left[\begin{array}{l} |F_{\theta 1}(\theta, \phi) + F_{\theta 2}(\theta, \phi) + F_{\theta 3}(\theta, \phi)|^2 \\ + |F_{\phi 1}(\theta, \phi) + F_{\phi 2}(\theta, \phi) + F_{\phi 3}(\theta, \phi)|^2 \end{array} \right]$$

The normalized bistatic radar cross-sections in the E and H planes are obtained by substituting $\phi = \pi/2$ and $\phi = 0$, respectively, into Eq. (83). For the back-scattering cross-section, when $\theta = \pi - \alpha$ and $\phi = \pi$, the corresponding normalized back-scattering cross section is

$$\frac{\sigma(\alpha)}{\pi a^2} = \frac{4}{(ka)^2} |F_{\theta 1}(\theta, \phi) + F_{\theta 2}(\theta, \phi) + F_{\theta 3}(\theta, \phi)|^2 \quad (84)$$

The normalized bistatic cross-section patterns in the E and H planes are plotted for the partially buried dielectric sphere versus the scattering angle θ , taken between 0° and 90° , and corresponding to end fire incidence ($\alpha = 0^\circ$), as well as for different burial

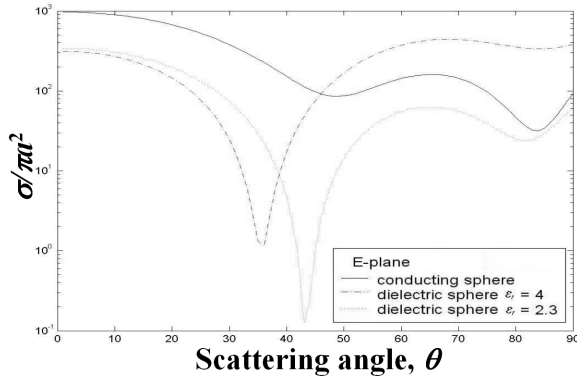


Fig. 7. Normalized bistatic cross-section in the E plane of a partially buried dielectric sphere vs. the scattering angle θ for $ka = 2.0$, $d = 0.75a$, and $\epsilon_r = \infty, 4, 2.3$.

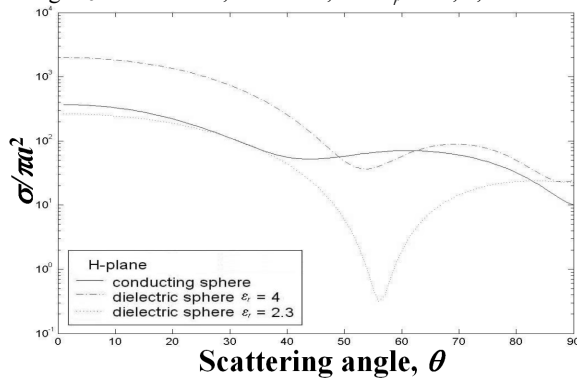


Fig. 8. Normalized bistatic cross-section in the H plane of a partially buried dielectric sphere vs. the scattering angle θ for $ka = 2.0$, $d = 0.75a$, and $\epsilon_r = \infty, 4, 2.3$.

distances. Figures 3 and 4 show the normalized scattering cross-sections for a sphere of electrical radius $ka = 1.0$, burial distance $d = a$, and relative dielectric constant $\epsilon_r = 4$ and $\epsilon_r = 2.3$. Furthermore, Figures 3 and 4 compare the numerical results of the conducting sphere residing on the ground plane that is represented by a continuous-line curve with the dielectric spheres with relative permittivity $\epsilon_r = 4$ and $\epsilon_r = 2.3$ represented by the broken-line curve and dotted-line curves, respectively. The three curves have almost the same behavior except for a resonance that occurs at $\theta = 79^\circ$ and 84° for the non-conducting spheres in the E plane. It can also be seen that the magnitude of the backscattering cross section for the dielectric cases are lower in average for both planes. Figures 5 and 6 show the normalized bistatic cross-sections of the same electrical radius and relative dielectric constants but with a burial distance of $d = 0.5a$. It appears that the dielectric spheres now show much significant resonance behavior at $\theta = 78^\circ$ and 82° . Figures 7 to 10 show the normalized bistatic cross-sections for a partially buried sphere of electrical radius $ka = 2.0$ with the same relative dielectric constants but with a burial distance of

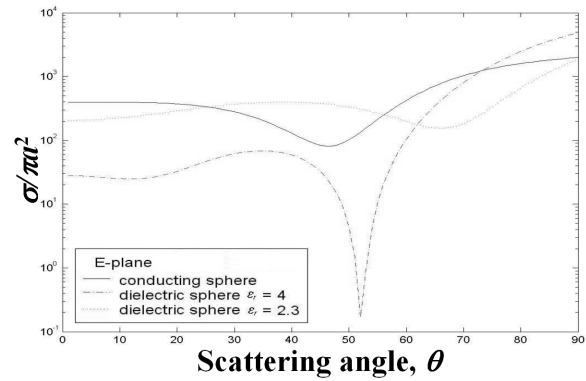


Fig. 9. Normalized bistatic cross-section in the E plane of a partially buried dielectric sphere vs. the scattering angle θ for $ka = 2.0$, $d = 0.5a$, and $\epsilon_r = \infty, 4, 2.3$.

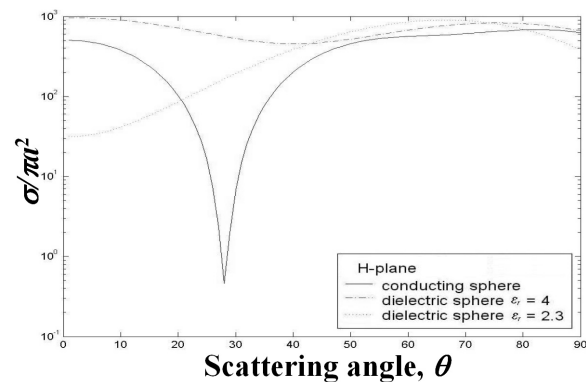


Fig. 10. Normalized bistatic cross-section in the H plane of a partially buried dielectric sphere vs. the scattering angle θ for $ka = 2.0$, $d = 0.5a$, and $\epsilon_r = \infty, 4, 2.3$.

$d = 0.7a$, and $d = 0.5a$, respectively. It can be seen that the behavior of the curves has become wavier as electrical radius of the sphere is increased.

4. THE NEURAL NETWORK APPROACH

Radial basis functions (RBF) emerged as a variant of artificial neural network in the late 1980's. However, their roots are entrenched in much older pattern recognition techniques as, for example, potential functions, clustering, functional approximation, spline interpolation and mixture models. Their excellent approximation capabilities have been studied by Park and Sandbeg [11], and Poggio and Girosi [12]. Due to their nonlinear approximation properties, RBF networks are able to model complex mappings, which perception neural networks can only model by means of multiple intermediary layers.

In order to estimate the relative permittivity ϵ_r , the electrical radius and the burial distance of the sphere, a/λ and d/λ of the sphere, respectively, we employ the radial basis function network shown schematically in Fig. 2. The network consists of three

layers; an input layer that consists of four sets of inputs, a hidden layer using Gaussian nonlinearity functions, and an output layer with three outputs. Each hidden unit represents a single radial basis function, with associated center position and width. Such hidden units are sometimes referred to as centroids or kernels. Each output unit performs a weighted summation of the hidden units, using the ω_j s as weights. The four sets of inputs in the input layer are the real and imaginary values of the computed scattered field complex coefficients for the TE (A_E^S & B_E^S) and TM (A_M^S & B_M^S) polarization cases, while the outputs are the electrical radius and burial distance of the sphere as well as its relative permittivity. This network is designed to perform nonlinear mapping from the input layer to the hidden layer, which is then followed by linear mapping from the hidden layer to the output layer. For this, we choose a function $y_k(x)$ with the following form:

$$y_k(x) = \sum_{j=1}^M \omega_j \phi(\|x - \mu_j\|) \quad (85)$$

variable x represents the input vector while $\phi(\|\cdot\|)$ are nonlinear functions known as the radial basis functions that consist of Gaussian function $\phi_c(r) = e^{-r^2/\sigma^2}$ and Euclidean norm $\|\cdot\|$. The known data points, μ_j , are taken to be the centers of the radial basis functions. The design of the network includes the selection of the width parameter σ_j and the weighting functions ω_j such that it minimizes the difference between the network output and the desired output. The training of the network will be discussed in the next section followed by the demonstration of the training results in Section 6.

5. NETWORK TRAINING

In order to use a Radial Basis Function Network, we need to specify the hidden unit activation function, the number of processing units, a criterion for modeling a given task and a training algorithm for finding the parameters of the network. Finding the three sets of RBF network parameters (the centers, the widths, and the weights) is called network training. There are two categories of training algorithms: supervised and unsupervised. RBF networks are used mainly in supervised applications. In a supervised application, we are provided with an asset of data samples called a training set for which the corresponding network outputs are known. In this case, the network parameters are found such that they minimize a cost function:

$$\min \sum_{k=1}^M \{t_k^n - y_k(x^n)\}^2 \quad (86)$$

where M is the total number of vectors from the training set, t_k^n is the target value of the output vector and $y_k(x^n)$ represents the output vector associated with a

data sample x^n from the training set. If Gaussian basis functions are used to minimize this cost function, one can perform a stochastic gradient descent and readily obtain the update equations:

$$\Delta\omega_{kj} = \eta_1 (t_k^n - y_k(x^n)) \phi_j(x^n) \quad (87)$$

$$\Delta\mu_j = \eta_2 \phi_j(x^n) \frac{\|x^n - \mu_j\|}{\sigma_j^2} \sum_{k=1}^M \{y_k(t_k^n) - x^n\} \omega_{kj} \quad (88)$$

$$\Delta\sigma_j = \eta_3 \phi_j(x^n) \frac{\|x^n - \mu_j\|^2}{\sigma_j^3} \sum_{k=1}^M \{y_k(t_k^n) - x^n\} \omega_{kj} \quad (89)$$

where η_1, η_2, η_3 are the learning rates.

In unsupervised training, the output assignment is not available for the given training set. One of the approaches is assigning a basis function for each of the data samples. This solution proved to be expensive in terms of memory requirement and in the number of parameters. Other approaches choose randomly, or assume known, the hidden unit weights and calculate the output weights ω_{jk} by solving a system of equations whose solution is given in the training set. The matrix inversion required in this approach is computationally expensive and could cause numerical problems in certain situations (when the matrix is singular).

For RBF networks, finding the right number of free parameters is crucial. This involves trying to determine the optimal number of hidden units. Hence, the analysis of the effect of adding a new hidden unit or removing an existing unit is an important one. Backward elimination and forward selection are two ways of pruning and growing RBF networks. In backward elimination, a network is constructed with all the basic functions in the candidate pool. At each step, the unit that least increases the error is eliminated from the network. Again, this procedure is continued until some model selection criterion stops decreasing. At this point, the complexity of the model is assumed sufficient to represent the underlying function complexity.

In forward selection, one is given an initial network configuration and a candidate pool of basis functions; typically Gaussians centered at the training data points. At each step, the hidden basis function unit, which decreases the error most, such as sum-squared-error, is removed from the candidate pool and added to the network. Though forward selection is a nonlinear optimization technique, it has the advantages of not having to fix the number of hidden units in advance, tractable model selection criteria, and computational efficiency. The projection matrix for the case where an extra hidden unit has been added is given by

$$P_{m+1} = P_m - \frac{P_m f_j f_j^T P_m}{f_j^T P_m f_j} \quad (90)$$

where, f_j is the column of the design matrix, Φ , corresponding to the most recently recruited hidden

unit. The reduction in the sum-squared-error due to the addition of the unit is given by

$$\hat{S}_m - \hat{S}_{m+1} = \frac{(\hat{y}^T P_m f_J)^2}{f_J^T P_m f_J}. \quad (91)$$

The unit, which reduces the sum-squared-error most, is the chosen candidate. Geometrically, this will be the unit whose corresponding basis vector is most closely aligned to the perpendicular from \hat{y} to the current m -dimensional space. Though the sum-squared-error reduces as more hidden units are added, the model selection criterion will reach a minimum before it starts increasing again. This is the point where the process is stopped.

Forward selection is a relatively fast algorithm but it can be speeded up even further using a technique called orthogonal least squares [9]. This is a Gram-Schmidt orthogonalization process [15], which ensures that each new column added to the design matrix of the growing subset is orthogonal to all previous columns. This simplifies the equation for the change in sum-squared-error and results in a more efficient algorithm.

Any matrix can be factored into the product of a matrix with orthogonal columns and a matrix which is upper triangular. In particular, the design matrix, $H_m \in \mathfrak{R}^{p \times m}$, can be factored into

$$H_m = \tilde{H}_m U_m \quad (92)$$

where $\tilde{H}_m = [\tilde{h}_1 \ \tilde{h}_2 \ \dots \ \tilde{h}_m] \in \mathfrak{R}^{p \times m}$ has orthogonal columns ($\tilde{h}_i^T \tilde{h}_j = 0, i \neq j$) and $U_m \in \mathfrak{R}^{m \times m}$ is upper triangular.

When considering whether to add the basis function corresponding to J -th column, \tilde{f}_j of the full design matrix, the projection of \tilde{f}_j in the space already spanned by the m columns of the current design matrix is irrelevant. Only its projection perpendicular to this space, namely

$$\tilde{f}_J - \sum_{j=1}^m \frac{\tilde{f}_J^T \tilde{h}_j}{\tilde{h}_j^T \tilde{h}_j} \tilde{h}_j \quad (93)$$

can contribute to a further reduction in the training error, and this reduction is

$$\hat{S}_m - \hat{S}_{m+1} = \frac{(\hat{y}^T \tilde{f}_J)^2}{\tilde{f}_J^T \tilde{f}_J}. \quad (94)$$

Computation of this change in sum-squared-error is lower compared to the unnormalized version given in equation (91). This is the basis of the increased efficiency of orthogonal least squares.

A small overhead is necessary to maintain the columns of the full design matrix orthogonal to the space spanned by the columns of the growing design matrix and to update the upper triangular matrix. After \tilde{f}_j is selected the new orthogonalized full design matrix is

$$\tilde{F}_{m+1} = \tilde{F}_m - \frac{\tilde{f}_J \tilde{f}_J^T \tilde{F}_m}{\tilde{f}_J^T \tilde{f}_J} \quad (95)$$

and the upper triangular matrix is updated to

$$U_m = \begin{bmatrix} U_{m-1} & (\tilde{H}_{m-1}^T \tilde{H}_{m-1})^{-1} \tilde{H}_{m-1}^T f_J \\ O_{m-1}^T & 1 \end{bmatrix}. \quad (96)$$

Initially $U_1 = 1$ and $\tilde{F}_0 = F$. The orthogonalized optimal weight vector

$$\tilde{w}_m = (\tilde{H}_m^T \tilde{H}_m)^{-1} \tilde{H}_m^T \hat{y} \quad (97)$$

and the unorthogonalized optimal weight equation are then related by

$$\hat{w}_m = U_m^{-1} \tilde{w}_m. \quad (98)$$

6. NETWORK SIMULATION RESULTS

The training and testing of the proposed Radial Basis Function Network was carried out using MATLAB script. After the Radial Basis Function Network is trained with a set of chosen learning data, a new set of test data that is different from the learning data is generated to evaluate the trained network. The learning data set requires 50 distinct sample values for each of the three outputs. Therefore, 125,000 samples are required as the learning data set. The range of the electrical radius a , of the training sphere is from 0.01λ to 5λ . The range of the

burial distance is from 0 to a (half buried in the conducting ground to residing on the surface of the conducting ground) while the range of the relative permittivity ϵ_r is from 1 to 9. Each of the sample sets holds 4 set of inputs and 3 target outputs. The 4 set of inputs are:

x_{1j} : Real value of scattered field coefficients for TE polarization case:

$$real(A_E^S(m,n)) \text{ and } real(B_E^S(m,n))$$

x_{2j} : Real value of scattered field coefficients for TM polarization case:

$$real(A_M^S(m,n)) \text{ and } real(B_M^S(m,n))$$

x_{3j} : Imaginary value of scattered field coefficients for TE polarization case:

$$imag(A_E^S(m,n)) \text{ and } imag(B_E^S(m,n))$$

x_{4j} : Imaginary value of scattered field coefficients for TM polarization case:

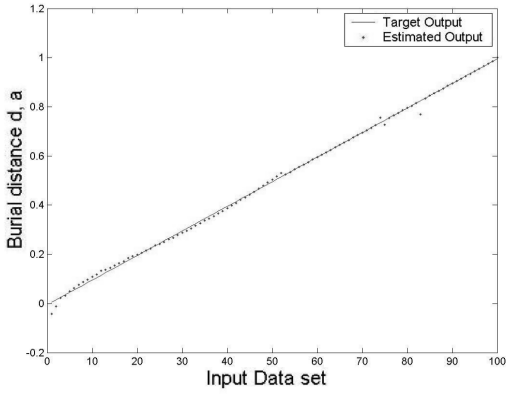
$$imag(A_M^S(m,n)) \text{ and } imag(B_M^S(m,n))$$

where $j = 1, \dots, d$ and $d = 4n^2 + 2n = 42$.

The higher the order of n , the higher the accuracy of the outputs and the large data set of the mapping function can become very costly to evaluate. Nevertheless, the coefficients of order up to the 3rd order ($n=3$) were sufficient for training of a sphere with electric radius 0.01λ to 5λ . Similarly, the use of only one set of the scattered field coefficients ($real(A_E^S(m,n))$) will result in poor performance.

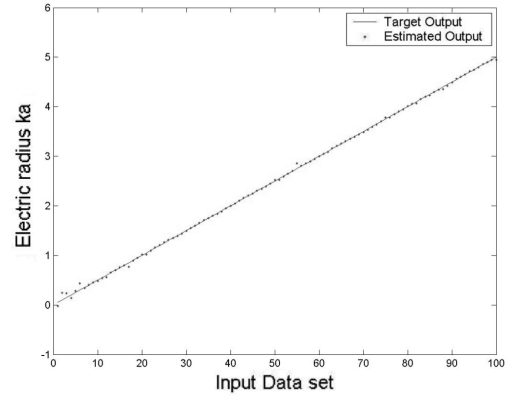
The test results are plotted in Figs. 11 to 18.

Figures 11 and 12 show the RBF network estimated burial distance of the sphere with electric radius $ka = 1$



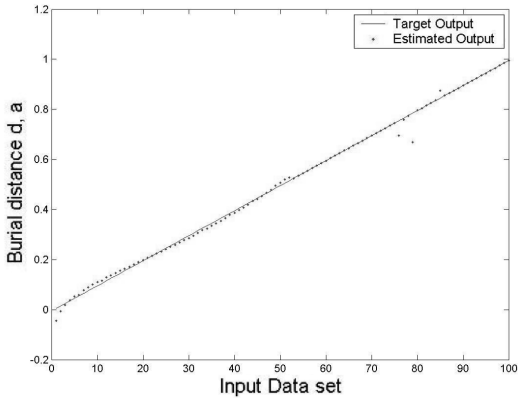
Average absolute error = 0.0043
 % error relative to sphere radius = 0.43%

Fig. 11. RBF network estimated burial distance ($ka=1.0$ and $\epsilon_r = 2.3$ ($m=1.51$)).



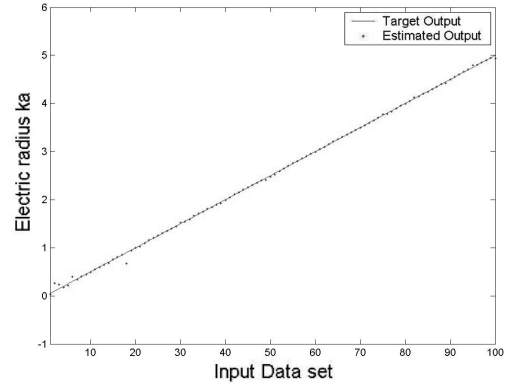
Average absolute error = 0.0159
 Average relative percentage error = 4.95%

Fig. 13. RBF network estimated electric radius ($d=0.5a$ and $\epsilon_r = 2.3$ ($m=1.51$)).



Average absolute error = 0.0067
 % error relative to sphere radius = 0.67%

Fig. 12. RBF network estimated burial distance ($ka=1.0$ and $\epsilon_r = 4.0$ ($m=2.0$)).



Average absolute error = 0.0144
 Average relative percentage error = 3.73%

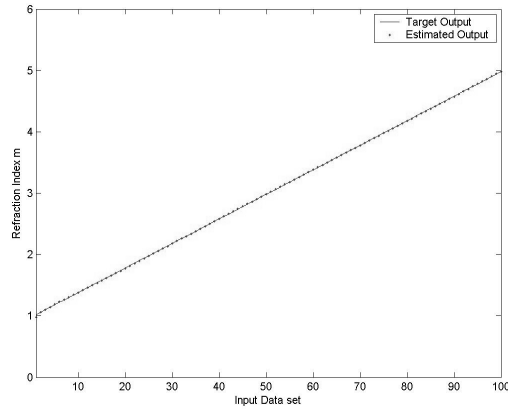
Fig. 14. RBF network estimated electric radius ($d=0.5a$ and $\epsilon_r = 4.0$ ($m=2.0$)).

and relative permittivity, $\epsilon_r = 2.3$, and $\epsilon_r = 4$, respectively. When burial distance $d = 0$, the sphere is half buried in the conducting ground and when burial distance $d = a$, the sphere is touching and residing on the conducting ground. From the results plotted in Fig. 11 and Fig. 12, the estimated burial distance is found to be very accurate as the percentage error of the estimated burial distance relative to the sphere radius is less than 1%. Figures 13 and 14 show the RBF network estimated electric radius of the sphere with burial distance $d = 0.5a$ and relative permittivity $\epsilon_r = 2.3$, and $\epsilon_r = 4$, respectively. The network gives poor prediction results when the electrical radius ka of the sphere is below 1 and close to zero, where the sphere is disappearing. While Figures 15 to 18 show the RBF network estimated refraction index m of the sphere with electrical radius $ka = 1$ and burial distance $d = 0$, $d =$

$0.25a$, $d = 0.5a$, and $d = a$, respectively. As expected, the estimated sphere parameters are very close to the target values.

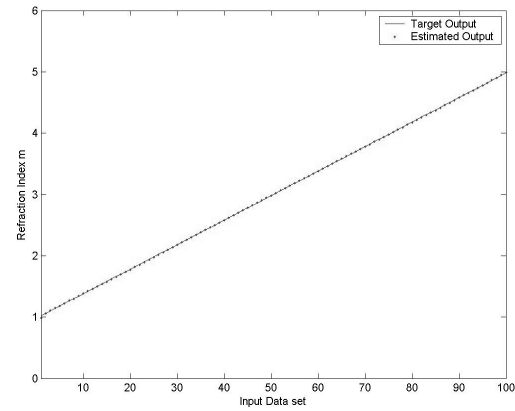
7. CONCLUSION

The first part of this paper describes an exact solution to the problem of scattering by a partially truncated dielectric sphere resting on a ground plane. The different bistatic cross-section results were obtained for various electrical radii, burial depths or the truncated depths and relative permittivity of the sphere. Since the medium intrinsic impedance of the sphere, η , is a function of the relative dielectric constant of the material of the sphere ϵ_r . It is obvious that the present solution should tend to that of a conducting sphere partially buried in a ground plane as $\epsilon_r \rightarrow \infty$.



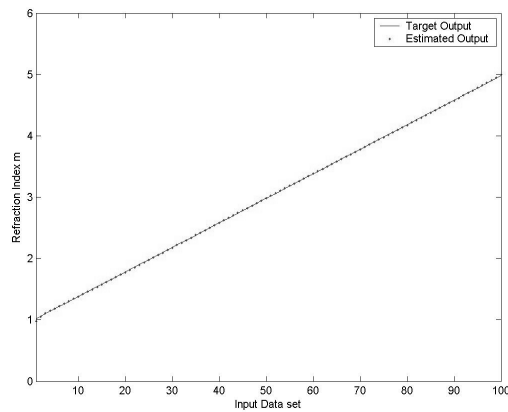
Average absolute error = 0.0038
Average relative percentage error = 0.18%

Fig. 15. RBF network estimated refraction index m ($ka=1$ and $d=0$).



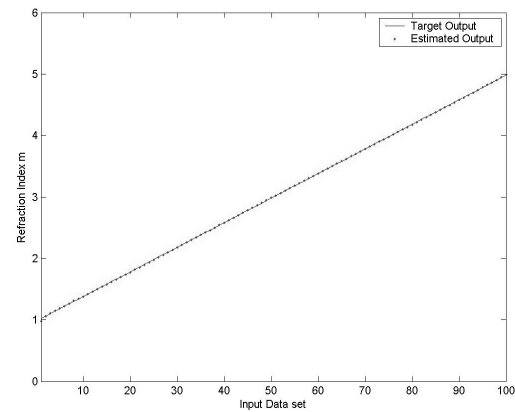
Average absolute error = 0.0036
Average relative percentage error = 0.16%

Fig. 17. RBF network estimated refraction index m ($ka=1$ and $d=0.5a$).



Average absolute error = 0.0038
Average relative percentage error = 0.18%

Fig. 16. RBF network estimated refraction index m ($ka=1$ and $d=0.25a$).



Average absolute error = 0.0037
Average relative percentage error = 0.18%

Fig. 18. RBF network estimated refraction index m ($ka=1$ and $d=a$).

Furthermore, the solution should tend to well known solutions for the special cases when $d \rightarrow 0$ [13,14].

Comparing to analytical and numerical techniques, the proposed method of using neural networks in inverse scattering is simple, straightforward and timesaving, since it does not require matrix inversion, recurrence relations or graphical inversion methods to retrieve the desired parameters of the sphere. From the computer simulation results, the proposed method has proven effective in predicting the non-linear relation between the scattered field coefficient inputs and the sphere parameter outputs. The network has successfully retrieved the burial distance, radius, and relative permittivity of the dielectric sphere partially buried in a conducting ground given the scattering coefficients of the scatterer. Above and beyond, the performance of the proposed RBF network is proportional to the number of learning samples.

Therefore, by increasing the number of learning samples, a better prediction of the network will be achieved.

ACKNOWLEDGEMENT

The authors wish to acknowledge the financial assistance of the National Science Foundation.

REFERENCES

- [1] A.-K. Hamid, and M. Hamid, "Electromagnetic scattering by a dielectric sphere partially buried in an infinite plane," *Canadian Journal of Physics*, vol. 80, pp. 979-986, 2002.
- [2] C. Eftimiu, "Direct and inverse scattering by a sphere of variable index of refraction," *Journal of Mathematical Physics*, vol. 23, no. 11, pp. 2140-2146. 1982.

- [3] J. Sylvester, and D. P. Winebrenner, "Linear and nonlinear inverse scattering," *SIAM Journal of Applied Mathematics* 59(2), pp. 669-699, 1998.
- [4] I. T. Rekanos, T. V. Yioultis & T.D.Tsiboukis "Inverse scattering using the finite-element method and a nonlinear optimization Technique ", *IEEE Trans. On Microwave Theory and Techniques*, vol. 47, no. 3, pp. 336-344,1999.
- [5] A-K Hamid, "A neural-network approach to the inverse-scattering problem from a circular conducting cylindrical scatterer," *Microwave and Optical Tech. Letters*, vol. 13, no. 6, pp. 380-382, 1998.
- [6] E. Bermami, S. Caorsi, M. Raffetto, "An inverse scattering approach based on a neural network technique for the detection of dielectric cylinders buried in a lossy half-space," *Progress in Electromagnetics Research*, no. 26, pp. 69-90, 2000.
- [7] S. Caorsi and P. Gamba, "Electromagnetic detection of dielectric cylinder by a neural network approach," *IEEE Trans. on Geoscience and Remote Sensing*, vol. 37, 820-827, 1999.
- [8] X. Gong and Y. Wang, "A neural network approach to the microwave inverse scattering problem with edge-preserving regularization," *Radio Science*, vol. 36, no. 5, pp. 825-832, 2001.
- [9] S. Chen, C. F. N. Cowan, and P. M. Grant. "Orthogonal least squares learning for radial basis function networks," *IEEE Trans. On Neural Networks*, vol. 2, no. 2, pp. 302-309, 1991.
- [10] Y. L. Xu, "Electromagnetic scattering by an aggregate of spheres: Far field," *Appl. Optics*. vol. 36, pp. 9496-9508, 1997.
- [11] J. Park and J. W. Sandbeg, "Universal approximation using radial basis functions network," *Neural Computation*, vol. 3, pp. 246-257, 1991.
- [12] T. Poggio and F. Girosi, (1990) "Networks for approximation and learning," *Proc. IEEE*, vol. 78, no. 9, pp. 1481-1497.
- [13] J. A. Stratton, *Electromagnetic Theory*, McGraw-Hill, New York, 1941.
- [14] P. Bhartia, R. A. Ross and M. Hamid, "Ray optical scattering by two spheres", *Arch. Elekt. Ubertrag.*, vol. 24, pp. 215-222, 1970.
- [15] R. A. Horn and C. R. Johnson. "Matrix Analysis," *Cambridge University Press*, Cambridge, UK, 1985.

APPENDIX

Xu's vector translation addition theorem coefficients:

$$A_{\mu\nu}^{mn}(d_{pq}, \theta_{pq}, \phi_{pq}) = (-1)^{m+n} a_0 \frac{2n+1}{2n(n+1)} e^{j(\mu-m)\phi_{pq}} \quad (A1)$$

$$\times \sum_p \left\{ \begin{matrix} n(n+1) \\ j^{p-n-\nu} + \nu(\nu+1) \\ -p(p+1) \end{matrix} \right\} a_1 z_p^{(j)} (kd_{pq}) P_p^{\mu-m} \cos(\theta_{pq})$$

$$B_{\mu\nu}^{mn}(d_{pq}, \theta_{pq}, \phi_{pq}) = (-1)^{m+n} a_0 b_0 \frac{2n+1}{2n(n+1)} e^{j(\mu-m)\phi_{pq}} \quad (A2)$$

$$\times \sum_p \left\{ \begin{matrix} 2(n+1)(\nu-\mu)a_2 \\ j^{p-n-\nu+1} - [p(p+3) - \nu(\nu+1)] \\ -[n(n+3) - 2\mu(n+1)]a_3 \end{matrix} \right\} \times z_{p+1}^{(j)} (kd_{pq}) P_{p+1}^{\mu-m} \cos(\theta_{pq})$$

where

$$z_p^{(j)} = z_p^{(j)}, \quad \text{if } r \leq d_{pq}$$

$$z_p^{(j)} = j_p^{(1)}, \quad \text{if } r \geq d_{pq}$$

$$a_0 = a(-m, n, \mu, \nu, n+\nu)$$

$$a_1 = \frac{a(-m, n, \mu, \nu, p)}{a(-m, n, \mu, \nu, n+\nu)}$$

$$a_2 = \frac{a(-m-1, n+1, \mu+1, \nu, p+1)}{a(-m-1, n+1, \mu+1, \nu, n+\nu+1)}$$

$$a_3 = \frac{a(-m, n+1, \mu, \nu, p+1)}{a(-m, n+1, \mu, \nu, n+\nu+1)}$$

$$b_0 = \frac{(2n+1)(n+\nu+m-\mu+1)}{(2n+2\nu+1)(n+m+1)}$$

and $a(m, n, \mu, \nu, p)$ is the Gaunt coefficient given by,

$$a(m, n, \mu, \nu, p) = (-1)^{m+\mu} (2p+1) \frac{[(n+m)!(\nu+\mu)!(p-m-\mu)!]}{[(n-m)!(\nu-\mu)!(p+m+\mu)!]} \quad (A3)$$

$$\times \begin{pmatrix} n & \nu & p \\ 0 & 0 & 0 \end{pmatrix} \begin{pmatrix} n & \nu & p \\ m & \mu & (-m-\mu) \end{pmatrix}$$

where the symbol $\begin{pmatrix} j_1 & j_2 & j_3 \\ m_1 & m_2 & m_3 \end{pmatrix}$ is the so-called

Wigner 3-j symbol. The integer p in the summations takes the values $n+\nu, n+\nu-2, \dots, |n-\nu|$.

Chye-Hwa Loo received his B.S. degree in 2001, and his M.S. degree in 2003, both in Electrical Engineering from the University of South Alabama. Currently he is a Ph.D. student in the Department of Electrical Engineering at University of Mississippi. His research interests are remote sensing and scattering.

Michael Hamid Graduated from McGill University in Montreal with a B. Eng. Degree in 1960, a M. Eng. Degree in 1962 and from the University of Toronto with a Ph.D. degree in 1966, all in Electrical Engineering. He joined the University of Manitoba in 1965 where he became a Professor of Electrical Engineering and Head of the Antenna Laboratory. He was a Visiting Professor at the University of California Davis and Central Florida and is presently a Professor of Electrical Engineering at the University of South Alabama. He is a past president of the International Microwave Power Institute, a Fellow of IEE and IEEE and published 310 refereed articles and 25 patents.

Recent Advances in Sensitivity Analysis with Frequency-Domain Full-Wave EM Solvers

Shirook M. Ali, Natalia K. Nikolova and Mohamed H. Bakr

Department of Electrical and Computer Engineering
McMaster University

Hamilton, Ontario L8S 4K1, CANADA.

Phone +1 905 525 9140 Fax +1 905 523 4407

E-mail: alis5@mcmaster.ca, talia@mcmaster.ca, mbakr@mail.ece.mcmaster.ca

Abstract — This paper introduces recent developments in efficient sensitivity analysis with numerical electromagnetic solvers in the frequency domain. We start by reviewing our original discrete approaches for sensitivity analysis. We then propose and investigate, for the first time, two new discrete approaches which enhance the accuracy of the estimated derivatives. All four introduced approaches are based on the adjoint-variable method and target solvers on structured grids. Discussion and comparison of the accuracy and convergence for the different approaches are also given. Examples include waveguide and printed structures.

I. INTRODUCTION

The adjoint-variable sensitivity analysis of 3-D distributed systems has been studied in structural engineering [1], and its use with the finite-element method (FEM) in structural shape design with gradient-based optimizers is a known efficient design approach [2]. Applications with the FEM in electromagnetic problems span problems from eddy currents to high-frequency devices, e.g. [3],[4].

In the implementation of this methodology with other numerical methods, some unsolved problems have been identified. First, time-harmonic electromagnetic (EM) problems lead to complex analysis with complex response functions, while the theory found in [1]-[4], and elsewhere, does not discuss the complex case. Adjoint-network approaches [5] deal with complex problems but their relation to full-wave analysis is not so straightforward. Second, the classical adjoint-variable method assumes that the system matrices are differentiable with respect to the design parameters, and their derivatives are available. In EM analysis, however, the system matrix derivatives—if existing at all—require cumbersome analytical pre-processing and major software changes in the existing full-wave solvers. Besides, methods using structured grids – such as transmission-line matrix (TLM) methods, or finite-difference (FD) methods – produce system matrices, which are not analytical functions of the coordinates of the mesh nodes. Therefore, strictly speaking, they are not differentiable with respect

to the shape design parameters.

Here we present a framework of methodologies for EM-based sensitivity analysis where analytical derivatives of the system matrices are not needed. The analytical pre-processing is avoided, and the implementation is made simple and versatile. Our approaches—being adjoint in nature—are efficient, as they compute the system response and all its derivatives with at most two system analyses, regardless of the number of the design parameters.

For the first time, we derive a sensitivity formula in which perturbations relate to the adjoint problem instead of the original problem. This formula has the potential of better accuracy especially when highly nonlinear responses are of interest. We also develop a central adjoint formula which improves the accuracy of the estimated sensitivities even further.

Discussion and comparisons between the presented discrete adjoint techniques are given through a variety of examples including waveguides and printed structures. In addition, conclusions with regard to the accuracy of the presented techniques are made through robust convergence analysis.

We start in Section II by giving a brief review of the mathematical concepts used in sensitivity analysis. Still there, we present our adjoint-based approaches to sensitivity analysis with structured-grid solvers. Practical examples and comparisons are given in Section III. Finally, conclusions are made in Section IV.

II. MATHEMATICAL FORMULATION

A. Definitions and Notation

The analysis stage of a design assembles and solves equations, which describe the system. For linear stationary systems,

$$\mathbf{A}(\mathbf{p})\mathbf{x} = \mathbf{b}(\mathbf{p}), \quad (1)$$

where $\mathbf{A} \in \mathbb{C}^{M \times M}$ is the system matrix, $\mathbf{x} \in \mathbb{C}^{M \times 1}$ is the state-variable vector, and $\mathbf{b} \in \mathbb{C}^{M \times 1}$ is the excitation. In the case of time-harmonic processes, (1) is complex. We denote with \mathbf{p} a vector of N shape and/or material design

parameters of the system, which may vary, e.g., to obtain better system performance, or due to technological or environmental factors. We assume that the elements of the design-parameter vector are real-valued. These variations in general affect the system matrix \mathbf{A} , the excitation vector \mathbf{b} , and, as a result, the solution as well, i.e., $\mathbf{x}(\mathbf{p})$. The system output is usually described by a vector of complex-valued responses $\mathbf{R}(\mathbf{x}(\mathbf{p}))$, e.g., the four S -parameters of a two-port microwave network. Its overall performance is often formulated in terms of a single scalar function, $f(\mathbf{R}(\mathbf{p}))$, the response function.

The purpose of sensitivity analysis is to describe the rate of change of the response function with each design parameter:

$$\nabla_{\mathbf{p}} f, \text{ subject to } \mathbf{A}\mathbf{x} = \mathbf{b}, \quad (2)$$

where the gradient is defined as a row operator [1]:

$$\nabla_{\mathbf{p}} f = \left[\frac{\partial f}{\partial p_1} \quad \frac{\partial f}{\partial p_2} \quad \dots \quad \frac{\partial f}{\partial p_N} \right].$$

This information is valuable in optimization, modeling, tolerance and yield analyses.

B. Second-order Sensitivity Expression I (AVM-I)

For a perturbation Δp_i in the i th parameter, (1) becomes

$$(\mathbf{A} + \Delta_i \mathbf{A})(\mathbf{x} + \Delta_i \mathbf{x}) = \mathbf{b} + \Delta_i \mathbf{b}. \quad (3)$$

Here, Δ_i denotes a variation caused by the perturbation Δp_i . Simplifying and rearranging (3), we obtain

$$\mathbf{A} \Delta_i \mathbf{x} + \Delta_i \mathbf{A} \cdot \mathbf{x} + \Delta_i \mathbf{A} \cdot \Delta_i \mathbf{x} = \Delta_i \mathbf{b}. \quad (4)$$

A possible expression for the variation of the state variables is

$$\Delta_i \mathbf{x} = \mathbf{A}^{-1} \left[\Delta_i \mathbf{b} - \Delta_i \mathbf{A} \cdot (\mathbf{x} + \Delta_i \mathbf{x}) \right] \quad (5)$$

assuming that \mathbf{A}^{-1} exists.

This variation is needed to find the derivative of the response function df/dp_i , where f can be a complex quantity, $f = f_R + jf_I$. We assume that f is an analytic function of the state variables $\mathbf{x} = \mathbf{x}_R + j\mathbf{x}_I$. In expanded form

$$\begin{aligned} \frac{df}{dp_i} = & \frac{\partial f_R}{\partial p_i} + \left(\frac{\partial f_R}{\partial x_{1R}} \frac{dx_{1R}}{dp_i} + \frac{\partial f_R}{\partial x_{1I}} \frac{dx_{1I}}{dp_i} + \dots + \frac{\partial f_R}{\partial x_{MR}} \frac{dx_{MR}}{dp_i} \right. \\ & \left. + \frac{\partial f_R}{\partial x_{MI}} \frac{dx_{MI}}{dp_i} \right) + j \frac{\partial f_I}{\partial p_i} + j \left(\frac{\partial f_I}{\partial x_{1R}} \frac{dx_{1R}}{dp_i} + \frac{\partial f_I}{\partial x_{1I}} \frac{dx_{1I}}{dp_i} \right. \\ & \left. + \dots + \frac{\partial f_I}{\partial x_{MR}} \frac{dx_{MR}}{dp_i} + \frac{\partial f_I}{\partial x_{MI}} \frac{dx_{MI}}{dp_i} \right). \end{aligned} \quad (6)$$

Due to the analyticity of f , the Cauchy-Riemann relations

$$\frac{\partial f_R}{\partial x_{mR}} = \frac{\partial f_I}{\partial x_{mI}}, \quad \frac{\partial f_R}{\partial x_{mI}} = -\frac{\partial f_I}{\partial x_{mR}}, \quad m = 1, \dots, M, \quad (7)$$

hold. Using (7), we write (6) as

$$\frac{df}{dp_i} = \frac{\partial f}{\partial p_i} + \nabla_{\mathbf{x}} f \cdot \frac{d\mathbf{x}}{dp_i}, \quad (8)$$

where

$$\nabla_{\mathbf{x}} f = \nabla_{x_R} f_R - j \nabla_{x_I} f_R = \nabla_{x_R} f_R + j \nabla_{x_I} f_I, \text{ etc.}, \quad (9)$$

and

$$\frac{d\mathbf{x}}{dp_i} = \frac{d\mathbf{x}_R}{dp_i} + j \frac{d\mathbf{x}_I}{dp_i}. \quad (10)$$

We approximate (8) as

$$\frac{df}{dp_i} \approx \frac{\partial f}{\partial p_i} + \nabla_{\mathbf{x}} f \cdot \frac{\Delta_i \mathbf{x}}{\Delta p_i} \quad (11)$$

and substitute (5). The result is the complex sensitivity expression

$$\left(\frac{df}{dp_i} \right)_{AVM-I} \approx \frac{\partial f}{\partial p_i} + \hat{\mathbf{x}}^H \cdot \left[\frac{\Delta_i \mathbf{b}}{\Delta p_i} - \frac{\Delta_i \mathbf{A}}{\Delta p_i} (\mathbf{x} + \Delta_i \mathbf{x}) \right], \quad (12)$$

$i = 1, \dots, N$

where $\hat{\mathbf{x}}$ is the solution of the adjoint system,

$$\mathbf{A}^H \hat{\mathbf{x}} = [\nabla_{\mathbf{x}} f]^H. \quad (13)$$

Here, \mathbf{A}^H is the Hermitian of the system matrix \mathbf{A} in (1), obtained by transposition and conjugation of \mathbf{A} . \mathbf{A}^H is also called adjoint to \mathbf{A} in analogy with adjoint operators in functional space analysis. As per (9), the adjoint excitation can be defined as

$$[\nabla_{\mathbf{x}} f]^H = \left[\left(\frac{\partial f_R}{\partial x_{1R}} + j \frac{\partial f_R}{\partial x_{1I}} \right) \dots \left(\frac{\partial f_R}{\partial x_{MR}} + j \frac{\partial f_R}{\partial x_{MI}} \right) \right]^T. \quad (14)$$

If f is a real function [8], then

$$\begin{aligned} \frac{df}{dp_i} \approx & \frac{\partial f}{\partial p_i} + \\ & \text{Re} \left\{ \hat{\mathbf{x}}^H \cdot \left[\frac{\Delta_i \mathbf{b}}{\Delta p_i} - \frac{\Delta_i \mathbf{A}}{\Delta p_i} (\mathbf{x} + \Delta_i \mathbf{x}) \right] \right\}, \quad i = 1, \dots, N \end{aligned} \quad (15)$$

where $\hat{\mathbf{x}}$ is the solution of the adjoint problem (13)-(14) with $f = f_R$. Thus, the computational effort involved in the sensitivity calculations of a complex analytic response function is equivalent to that of a real-valued response function. Note that (12) is a generalization of the sensitivity expression developed in [6], [7] to the complex-variable case.

If f is complex but not analytic, then its real and imaginary parts, f_R and f_I , have to be treated as two

separate response functions, and two separate adjoint systems of the form (13)-(14) must be solved. Consider for example, a complex response function of the form $f = Z_{in} = 1/x_k$, where Z_{in} is the input impedance at a point excited with a 1-volt and has a corresponding current x_k . This response is not differentiable at $x_k = 0$. If the solution is at or very close to this point, we treat $f_R = R_{in} = \text{Re}\{Z_{in}\}$ and $f_I = X_{in} = \text{Im}\{Z_{in}\}$ as two separate real-valued response functions. As a consequence, two adjoint systems must be solved.

Below we summarize the features of the sensitivity formulas (12), (15):

- The adjoint vector $\hat{\mathbf{x}}$ requires one additional system analysis (13) (unless LU decomposition is used to solve (1), such that the analysis is reduced to forward-backward substitutions [8]). The adjoint problem (13) is perturbation independent.
- The perturbed original system solutions, $\mathbf{x} + \Delta_i \mathbf{x}$, $i = 1, \dots, N$ are perturbation dependent, and thus require N additional system analyses. This drawback is overcome with suitable approximations as explained later.
- No assumptions are made for the magnitudes of the system matrix variations $\Delta_i \mathbf{A}$, $i = 1, \dots, N$; the ratio $\Delta_i \mathbf{A} / \Delta p_i$ does not need to represent the respective system matrix derivative with high fidelity, and, in general, it *should not* be considered its finite-difference approximation.
- If, however, $\Delta_i \mathbf{A}$, $i = 1, \dots, N$, are sufficiently small, the second-order terms $\Delta_i \mathbf{A} \cdot \Delta_i \mathbf{x}$ in (4) can be neglected, thus, leading to the familiar first-order exact sensitivity expression [8]:

$$\frac{df}{dp_i} = \frac{\partial f}{\partial p_i} + \hat{\mathbf{x}}^H \cdot \left(\frac{d\mathbf{b}}{dp_i} - \frac{d\mathbf{A}}{dp_i} \mathbf{x} \right), \quad i = 1, \dots, N. \quad (16)$$

The first-order sensitivity expression (16) is applicable with numerical solvers utilizing unstructured grids because such grids allow for a continuous spectrum of values of the design shape parameters. This makes the arising system matrices differentiable with respect to the shape parameters. However, (16) is not suitable for structured-grid algorithms where allowable shape perturbations include only discrete on-grid parameter values. In this case, the second-order sensitivity expression (12) yields better accuracy.

Our technique can be summarized in the following steps:

1. *Parameterization*: specify the set of links L whose corresponding \mathbf{A} -coefficients are affected by the perturbations Δp_i , $i = 1, \dots, N$.
2. *Original system analysis*: (a) solve the original system (1); (b) store the incident voltages for all the links in the set L ; (c) store the incident voltages in the observation domain to be used in the computation of the derivatives for the adjoint excitation (14).

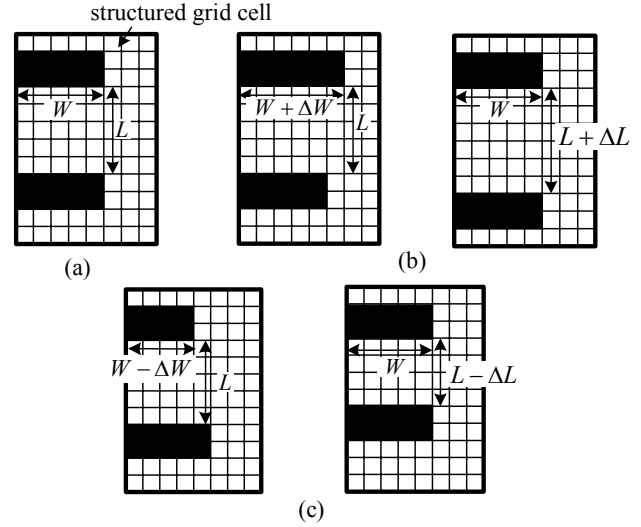


Fig. 1. Discrete on-grid perturbations of the boundaries: (a) the nominal structure; (b) a forward perturbation in W and L ; (c) a backward perturbation in W and L .

3. *Adjoint analysis*: solve the adjoint problem (13) and store \mathbf{x} in the locations that correspond to the set L and the nonzero elements of $\Delta_i \mathbf{b}$, $i = 1, \dots, N$.
4. *Approximation of the N perturbed problems*: find $\mathbf{x} + \Delta_i \mathbf{x}$ by performing a mapping between the solutions of the original problem and the perturbed problems for the elements of \mathbf{x} that correspond to L . See [7] for more details.
5. *Sensitivities estimation*: evaluate the sensitivities using (12) for all N parameters.

C. Second-order Sensitivity Expression II (AVM-II)

An alternative to (5) is [9]

$$\Delta_i \mathbf{x} = (\mathbf{A} + \Delta_i \mathbf{A})^{-1} (\Delta_i \mathbf{b} - \Delta_i \mathbf{A} \cdot \mathbf{x}). \quad (17)$$

Repeating all other steps as above, another possible complex sensitivity expression emerges,

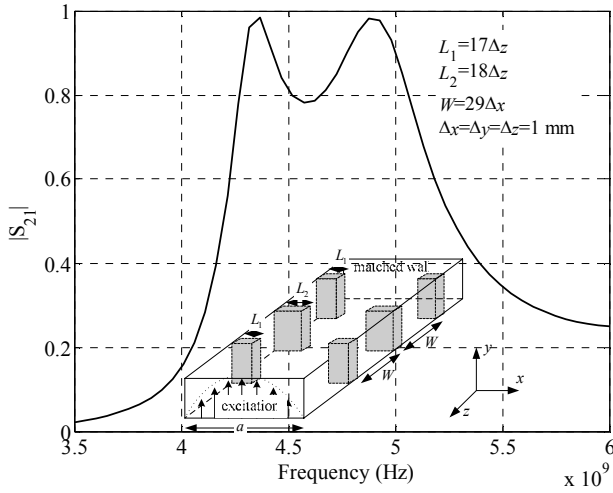
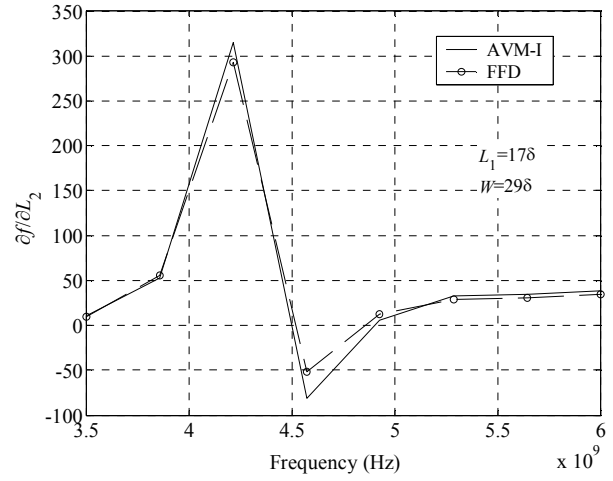
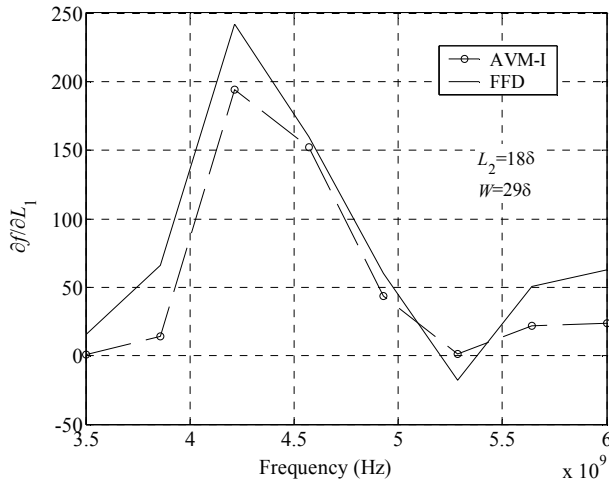
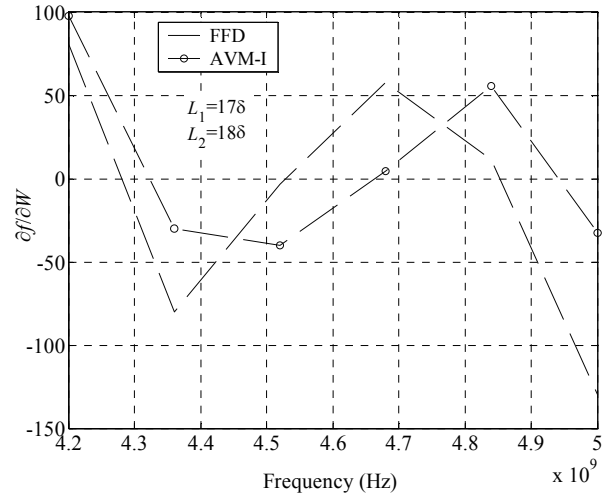
$$\left(\frac{df}{dp_i} \right)_{AVM-II} \approx \frac{\partial f}{\partial p_i} + \hat{\mathbf{x}}_i^H \cdot \left(\frac{\Delta_i \mathbf{b}}{\Delta p_i} - \frac{\Delta_i \mathbf{A}}{\Delta p_i} \mathbf{x} \right), \quad i = 1, \dots, N. \quad (18)$$

This time, the unperturbed original problem solution \mathbf{x} is used, but the adjoint solution vector $\hat{\mathbf{x}}_i$ is perturbation dependent since the complex adjoint problem appears as

$$(\mathbf{A} + \Delta_i \mathbf{A})^H \hat{\mathbf{x}}_i = [\nabla_{\mathbf{x}} f]^H, \quad i = 1, \dots, N. \quad (19)$$

Note that neglecting the second-order term in (4) or (17), in this case, too, reduces (18) to the first-order sensitivity formula (16).

This technique can be summarized with the same steps as those of the AVM-II technique. The only difference is that steps 2 (original system analysis) and 3 (adjoint system analysis) are swapped, i.e., perturbations take place in the adjoint system and not the original system. See [9] for more details.


 Fig. 2. Insertion loss $|S_{21}|$ of the filter.

 Fig. 4. Derivative of f with respect to L_2 vs. frequency.

 Fig. 3. Derivative of f with respect to L_1 vs. frequency.

 Fig. 5. Derivative of f with respect to W vs. frequency.

The two second-order sensitivity expressions (12) and (18), although theoretically equivalent, exhibit some differences when implemented in practical algorithms. This is mainly due to the self-dependence of the variations in the state variable term in (5), i.e., $\Delta_i \mathbf{x}$ appears in both sides of (5) and is hence computed from its own approximation. As a result, we expect the computational error in this term to increase especially with highly nonlinear responses. Notice that, this is not the case in (17) [8].

In general, neither (3)-(12) nor (18)-(19) are actually solved for a perturbation in each of the N parameters. Instead, the values of $\Delta_i \mathbf{x}$ are approximated using a simple mapping [6], [7], [9]. The concept is based on the perturbation theory [10], and it can be implemented for conducting and dielectric parameters.

D. Central Approaches with Sensitivity Expressions

As mentioned earlier, with structured grid solvers, allowable perturbations are limited to multiples of the grid size in the respective direction. For example, consider the structure in Fig. 1. The dark rectangles may be either conducting or dielectric objects. The nominal design of this structure is shown in Fig. 1 (a) where $\mathbf{p} = [L \ W]^T$ is the vector of design parameters. AVM-I (12) can be used when perturbations in the forward direction [see Fig. 1(b)] take place in the original problem. It can also be used when perturbations are in the backward direction [see Fig. 1(c)]. The sensitivity results obtained from the forward and backward perturbations are somewhat different especially when the response \mathbf{R} is a highly nonlinear function of \mathbf{p} . The same forward, backward and central approaches can be applied with the AVM-II (18).

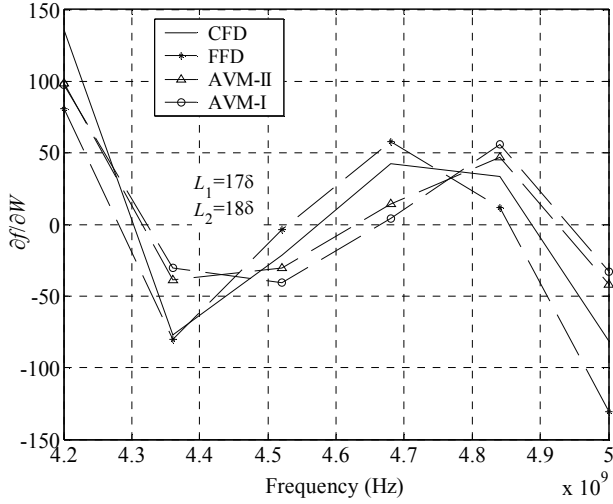


Fig. 6. A Comparison between response level sensitivities and adjoint-based sensitivities.

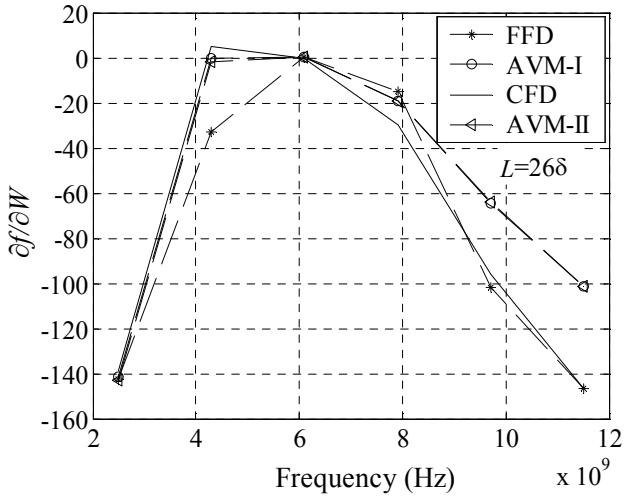


Fig. 8. Derivative of f with respect to W for the printed filter.

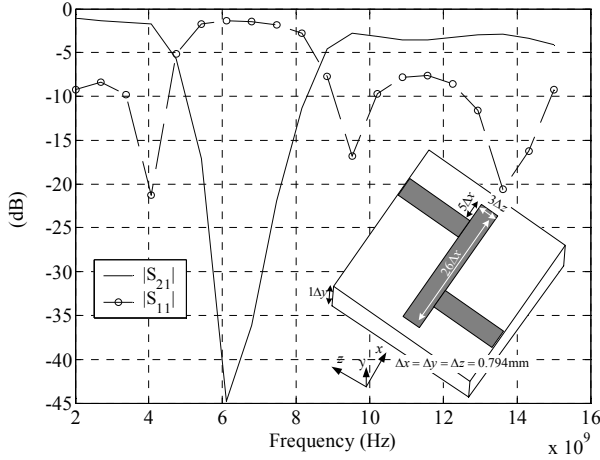


Fig. 7. Reflection and transmission coefficients of the printed filter.

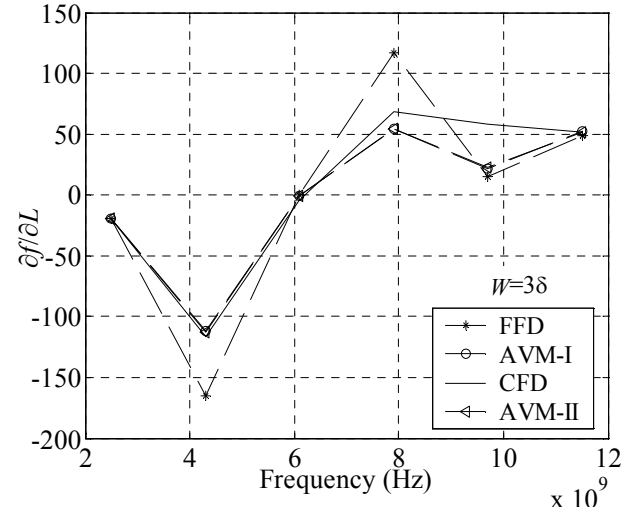


Fig. 9. Derivative of f with respect to L for the printed filter.

Major improvement in the accuracy can be achieved using the central adjoint approach [11]. The central formula (CAVM-I) combines the solutions of the forward and backward sensitivity expressions. Its complex form is

$$\left(\frac{df}{dp_i}\right)_{CAVM-I} \approx \frac{\partial f}{\partial p_i} + \hat{\mathbf{x}}^H \cdot \left\{ \frac{\Delta_i \mathbf{b}^+ + \Delta_i \mathbf{b}^-}{2\Delta p_i} - \frac{\Delta_i \mathbf{A}^+ \mathbf{x}_i^+ + \Delta_i \mathbf{A}^- \mathbf{x}_i^-}{2\Delta p_i} \right\}, \quad i=1, \dots, N. \quad (20)$$

In (20), the plus sign (+) refers to a perturbation in the forward direction and the minus sign (-) refers to that in the backward direction.

Since we have observed that the computational error is, in fact, reduced with AVM-II (18), we consider here the same forward/backward procedure and derive a central formula for AVM-II (CAVM-II) as well:

$$\left(\frac{df}{dp_i}\right)_{CAVM-II} \approx \frac{\partial f}{\partial p_i} + \frac{\hat{\mathbf{x}}_i^H \Delta_i \mathbf{b}^+ + \hat{\mathbf{x}}_i^H \Delta_i \mathbf{b}^-}{2\Delta p_i} - \frac{\hat{\mathbf{x}}_i^H \Delta_i \mathbf{A}^+ + \hat{\mathbf{x}}_i^H \Delta_i \mathbf{A}^-}{2\Delta p_i} \cdot \mathbf{x}, \quad i=1, \dots, N. \quad (21)$$

The improvement in the accuracy due to the central formulas (20) and (21) is, in some cases, very significant over the sensitivity results produced by formulas (12) and (18). Note however, that the computational load is the same for all four approaches.

III. EXAMPLES AND COMPARISONS

In this section, we show sensitivity results computed with our adjoint techniques through a variety of different structures. The structures are chosen so that: (i) different types of perturbations are possible, i.e., volumetric

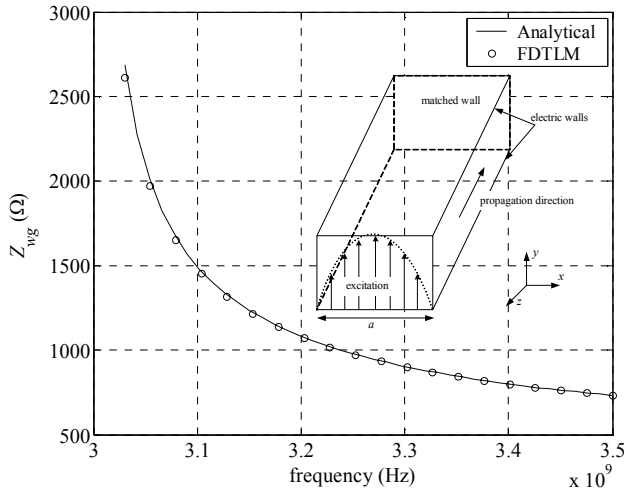


Fig. 10. The wave impedance of the waveguide vs. frequency at $a = 5$ cm.

perturbations, as in waveguide structures, as well as metallic surface perturbations in printed structures; and (ii) the selected response is a highly nonlinear function of its design parameters.

The adjoint results are compared with those computed using classical finite differences at the level of the response or with sensitivity results calculated analytically whenever available.

The structures are simulated using an in-house simulator based on the frequency-domain transmission line method (FDTLM) [12]. A uniform discretization grid is used, i.e., $\Delta x = \Delta y = \Delta z = \delta$ and $\Delta p_i = \delta$.

A. Results with AVM-I

Using AVM-I, we compute response sensitivities for the double-resonator filter shown in the inset of Fig. 2 for a range of frequencies. The filter is analyzed for its dominant mode and thus the problem reduces to two dimensions. The computational size of the problem is $30 \times 1 \times 120 \delta$. The filter is excited with a uniform half sine-wave at its input port. The input and output ports are matched to absorb the reflected waves.

The response function is defined as $f = |S_{21}|$, where S_{21} is the transmission coefficient for the filter. The response is shown in Fig. 2. The vector of design parameters is $\mathbf{p} = [L_1 \ L_2 \ W]^T$, where L_2 and L_1 are the lengths of the middle and side septa, respectively. W is the separation between the septa.

For comparison, the sensitivities are also computed using forward finite differences (FFD) directly at the level of the response [Figs. 3, 4, and 5].

TABLE 1
COMPARISON BETWEEN THE DERIVATIVES FROM THE CONVERGENCE ANALYSIS.

δ	$\rightarrow 0$	$\lambda/80$	$\lambda/20$	$\lambda/10$
• analytical		-1.244		
• AVM-I	-1.2471	-1.2481	-1.2530	-1.2550
• CAVM-I	-1.2470	-1.2480	-1.2510	-1.2520
• AVM-II	-1.2459	-1.2471	-1.2500	-1.2513
• CAVM-II	-1.2455	-1.2460	-1.2481	-1.2501

B. Results with AVM-II and Comparisons with AVM-I

1) Double-resonator Filter

For the same double-resonator filter shown in Fig. 2, we compute the sensitivity results for $f = |S_{21}|$ with respect to W using AVM-II. The results are compared with those produced with AVM-I from Section III.A as shown in Fig. 6. For better comparison of the accuracies of AVM I and II, we compute a reference sensitivity using the second-order central finite differences (CFD) at the level of the response. Notice that this is a highly nonlinear response function. Even with a relatively fine grid, the FFD and CFD sensitivities disagree. Results computed with AVM-II show acceptable accuracy compared to the reference CFD and a noticeable improvement over those computed using AVM-I.

2) Microstrip Low-pass Filter

With this example, the perturbations are of infinitesimal surface type. The relative permittivity of the substrate is $\epsilon_r = 2.2$. The total size of the simulated problem is $43 \times 37 \times 7 \delta$. We excite the structure with a voltage source applied uniformly underneath the strip-line at port 1 in the y -direction.

We compute the sensitivities for the printed low-pass filter shown in the inset of Fig. 7. The response function is the squared modulus of the transmission coefficient of the filter, i.e., $f = |S_{21}|^2$ [see Fig. 7]. The vector of design parameters is $\mathbf{p} = [L \ W]^T$, where L is the length of the resonating element and W is its width.

The sensitivities are computed with respect to changes in the vector of design parameters $\mathbf{p} = [L \ W]^T$ using both AVM I and II. The computed results are compared with first and second-order finite difference estimates at the level of the response as shown in Figs. 8 and 9.

As seen from this example, the difference between the adjoint-based sensitivities is small. This is also true for the results from the previous example when the sensitivities are computed with respect to changes in L_1 and L_2 [see Fig. 2]. It is thus difficult to conclude with certainty which approach provides better accuracy. Therefore, more detailed comparison based on convergence analysis is needed.

C. Convergence Analysis

In this section, we test the accuracy of our adjoint approaches presented in Sections II.B to II.D through a convergence test, i.e., we compute the sensitivity of a response function using each of the four approaches at a given design, and compare their accuracy as the grid size δ becomes smaller. For this test to be accurate, we choose a response function that is analytically available, and therefore, its derivative can be calculated analytically. We consider the wave impedance ($f = Z_{wg}$) of a hollow rectangular waveguide [see the inset of Fig. 10]. The computed adjoint derivatives are compared to the analytical derivative.

The response is calculated analytically using the well-known formula for Z_{wg} as a function of the waveguide cross-section dimensions and the frequency [13]. The response function is also computed using our FDTLM simulator as shown in Fig. 10.

The convergence analysis is executed at a given design point in the highly nonlinear region of the response function [see Fig. 10]. For example, consider the design where the waveguide width is $a = 5$ cm and the frequency is 3.05 GHz. For this design, the four adjoint sensitivities are computed for different uniform discretization grid of the TLM simulator, i.e., at $\delta = \lambda/10$ to $\delta = \lambda/80$, where λ is the wavelength. The derivatives for a finer grid at $\delta \rightarrow 0$ are estimated using Matlab's [14] extrapolating functions. The results are given in Table 1.

The results show that all four approaches tend to converge to the analytical value of the derivative as the grid size δ becomes finer. This is due to the dependence of the field approximation in the perturbed problems [7] on the grid size. It can also be observed that the results produced with CAVM-II give the best outcome for any grid size compared to the other results. The CAVM-II results also show a smoother convergence than the other approaches. Our interpretation to this outcome is: (i) the numerical error produced by the sensitivity expression II (18) is less than that of sensitivity expression I (12); and (ii) the CAVM, in general, preserves the advantages of the second-order term $\Delta_i \mathcal{A} \cdot \Delta_i \mathbf{x}$ since it takes into account both forward and backward perturbations in the design parameter. With the CAVM-II, we merge the above advantages and obtain the best results.

It is also observed that the difference between the AVM-I and CAVM-I derivatives at finer grid sizes is small. However, we would like to point out that larger differences are expected with responses that are functions of shape design parameters in which the electromagnetic field is singular at the locations of the perturbed boundaries [11]. There are no field singularities in our waveguide example as the field smoothly decays to zero at the edge of the electric conducting walls of the waveguide. Therefore, the field variations between the approximated perturbed solution and that of the original

unperturbed problem are not very different. Hence, the difference in the corresponding derivatives is not so pronounced.

IV. CONCLUSIONS

We present a framework of approaches for feasible and versatile adjoint-based sensitivity analysis with frequency-domain structured-grid electromagnetic solvers. For the first time, we present two new adjoint-based approaches that further improve the accuracy of the estimated sensitivities. All approaches are easy to implement with existing solvers and do not require solver-dependent analytical preprocessing. They provide cheap and accurate gradient information, which is valuable in a number of CAD applications such as optimization, modeling, and tolerance analysis.

We also test and compare the accuracy of our presented approaches through the computed sensitivities of a variety of structures and through robust convergence analysis. Conclusions are made based on comparisons with finite difference response-level sensitivities and with analytical derivatives.

REFERENCES

- [1] E. J. Haug, K. K. Choi and V. Komkov, *Design Sensitivity Analysis of Structural Systems*. Orlando: Academic Press Inc., 1986.
- [2] A. D. Belegundu and T. R. Chandrupatla, *Optimization Concepts and Applications in Engineering*. Upper Saddle River, NJ: Prentice Hall, 1999.
- [3] I.-H. Park, I.-G. Kwak, H.-B. Lee, S.-Y. Hahn and K.-S. Lee, "Design sensitivity analysis for transient eddy current problems using finite element discretization and adjoint variable method," *IEEE Trans. Mag.*, vol. 32, pp. 1242-1245, May 1996.
- [4] J.P. Webb, "Design sensitivity of frequency response in 3-D finite-element analysis of microwave devices," *IEEE Trans. Mag.*, vol. 38, No. 2, pp. 1109-1112, Mar. 2002.
- [5] J. W. Bandler, Q.-J. Zhang and R. M. Biernacki, "A unified theory for frequency-domain simulation and sensitivity analysis of linear and nonlinear circuits," *IEEE Trans. MTT*, vol. 36, pp. 1661-1669, Dec. 1988.
- [6] M. H. Bakr and N. K. Nikolova, "An adjoint variable method for frequency domain TLM problems with conducting boundaries," *IEEE Microwave Wireless Components Lett.*, vol. 13, pp. 408-410, Sep. 2003.
- [7] S. M. Ali, N. K. Nikolova and M. H. Bakr, "Sensitivity analysis with full-wave EM solvers based on structured grids," *IEEE Trans. Mag.*, vol. 40, No. 3, pp. 1521-1529, May, 2004.
- [8] N. K. Nikolova, J. W. Bandler and M. H. Bakr, "Adjoint techniques for sensitivity analysis in high-frequency structure CAD," *IEEE Trans. MTT*, vol. 52, No. 1, pp. 403-419, Jan. 2004.
- [9] S. M. Ali, N. K. Nikolova, and M. H. Bakr, "Sensitivity analysis and optimization utilizing an approximate auxiliary problem," *IEEE/URSI Int. Symposium on Antennas and Propagation*, June 2004 (Monterey, CA), vol.1, pp. 1118-1121.
- [10] R. F. Harrington, *Time-Harmonic Electromagnetic Fields*. New York: McGraw-Hill book company, Inc., 1961.

- [11] S. M. Ali, N. K. Nikolova, and M. H. Bakr, "Central adjoint variable method for sensitivity analysis with structured grid electromagnetic solvers," *IEEE Trans. Mag.*, pp. 1969-1971, July, 2004.
- [12] D. Johns and C. Christopoulos, "New frequency-domain TLM method for the numerical solution of steady-state electromagnetic problems," *IEE Proc. Sci Meas. Technol.*, vol. 141, pp. 310-316, 1994.
- [13] D. M. Pozar, *Microwave Engineering*. New York: Addison-Wesley Publishing Company, Inc., 1993.
- [14] MATLAB (2000) Version 6.0, MathWorks, Inc., 3 Apple Hill Drive, Natick MA 01760-2098.



Shirook M. Ali received the B.Sc. degree from University of Baghdad, Iraq, in 1993, and the M.Sc. degree from Jordan University of Science and Technology, Jordan, in 1999. She is currently working toward her Ph.D. at McMaster University, Canada. Her research interests include computational electro-

magnetics, optimization, and CAD methods for high-frequency structures and antennas.



Natalia K. Nikolova received the Dipl. Eng. degree from the Technical University of Varna, Bulgaria, in 1989, and the Ph.D. degree from the University of Electro-Communications, Tokyo, Japan, in 1997. From 1998 to 1999, she held a Postdoctoral Fellowship of the Natural Sciences and Engineering Research Council of Canada (NSERC), during which time she was initially with

the Microwave and Electromagnetics Laboratory, DalTech, Dalhousie University, Halifax, Canada, and, later, for a year, with the Simulation Optimization Systems Research Laboratory, McMaster University, Hamilton, ON, Canada. In July 1999, she joined the Department of Electrical and Computer Engineering, McMaster University, where she is currently an Associate Professor. Her research interests include theoretical and computational electromagnetism, high-frequency analysis techniques, as well as CAD methods for high-frequency structures and antennas.

Dr. Nikolova currently holds a University Faculty Award of NSERC, which she received in 2000, and which was renewed in 2003.



Mohamed H. Bakr received a B.Sc. degree in Electronics and Communications Engineering from Cairo University, Egypt in 1992 with distinction (honors). In June 1996, he received a Master's degree in Engineering Mathematics from Cairo University. In 1997, he was a student intern with Optimization Systems Associates (OSA), inc. From 1998 to 2000, he worked as a research assistant with the Simulation Optimization Systems (SOS)

research laboratory, McMaster University, Hamilton, Ontario, Canada. He earned the Ph.D. degree in September 2000 from the Department of Electrical and Computer Engineering, McMaster University. In November 2000, he joined the Computational Electromagnetics Research Laboratory (CERL), University of Victoria, Victoria, Canada as an NSERC Post Doctoral Fellow. Dr. Bakr is a recipient of a 2003 Premier's Research Excellence Award (PREA) from the province of Ontario, Canada. His research areas of interest include optimization methods, computer-aided design and modeling of microwave circuits, neural network applications, smart analysis of microwave circuits and efficient optimization using time/frequency domain methods. He is currently an Assistant Professor with the Department of Electrical and Computer Engineering, McMaster University.

Advanced FVTD Simulation of Dielectric Resonator Antennas and Feed Structures

Christophe Fumeaux, Dirk Baumann, Rüdiger Vahldieck
 Swiss Federal Institute of Technology, ETHZ, IFH, 8092 Zürich, Switzerland
 E-mail: fumeaux/dbaumann/vahldieck@ifh.ee.ethz.ch

Abstract—This paper illustrates the application of the Finite-Volume Time-Domain (FVTD) method to the electromagnetic modeling of complex 3D antenna structures. The FVTD algorithm solves Maxwell's equations in a conformal polyhedral mesh, therefore permitting an accurate approximation of curved surfaces and a fine resolution of structural details. The flexibility of the unstructured mesh is coupled with a geometry-matched local time-stepping scheme to increase the computational efficiency. The FVTD algorithm is applied here to simulate probe-fed hemispherical dielectric resonator antennas. Emphasis of the investigation is placed on the modeling of fabrication details and their influence on the input impedance and resonance frequency of the device.

Index Terms—3D FVTD method, conformal meshing, dielectric resonator antenna

I. INTRODUCTION

The Finite-Volume Time-Domain (FVTD) method has been introduced at the end of the 1980's [1], [2] as a powerful technique for numerically solving Maxwell's equations in unstructured meshes. Typically, the FVTD algorithm is applied in a tetrahedral mesh, therefore avoiding stair-casing approximations for the discretization of curved or non-orthogonal surfaces. The FVTD method stands therefore as an alternative to the Finite-Difference Time-Domain (FDTD) method for complex geometries where conformal meshing is advantageous.

Another important characteristic of unstructured meshes is their ability to adapt the cell size to the local geometrical requirements. Since the transition between domains with different feature sizes can be made very fast, the number of cells in the computational domain can be minimized without sacrificing the resolution. Modeling small structural details, e.g. the feed of an antenna, in close proximity to large structures is a frequently encountered practical problem. A solution to this problem strongly benefits from different scales of cell sizes: In the coarse regions of the problem, the standard linear cell dimension will be determined by a fraction of the shortest wavelength of interest (typically $\lambda/10$), whereas resolution of details might require much smaller cell dimensions (e.g. in the order of $\lambda/100$ or smaller). Another advantage of inhomogeneous meshes consists in the modeling of boundaries between materials with a large dielectric contrast. The shorter wavelength in the denser material

requires finer cell sizes than in free-space, which can be achieved straightforwardly in an unstructured tetrahedral mesh. Since the FVTD method keeps the number of needed cells to a minimum in complex problems, it saves memory despite a computationally higher expense for a single cell (geometrical data are required) compared to FDTD.

Simulations of dielectric resonator antennas (DRA) are very challenging problems that can take advantage of the geometrical flexibility of the FVTD method: A DRA typically includes curved boundary surfaces with a large dielectric contrast, and small feeding mechanisms. In this investigation, a hemispherical DRA fed by a coaxial probe is modeled. The effects of different probe configurations and of fabrication imperfections are studied numerically. The results demonstrate the versatility of the FVTD technique.

II. THE FVTD ALGORITHM

The FVTD method is based on Maxwell's equations written in conservative form and integrated over elementary volumes [3]. The implementation in a digital computer requires the approximation of the equations in each elementary volume of a given spatial grid. In a tetrahedral mesh, each volume V_i has 4 faces with areas F_k and outward-pointing unit normal vector \vec{n}_k . This yields the following vector equations

$$\begin{aligned} -\mu V_i \frac{\partial}{\partial t} \langle \vec{H} \rangle_{V_i} &= \sum_{k=1}^4 \left(\vec{n}_k \times \langle \vec{E} \rangle_{F_k} \right) F_k \\ \epsilon V_i \frac{\partial}{\partial t} \langle \vec{E} \rangle_{V_i} &= \sum_{k=1}^4 \left(\vec{n}_k \times \langle \vec{H} \rangle_{F_k} \right) F_k \end{aligned} \quad (1)$$

The left-hand side (LHS) of (1) represents a volume integral, where the triangular brackets denote the averaging of the field components over the considered volume. This average is approximated by the value of the fields in the barycenter of the tetrahedron. The right-hand side (RHS) of (2) represents a sum of surface integrals over the faces of the considered finite volume. The integrands are so-called (mathematically defined) "fluxes" through the faces of the cells. The triangular brackets represent the averaging of the fields over each face of the tetrahedron. The approximation locates the average field components in the barycenter of the considered face.

The interaction between adjacent cells in the FVTD algorithm happens, as inspired by FV techniques in fluid

dynamics, through separation of the flux terms in incoming (-) and outgoing (+) contributions (split-flux formulation [3])

$$\begin{aligned}
 -\mu V_i \frac{\partial}{\partial t} \langle \vec{H} \rangle_{V_i} &= \sum_{k=1}^4 \left(\vec{n}_k \times \langle \vec{E} \rangle_{F_k}^+ - \vec{n}_k \times \langle \vec{E} \rangle_{F_k}^- \right) F_k \\
 \varepsilon V_i \frac{\partial}{\partial t} \langle \vec{E} \rangle_{V_i} &= \sum_{k=1}^4 \left(\vec{n}_k \times \langle \vec{H} \rangle_{F_k}^+ - \vec{n}_k \times \langle \vec{H} \rangle_{F_k}^- \right) F_k
 \end{aligned} \quad (2)$$

Explicit update equations for the fields in the finite volumes are obtained by discretizing the time variable in (2). Different time-marching schemes can be applied for this purpose. In a first-order approximation, the $\partial/\partial t$ is estimated using a finite difference. In the algorithm implemented for this study, the second-order Lax-Wendroff predictor-corrector scheme [3] is used. A significant increase of the efficiency of the FVTD march-in-time iteration is obtained through the application of geometry-matched local time steps [4].

A. Local Time Steps

The local time step technique is based on a special partition of the computational domain into sub-domains. This partition is performed automatically during preprocessing based on local geometric and material conditions of the elements in the mesh. To obtain a robust and precise local time step scheme, three restrictions are set on the sub-domain partition:

- 1) The partition defines only discrete levels of local time steps that correspond to power of two times Δt ($\Delta t, 2\Delta t, 4\Delta t, 8\Delta t, \dots$), where Δt is the fundamental time step that assures stability in the whole mesh.
- 2) The time steps of two adjacent sub-domains must have a ratio of two. Thus, multiple scale problems produce nested sub-domains.
- 3) The local time step for all elements in each sub-domain satisfies the stability condition.

A division of the computational domain satisfying these three conditions is performed using an iterative process described in [4]. The restrictions imposed on the partition allow a treatment of the borders between sub-domains as generic two-level boundaries, which are inserted very naturally in the FVTD march-in-time iteration. The time consistency is preserved by introducing an artificial half-step in the larger cells of a time-step boundary. The principle is demonstrated in Fig. 1 for first-order march in time. A boundary between the first and the second level of time step is depicted, but the procedure is similar for all other time step levels. The values of the fields in the higher level boundary cell are required at time step $n+1$ to perform the second small time step (③, from $n+1$ to $n+2$) in the lower level cell. Since the fields at this time step are not computed explicitly in the large cells, these values are obtained through averaging the fields computed at time steps n and $n+2$ (operation denoted by ②). It is therefore necessary to perform the update of the larger cell (①a from n to $n+2$) before the second update in the smaller cell (③, from $n+1$ to $n+2$). The technique is described here for a first-order time discretization but can be extended to more sophisticated schemes as shown in [4].

The less frequent update of larger cells in the mesh allows a significant speedup of the computations when different element scales are present in the simulated structures. Although the update of a cell at the boundary between sub-domains requires around two times more CPU time than a standard cell at the same time-step level, this does not slow down the computation significantly since boundary cells represent only a few percent of the total number of cells.

The local time step scheme used in this study has proven to be very accurate and robust since it requires no space interpolation and only simple time interpolations. Therefore, the fundamental time step does not require a more severe stability condition than the original algorithm. This has been confirmed in all examples computed in practice, involving up to 8 nested levels of time steps (from Δt to $256\Delta t$).

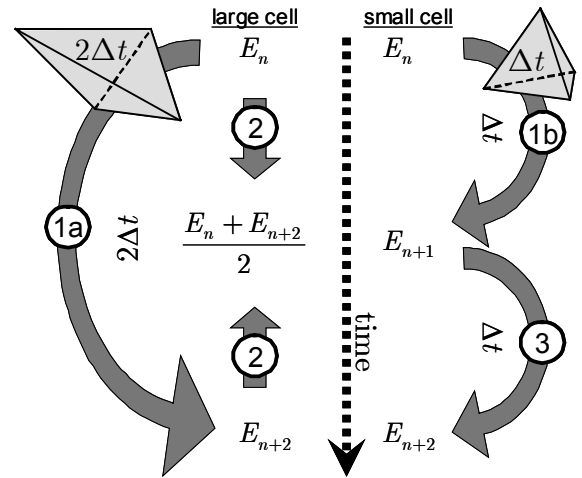


Fig. 1. Principle of application for local time steps at the boundary between sub-domains (two-level system). The chronology is indicated by the encircled numbers. An artificial half-step ② is created in the large cell to obtain data required to perform the update ③.

B. Near-Field to Far-Field Transformation

The far-field patterns are computed using a Huygens' surface enclosing the antenna. This triangulated closed surface is embedded in the tetrahedral mesh. A discrete Fourier transformation (DFT) is performed on the fly during the FVTD iteration to obtain the necessary frequency-domain tangential fields in the center of each triangle of the Huygens' surface. The sampling frequency of the DFT is determined by the local time step of the sub-domain where the sampled fields are located.

C. Ports

Port planes are introduced as triangulated surfaces in the FVTD mesh. The planes force the tetrahedrons to be aligned with respect to one face and therefore form a phase reference plane for the incident and the reflected waves.

The flux-splitting formulation in (2) is exploited to compute the incident and the reflected fields in a port plane consisting of N triangles. This allows to directly calculate power waves without the need to determine voltages and currents in the port by [5].

$$a(n)^2 = \sum_{k=1}^N (\mathbf{E}_t^+(k, n) \times \mathbf{H}_t^+(k, n)) F_k \quad (3)$$

$$b(n)^2 = \sum_{k=1}^N (\mathbf{E}_t^-(k, n) \times \mathbf{H}_t^-(k, n)) F_k$$

where the subscript t denotes tangential fields and the superscripts $+$ and $-$ indicate incident and reflected fields. In a multimode environment the total field in a waveguide can be expressed as a sum over all possible modes. Due to the orthogonality of the modes, the mode amplitude of each mode can be determined. Thus the amplitude $A_m^{+/-}(n)$ of the m th mode at time step n can be computed with

$$A_m^{+/-}(n) = \sum_{k=1}^N \mathbf{E}_t^{+/-}(k, n) \cdot \mathbf{e}_m(k) F_k \quad (4)$$

if the normalized mode template vector \mathbf{e}_m is known a priori. The power waves can then be computed as

$$a = A^+ / \sqrt{Z_w}$$

$$b = A^- / \sqrt{Z_w} \quad (5)$$

with Z_w being the wave impedance.

III. THE HEMISPHERICAL DIELECTRIC RESONATOR ANTENNA

Dielectric resonators placed in an open environment can be used as radiating elements showing such attractive characteristics as small size, large bandwidth, high efficiency and simplicity of excitation [6]. Numerous shapes of resonators have been used including rectangles, cylinders, rings and hemispheres. The coupling of power to the dielectric structure can be achieved through coaxial probes, apertures, microstrip, or coplanar lines. Most of the designs exhibit a large dielectric contrast to free-space and at the same time small feed dimensions. The FVTD method seems therefore perfectly suited to investigate this class of antennas.

To illustrate the advantages of the FVTD simulations, a hemispherical probe-fed dielectric resonator antenna with characteristics close to the devices presented in [7] and [8] is chosen. The geometry is depicted in Fig. 2 showing all the relevant dimensions. The feed configuration excites the TE_{111} mode of the DRA with a resonant frequency in the vicinity of 3.6 GHz. The results of the FVTD simulations have been compared previously [9] with those of a finite-element based commercial program, showing a good agreement for return loss and radiation patterns. The ground plane is chosen as a circular plate with a radius of 60 mm. The present paper investigates the influence of small details on the characteristics of the device. The resolution of fine features in the simulation yields useful information on the effects of fabrication tolerances that might cause discrepancies from predictions of simplified idealized models. In the following, the effect of the probe shape and length, as well as the influence of air gaps around the probe or between the ground plane and the dielectric will be investigated numerically using the FVTD method.

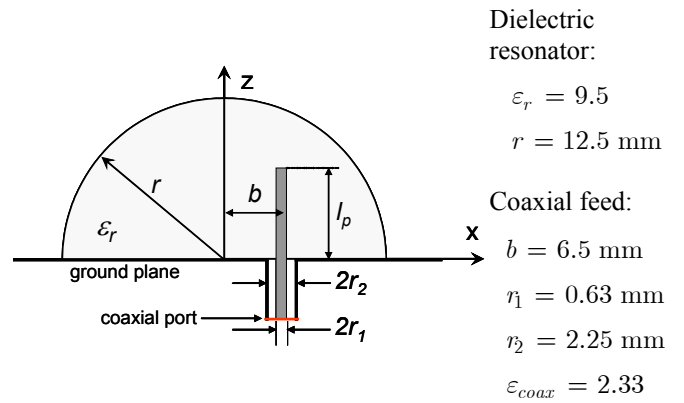


Fig. 2. Schematic cross section of the probe fed hemispherical DRA.

A. General Characteristics of the FVTD Model

The broadband simulation is performed in the frequency range from 3 GHz to 6 GHz. The computational domain is closed by a sphere with radius of 80 mm where a Silver-Müller absorbing boundary condition is applied.

The fineness of the mesh is adapted to the different parts of the devices as shown in Table I and Fig. 3. The resulting ratio of volumes V_{max}/V_{min} in the mesh reaches typically more than 100'000. For an efficient simulation, this spatial inhomogeneity of the mesh is coupled to an inhomogeneous time discretization with up to seven levels of local time steps ($64\Delta t$). A cut through a meshed model is depicted in Fig. 3 showing typical linear cell dimensions associated to different regions of the considered DRA problem. The mesh around the probe is determined by the geometrical resolution desired and might be even finer when an air gap needs to be resolved. The transitions between the different regions of the mesh are smooth in nature in the tetrahedral mesh.

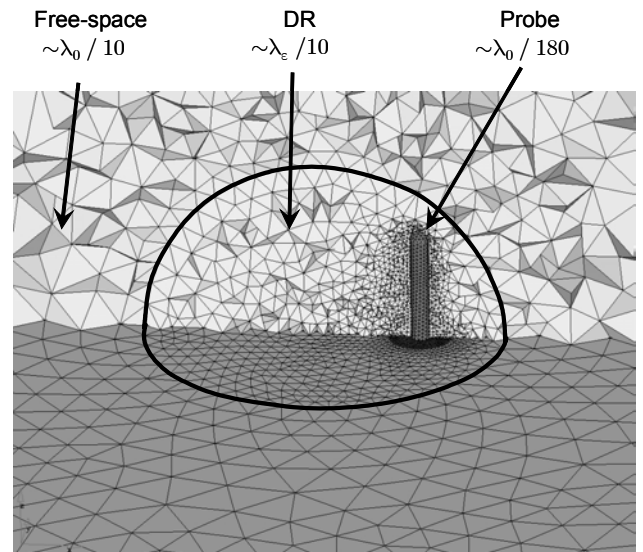


Fig. 3. Cut through the 3D model of the DRA showing the mesh with different fineness adapted to the local geometry. The maximal ratio of volumes in the associated tetrahedral mesh reaches more than 100,000. The presence of thin air gaps in other models results in even larger size contrasts.

TABLE I

TYPICAL LINEAR DIMENSIONS OF THE TRIANGLES USED FOR THE SURFACE DISCRETIZATIONS. THE FINENESS OF THE VOLUME MESH IS DETERMINED BY THE SURFACE DISCRETIZATION. THE NUMBERS IN TERMS OF WAVELENGTHS ARE GIVEN RELATIVE TO THE SHORTEST WAVELENGTH OF INTEREST (I.E., AT 6 GHz).

	Linear dimensions		
	absolute	in terms of λ_0	in terms of λ
Outer boundary	6 mm	$\lambda_0 / 8.3$	$\lambda_0 / 8.3$
DRA surface	1.6 mm	$\lambda_0 / 31.5$	$\lambda_\epsilon / 10$
Probe feed	0.28 mm	$\lambda_0 / 180$	$\lambda_{coax} / 117$
Thinnest air gap (0.05 mm)	0.05 mm	$\lambda_0 / 1000$	$\lambda_0 / 1000$

B. Detailed Model of the Coaxial Probe

The simulations of the hemispherical DRA have been performed for a set of different probe lengths l_p between 1.0 mm and 9.5 mm. The variation of the probe length is a practical way of controlling the input impedance of the DRA. In addition to varying the length, detailed configurations of the probe have been investigated in the frame of this study. Different generic cases are represented in Fig. 4. The probe of the first case (Fig. 4 (a)) is a cut wire with an abrupt end, whereas the probe of the second case (Fig. 4 (b)) has a rounded tip. In the third case, an air gap exists between the probe (rounded tip) and the dielectric material (Fig. 4 (c)). Different thicknesses of air gaps between 0.05 and 0.30 mm have been modeled. All configurations have been considered from the perspective of the matching to 50Ω and from the point of view of the resonant frequency of the DRA. The return loss is a practical value for a specific matching condition but does not yield full information on the exact location of the resonant frequency.

The presence of a thin air gap around the probe requires a finer mesh around the probe than corresponding simulations without air gap. Typical ratios of volumes V_{\max} / V_{\min} are given in Table II for different thicknesses of air gap.

C. Effect of Local-Time Stepping

The local time stepping permits to achieve a significant speedup of the simulation since the large cells in the mesh will

TABLE II
MESH CHARACTERISTICS FOR DIFFERENT MODELS WITH AIR GAP AROUND THE PROBE. THE THICKNESS OF THE AIR GAP IS GIVEN IN MILLIMETER.

Model	# of cells	V_{\max} / V_{\min}	Top level
Air Gap 0.05	379,657	3,675,074	7 ($64 \Delta t$)
Air Gap 0.10	237,213	803,117	7 ($64 \Delta t$)
Air Gap 0.20	212,859	117,411	5 ($16 \Delta t$)
Air Gap 0.30	213,379 *	95,011	5 ($16 \Delta t$)
No air gap	209,443	112,652	5 ($16 \Delta t$)

* The number of elements for air gap 0.20 and 0.30 is very similar since the discretization used on the probe (0.28 mm, Table I) is sufficient to resolve both gap dimensions.

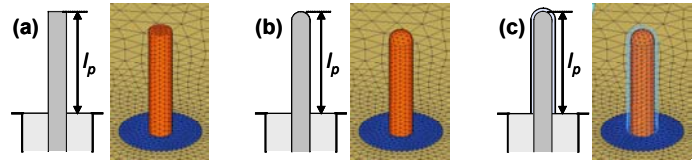


Fig. 4. Different models of the probe: (a) probe with cut end, (b) probe with a rounded tip, (c) probe with a rounded tip and an air gap.

be updated much less often than the small ones. For the type of problems presented here, computation speedup factors of 4 to 10 are achieved using this technique compared to the corresponding simulations performed without local time stepping. The largest speedups are achieved for the most inhomogeneous meshes.

The influence of the local time stepping on the simulation result has been demonstrated to be negligible [4]. In the practical examples presented here, the same conclusions can be applied. As illustration, the field amplitude in one particular point is represented in Fig. 5 together with the difference of the computed values obtained with and without local time stepping. Even when five to seven nested local time-step sub-domains are used, the discrepancies are well below -50 dB.

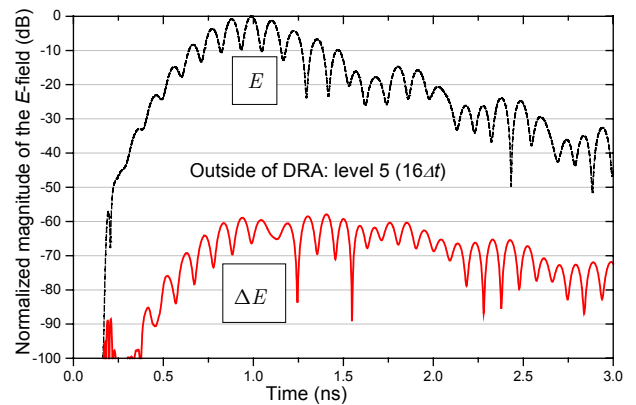


Fig. 5. Influence of the local time stepping on the amplitude of the electric field at a point located outside the DRA. The arbitrarily chosen point is updated with a local time step corresponding to 16 times the fundamental time step. The upper curve (E) shows the E-field magnitude in this point and the lower curve (ΔE) the difference between the simulations performed with and without local time stepping.

IV. DETAILED SIMULATION OF THE DRA

In this section, several features of the probe-fed DRA are investigated. After a general analysis of the effect of the probe length, the emphasis is placed on the modeling of details that might arise from fabrication imperfections [10].

A. Probe Length Dependence

The variation of the probe length represents a very convenient way to control the input impedance of the probe-fed DRA [7]. The return loss of the DRA fed by a $50\ \Omega$ coaxial line is represented for probe length l_p between 5 and 9 mm in Fig. 6. The optimum matching of the antenna for the first resonance located around 3.6 GHz (TE₁₁₁ mode) is obtained for a probe length between 7 mm and 8 mm. Higher-order resonances with different optimum probe lengths are observed around 5.3 GHz and 5.7 GHz (Fig. 7).

These results have been obtained using probes with cut ends (Fig. 4 (a)). The following paragraphs investigate the influence of probe details on the matching condition.

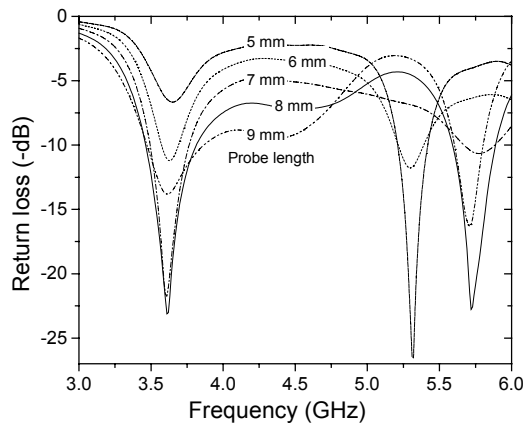


Fig. 6. Return loss (related to $50\ \Omega$ coaxial cable feeding) as a function of the frequency for different probe lengths. The probes used in the models have a cut end.

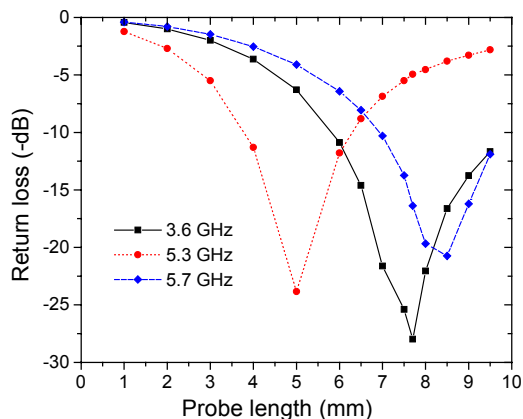


Fig. 7. Return loss as a function of the probe length at three different frequencies.

B. Effect of Rounded Probe Tip

Rounding the tip of the probe makes it appear electrically slightly shorter than a cut-end probe with the same length. This has an influence on the matching of the device and is best

observed on the return loss curves. On the upper graph of Fig. 8, the return loss for a rounded probe with length 6.5 mm remains for all frequencies in between curves for cut-end probes with length 6.0 mm and 6.5 mm. This suggests an "effective length" for the rounded probe between 6.0 mm and 6.5 mm. This particular example has been chosen for illustration since it also shows a higher resonance close to 5.3 GHz. Similar observations are made for all probe lengths.

The lower graph of Fig. 8 considers lengths closer to an optimal matching for $50\ \Omega$ and permits to quantify how shorter a rounded tip appears: The return loss of a rounded probe with 8 mm is nearly identical to the one of a cut-end probe with length 7.7 mm. This reduction corresponds roughly to half the radius of the rounding. Similar conclusions can be drawn for all probe lengths.

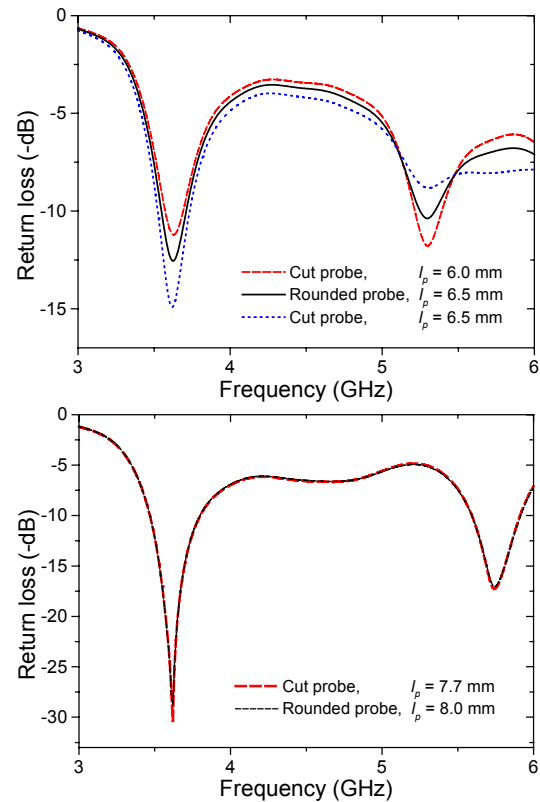


Fig. 8. Return loss for the probe-fed hemispherical resonator for different probe lengths illustrating the reduction of effective length caused by rounding the tip of the probe. Upper graph: The curve for rounded probe with 6.5 mm length is located in between the probes with lengths 6.0 mm and 6.5 mm. Lower graph: Nearly identical curves are obtained when considering a rounded tip 0.3 mm longer (here close to optimal length of the probe).

C. Effect of Air Gap around the Probe

The presence of an air gap around the probe has a more pronounced effect on the matching condition of the device than the rounding of the tip, since it basically alters the boundary condition over the whole surface of the probe. This has been investigated experimentally in [11] showing a significant effect of air gaps around the probe which fed a cylindrical dielectric resonator. Such an air gap might exist because of the mechanical tolerances associated with drilling a hole in the dielectric material to insert the probe.

In the present numerical study, we have used the FVTD method to model air gaps around the probe of the hemispherical DRA. Different thicknesses of air gap between 0.05 mm and 0.3 mm have been modeled and compared to the ideal case of a perfect mechanical contact between the probe and the dielectric (no air gap).

The input impedance of the probe-fed hemispherical DRA (rounded probe with length 8.0 mm) is plotted in Fig. 9 close to the first resonance frequency for different values of the air gap. The presence of the air gap shifts the peak of the input resistance towards higher frequencies and lowers its maximum value. Very thin air gaps can lower significantly the magnitude of the peak input resistance. The largest air gap modeled here (0.3 mm) roughly reduces the maximum input resistance to half (from 59 Ω to 25 Ω) and moves its location from 3.56 GHz to 3.67 GHz. A similar behavior is observed for the higher-order resonances.

Results from a simulation neglecting such air gaps would not yield accurate design parameters. This can be explicitly observed in Fig. 10 where the return loss is represented around the first resonance for several thicknesses of the air gap. A qualitatively similar behavior has been observed experimentally in [11] for a cylindrical DRA.

From the point of view of the computational cost, the resolution of very thin air gaps (e.g. here 0.05 mm) around the

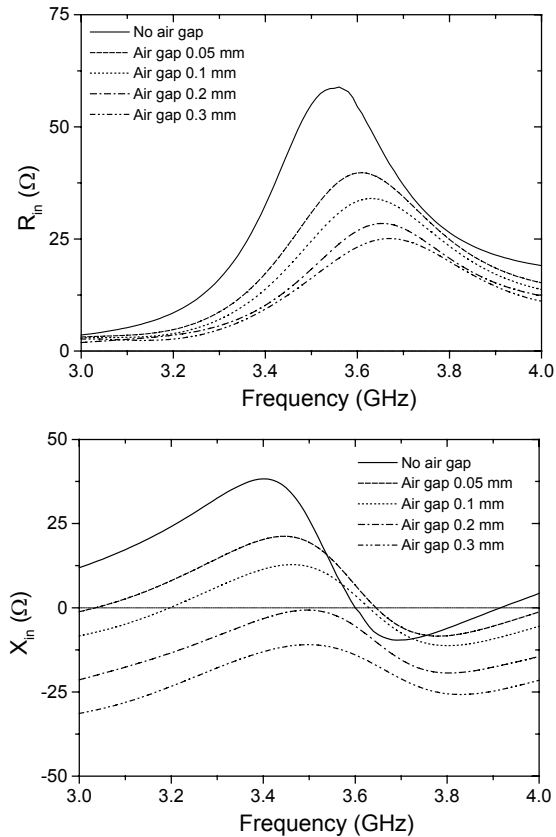


Fig. 9. Effect of an air gap surrounding the probe on the input impedance Z_{in} of the DRA. The rounded probe has a length of 8.0 mm. The R_{in} (upper graph) and X_{in} (lower graph) indicate the real and imaginary part of the input impedance respectively.

probe typically increases the number of cells in the mesh (Table II) and therefore the overall computational effort. Introducing local time-steps dampens this negative effect since the necessary reduction of time steps associated with the small cells affects only a limited region around the feed.

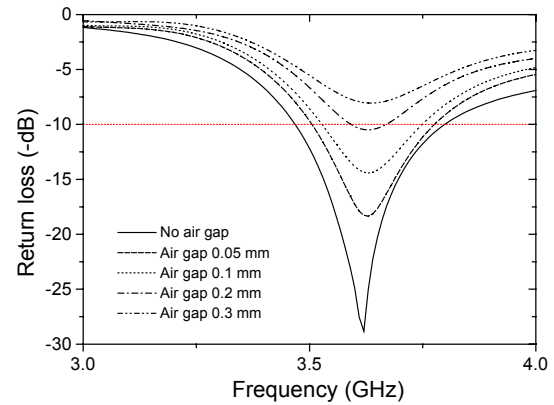


Fig. 10. Return loss of the hemispherical DRA with different thicknesses of air gap around the probe. The figure illustrates the degradation of the matching condition that can occur because of fabrication tolerances.

D. Effect of Air Gap between DRA and Ground Plane

Another fabrication issue likely to affect the radiation characteristics of a DRA has been described in [12]: A thin gap between the dielectric material and the ground plane can affect severely the input impedance of the device. This can be explained by a change in boundary condition at the bottom of the DRA.

The effect of the air gap between the hemispherical DRA and the ground plane on the input impedance is shown in Fig. 11 for different thicknesses of air gap (0.15 mm, 0.30 mm and 0.45 mm). The results are compared to the corresponding device without air gap. It is obvious that the presence of the air gap shifts the resonance frequency and the peak of the input resonance upwards in a significant manner. This can be interpreted as a lowering of the effective dielectric constant of the DRA due to the presence of the air gap.

The shift in resonance frequency shown in Fig. 11 is associated to a decrease of the Q factor of the structure and to an increase of the matching bandwidth of the device. As illustration of this fact, the return loss of the four DRAs is shown in Fig. 12. The relative bandwidth is doubled through the presence of the 0.3 mm air gap between the dielectric resonator and the ground plane. The exploitation of this effect has been suggested in [10] as a practical means to increase bandwidth. The downside of the technique is a required increase in size of the device for a fixed frequency of operation.

From the point of view of the computational effort, it should be mentioned again that resolving very thin gaps increases the overall number of cells in the computational domain. The type of air gap considered here has a more pronounced effect on the computational load since larger regions of the computational domain are affected than in the case of the air gap around the probe.

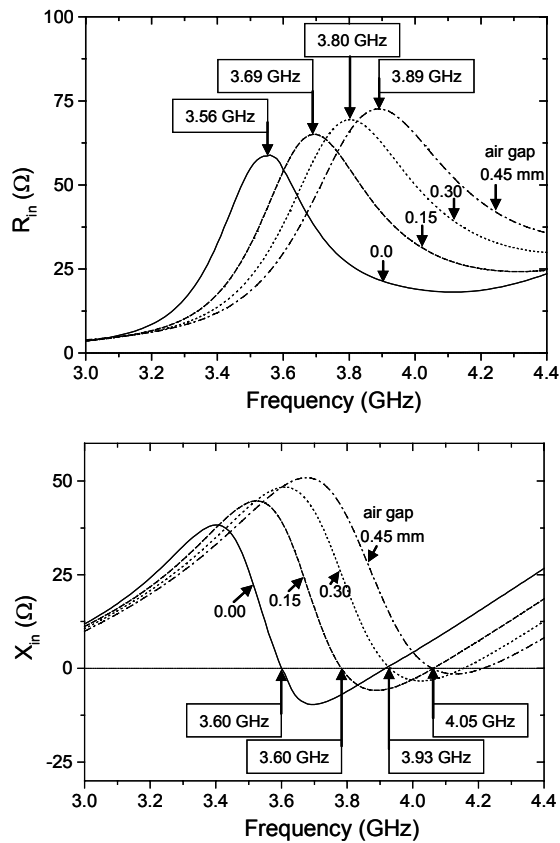


Fig. 11. Effect of an air gap between DRA and ground plane on the input impedance Z_{in} of the DRA. The rounded probe has a length of 8.0 mm. The R_{in} (upper graph) and X_{in} (lower graph) indicate the real and imaginary part of the input impedance respectively.

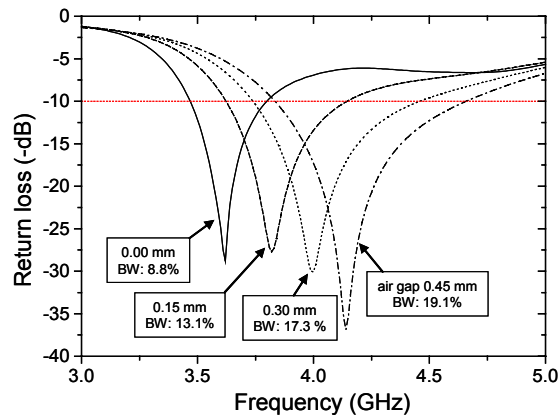


Fig. 12. Return loss of the hemispherical DRA with different air gaps between the dielectric and the ground plane. The figure illustrates the shift of the resonance frequency and the increase of the relative bandwidth when the air gap becomes thicker.

E. Effect of the Feeding on the Radiation Pattern

The radiation pattern is mainly determined by the geometry of the dielectric material and by the arrangement of the ground plane. However, by changing the location of the probe inside the DRA, different modes might be excited in the dielectric, leading to different radiation patterns. In the simulations presented here, the location of the probe has been kept

constant at a distance of 6.5 mm from the center of the hemisphere. This arrangement is chosen for excitation of the TE_{111} mode inside the dielectric.

For all the simulations where only the probe has been modified (as in paragraphs A, B, and C), no relevant variations of the patterns have been observed for any probe length or shape. This confirms that the variations of the probe represent a practical way of matching the antenna to the feed circuit without changing the radiation characteristics.

On the contrary, small differences can be observed if the relative arrangement of the ground plane and the DRA is modified. This is the case for example when the air gap is introduced between dielectric and ground plane (Paragraph D).

In Fig. 13, the computed patterns of the DRA are shown at a frequency of 3.6 GHz (near first resonance) in two principal planes. The curves are represented for three different configurations. The first two models chosen (curves 1 & 2) have different feeds (1 mm cut probe, and 8 mm rounded probe with air gap) and their patterns cannot be distinguished, even though the input impedances of the devices are very different. The third curve shown in the figure represents a DRA that has an additional air gap (0.45 mm thick) between the dielectric and the ground plane. This affects the patterns of the device, although not dramatically.

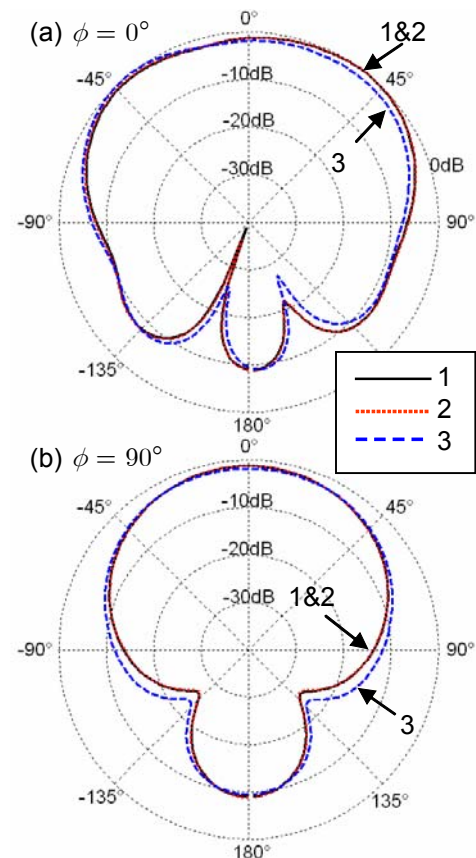


Fig. 13. Radiation patterns of the DRA at 3.6 GHz in two principal planes: (a) plane containing the probe (E-plane), (b) orthogonal plane (H-plane). The patterns are represented for three configurations: (1) 1 mm cut probe, (2) 8 mm rounded probe with 0.3 mm air gap around the probe, (3) 8 mm rounded probe plus air gap between the ground plane and the dielectric.

F. Effect of the Finite Ground Plane

A more visible effect can be observed when the dimensions of the ground plane of the DRA are changed. Different sizes of ground planes on the bottom of the dielectric have been modeled. Results for planar circular ground planes with radii equal to 60 mm and 180 mm have been compared to those with infinite ground plane. Modeling the latter, a perfectly conducting symmetry plane has been used in conjunction with image theory during the near to far field transformation necessary to obtain the radiation patterns.

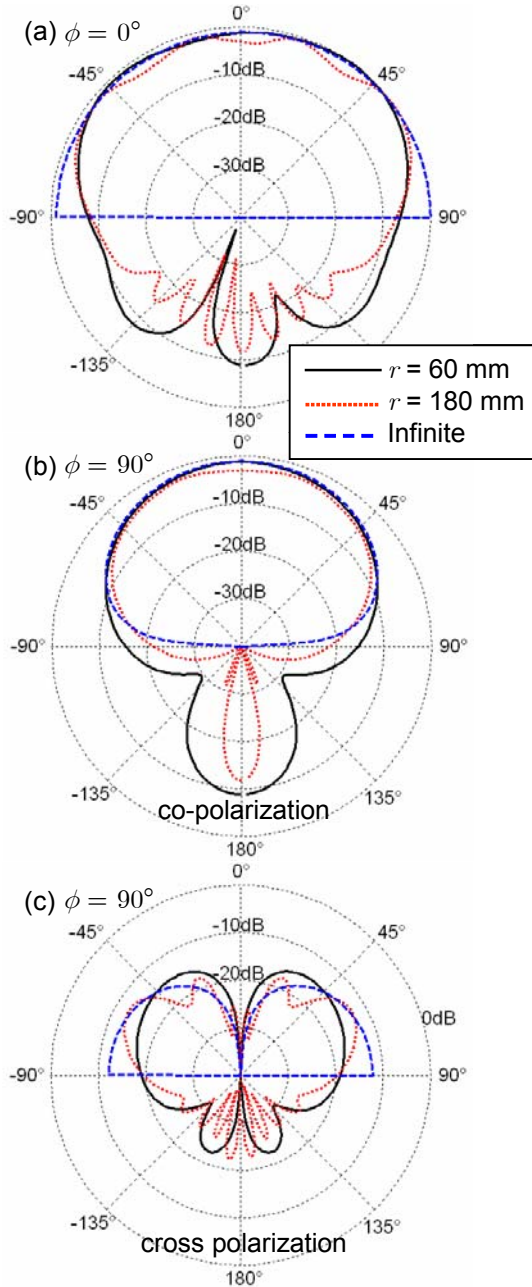


Fig. 14. Radiation patterns near the first resonance (3.6 GHz) for the hemispherical DRA with rounded probe (length 8 mm). The different curves correspond to the given radii r of the circular ground plane. (a) E-plane co-polarized pattern E_θ , (b) H-plane co-polarized pattern E_ϕ , (c) H-plane cross-polarized pattern E_θ . The cross-polarized component in the E-plane is too small to be represented in this scale.

From the point of view of matching the DRA to the feed circuit, the use of different ground planes does not have a noticeable effect. On the other hand, we observe that the radiation patterns are clearly influenced by the extent of the ground plane. The angular patterns in two principal planes are shown in Fig. 14 and Fig. 15 for the cross- and co-polarized components (third Ludwig definition [13]) of the radiated fields at the first two resonances. The cross-polarized component in the E-plane (plane containing the probe) is not shown since it is negligibly small.

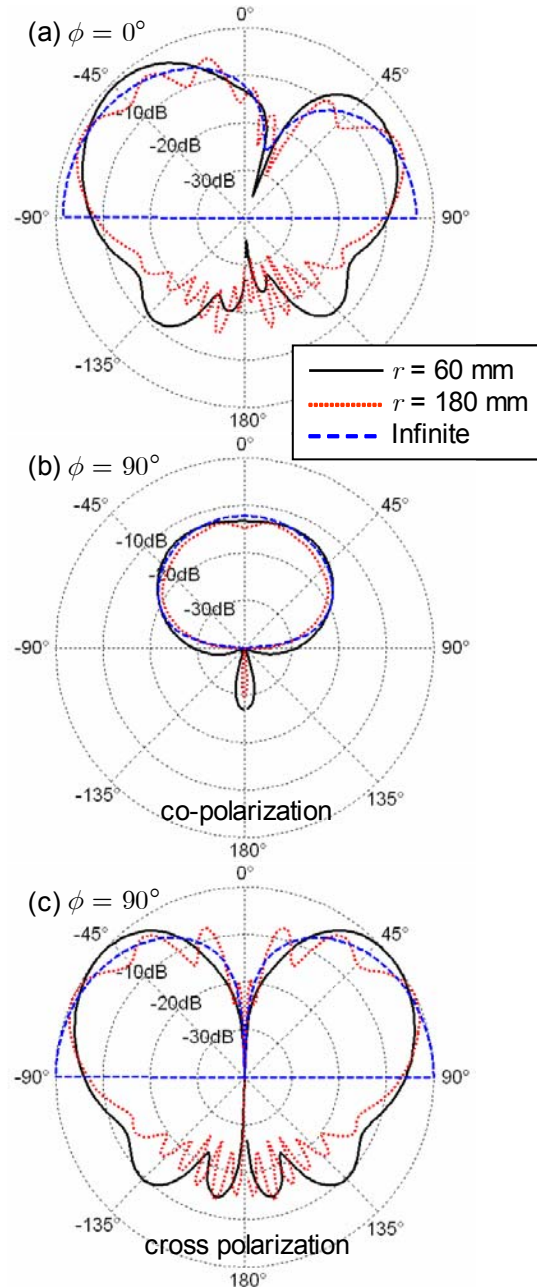


Fig. 15. Radiation patterns near the second resonance (5.3 GHz) for the hemispherical DRA with rounded probe (length 8 mm). The different curves correspond to the given radii r of the circular ground plane. (a) E-plane co-polarized pattern E_θ , (b) H-plane co-polarized pattern E_ϕ , (c) H-plane cross-polarized pattern E_θ . The cross-polarized component in the E-plane is too small to be represented in this scale.

Comparing the radiation patterns at the two frequencies (Fig. 14 vs. Fig. 15), it can be observed that the first resonance radiates towards broadside whereas the second radiates with end-fire characteristics.

The chosen sizes of the ground planes correspond to diameters larger than the free-space wavelength at the first resonance ($1.45 \lambda_0$ and $2.17 \lambda_0$ respectively at 3.6 GHz). We observe small oscillations of the curves (local maxima and minima) as a function of the angle for the finite ground planes. These oscillations are caused by resonances of the ground plane, which is confirmed by the fact that the device with three times larger ground plane have three times faster angular oscillations (see e.g. the back lobes). It is also observed as expected that the back radiation is reduced when the ground plane is extended.

These simulations show qualitatively the errors that arise when using infinite ground-plane computations to model devices with relatively small ground planes.

V. CONCLUSIONS

The FVTD method has been applied to the simulation of a probe-fed hemispherical DRA. Emphasis of the investigation has been placed on the effect of manufacturing issues, such as influence of feeding details on the matching and on the resonance frequency. The probe length provides as expected a convenient way to match the device to the circuit with a negligible influence on the radiation pattern. The shape of the probe tip has been demonstrated to have a sensible effect on the input impedance of the device: A rounded probe appears shorter than a cut probe. A more pronounced effect is introduced by an air gap between the probe and the dielectric material: The input impedance is significantly lowered and the resonance is shifted toward larger frequencies.

The simulations presented here demonstrate the versatility of the FVTD algorithm. Modeling other complex shapes (e.g. [14],[15]) does not change or increase the complexity level of the algorithm. The intrinsic geometrical flexibility of the method permits, when coupled to a local time-stepping scheme, the resolution of small details with excellent accuracy. This makes the FVTD method a very powerful tool that can be applied to assess the effect of fabrication tolerances of complex devices.

ACKNOWLEDGMENT

This work was supported by the Swiss procurement agency (armasuisse), Bern, Switzerland.

REFERENCES

- [1] N. K. Madsen, R. W. Ziolkowski, "A three-dimensional modified finite volume technique for Maxwell's equations", *Electromagnetics*, vol. 10, pp. 147-161, 1990
- [2] V. Shankar, A. H. Mohammadian, W. F. Hall, "A time-domain, finite-volume treatment for the Maxwell equations", *Electromagnetics*, vol. 10, pp. 127-145, 1990
- [3] P. Bonnet, X. Ferrieres, B. L. Michielsen, P. Klotz, J. L. Roumiguieres, "Finite-Volume Time Domain Method", Chapter 9 in *Time domain electromagnetics*, edited by S. M. Rao, Academic Press, San Diego, 1999
- [4] C. Fumeaux, D. Baumann, P. Leuchtman, R. Vahldieck, "A generalized local time-step scheme for efficient FVTD simulations in strongly inhomogeneous meshes", *IEEE Trans. Microwave Theory Tech.* MTT-52(3), pp. 1067-1076, 2004
- [5] D. Baumann, C. Fumeaux, P. Leuchtman, R. Vahldieck, "Generalized-scattering-matrix extraction using the finite-volume time-domain (FVTD) method", *IEEE MTT-S Int. Microwave Symp. Dig.*, pp. 1701-1704, June 2004
- [6] A. Petosa, A. Ittipiboon, Y. M. M. Antar, D. Roscoe, M. Cuhaci, "Recent advances in dielectric-resonator antenna technology", *IEEE Antennas Propagat. Mag.* 40(3), pp. 35-48, 1998
- [7] K. W. Leung, K. M. Luk, K. Y. A. Lai, D. Lin, "Theory and experiment of probe fed dielectric resonator antenna", *IEEE Trans. Antennas Propagat.* AP-41, pp. 1390-1398, 1993
- [8] K. W. Leung, K. K. Tse, K. M. Luk, E. K. N. Yung, "Cross-polarization characteristics of a probe-fed hemispherical dielectric resonator antenna", *IEEE Trans. Antennas Propagat.* AP-47(7), pp. 1228-1230, 1999
- [9] D. Baumann, C. Fumeaux, P. Leuchtman, R. Vahldieck, "Finite-Volume Time-Domain (FVTD) Method and its Application to the Analysis of Hemispherical Dielectric-Resonator Antennas", *IEEE MTT-S Int. Microwave Symp. Dig.*, pp. 985-988, June 2003
- [10] G.P. Junker, A.A. Kishk, A.W. Glisson, D. Kajfez, "Effect of fabrication imperfections for ground-plane-backed dielectric-resonator antennas", *IEEE Antennas Propagat. Mag.* 37(1), pp. 40-47, Feb. 1995
- [11] G. P. Junker, A. A. Kishk, A. W. Glisson, D. Kajfez, "Effect of an air gap around the coaxial probe exciting a cylindrical dielectric resonator antenna", *Electronics Letters* 30(3), pp. 177-178, 1994
- [12] G. P. Junker, A. A. Kishk, A. W. Glisson, D. Kajfez, "Effect of an air gap on a cylindrical dielectric antenna operating in the TM_{01} mode", *Electronics Letters* 30(2), pp. 97-98, 1994
- [13] A. C. Ludwig, "The definition of cross polarization", *IEEE Trans. Antennas Propagat.* AP-21(1), pp. 116-119, 1973
- [14] A. A. Kishk, Y. Yin, A. W. Glisson, "Conical dielectric resonator antennas for wide-band applications", *IEEE Trans. Antennas Propagat.* AP-50(4), pp. 469-474, 2002
- [15] K. W. Leung, "Conformal strip excitation of dielectric resonator antenna", *IEEE Trans. Antennas Propagat.* AP-48(6), pp. 961-967, 2000



Christophe Fumeaux received the diploma and Ph.D. degrees in physics from the Swiss Federal Institute of Technology (ETH) Zurich, Switzerland, in 1992 and 1997, respectively. His Ph.D. thesis on antenna-coupled infrared detectors was awarded the ETH Silver Medal of Excellence. From 1998 to 2000 he was post-doctoral researcher in infrared technology at the School of Optics (CREOL) of the University of Central Florida (UCF), Orlando. In 2000 he joined the Swiss Federal Office of Metrology in Bern, Switzerland, as a scientific staff member. Since 2001, he is a research associate at the Laboratory for Electromagnetic Fields and Microwave Electronics (IFH) at ETH Zurich. His current main research interest concerns computational electromagnetics in the time domain for numerical analysis of microwave circuits and antennas.



Dirk Baumann received the Dipl. Ing. degree in electrical engineering from the University of Karlsruhe, Germany, in 2001. Between Spring and Fall 2000 he did an internship at the Alaska SAR Facility (ASF) in Fairbanks, AK, working on the calibration of ASF's SAR processor. Currently he is working toward the Ph.D. degree in electrical engineering at the Laboratory for Electromagnetic Fields and Microwave Electronics (IFH), ETH Zurich, Switzerland. His research interests

include numerical methods with emphasis on time domain techniques and their application to general electromagnetic problems.



Rüdiger Vahldieck received the Dipl. Ing. and the Dr. Ing. degrees in electrical engineering from the University of Bremen, Germany, in 1980 and 1983, respectively.

From 1984 to 1986 he was a Postdoctoral Fellow at the University of Ottawa, Canada. In 1986 he joined the Department of Electrical and Computer Engineering at the University of Victoria, British Columbia, Canada, where he became a Full Professor in 1991. During Fall and Spring of 1992-'93 he was a visiting scientist at the "Ferdinand-Braun-Institut für Höchstfrequenztechnik" in Berlin, Germany. In 1997 he accepted an appointment as Professor for electromagnetic field theory at the Swiss Federal Institute of Technology, Zurich, Switzerland, and became head of the Laboratory for Electromagnetic Fields and Microwave Electronics (IFH) in 2003. His research interests include computational electromagnetics in the general area of EMC and in particular for computer-aided design of microwave, millimeter wave and opto-electronic integrated circuits.

Professor Vahldieck is a Fellow of the IEEE. He received the J.K. Mitra Award of the IETE (in 1996) for the best research paper in 1995, and was co-recipient of the outstanding publication award of the Institution of Electronic and Radio Engineers in 1983. Since 1981 he has published more than 230 technical papers in books, journals and conferences, mainly in the field of microwave CAD. He is the Past-President of the IEEE 2000 International Zurich Seminar on Broadband Communications (IZS'2000) and since 2003 President and General Chairman of the international Zurich Symposium on Electromagnetic Compatibility. He is a member of the editorial board of the IEEE Transaction on Microwave Theory and Techniques. From 2000 until 2003 he served as an Associate Editor for the IEEE Microwave and Wireless Components Letters and has now become the Editor-in-Chief effective Jan. 2004. Since 1992 he serves on the Technical Program Committee of the IEEE International Microwave Symposium, the MTT-S Technical Committee on Microwave Field Theory, and in 1999 on the TPC of the European Microwave Conference. From 1998 until 2003 Professor Vahldieck was the chapter chairman of the IEEE Swiss Joint Chapter on MTT, AP and EMC.

ANALYSIS OF A SUSPENDED STRIP IN A CIRCULAR CYLINDRICAL WAVEGUIDE

Hassan A. Ragheb

E-mail: hragheb@kfupm.edu.sa

Essam Hassan

E-mail: ehassan@kfupm.edu.sa

Department of Electrical Engineering
King Fahd University of Petroleum and Minerals
Dhahran, Saudi Arabia

Abstract: The separation of variables method along with transformation theorem from Mathieu functions to Bessel functions are employed here to analyze the problem of a suspended strip in a circular waveguide. An infinite dimensional determinant is obtained which represents the characteristic equation of the proposed structure. To obtain the cutoff wavenumbers for both TE and TM cases of such a structure, the infinite determinant is truncated and convergence was observed. Numerical results for cases of interest are then presented.

Introduction

The cut-off frequencies of circular cylindrical waveguides loaded with eccentric inner conductors were extensively investigated. For instance, a general problem of a conducting cylinder placed inside a conducting hollow tube of arbitrary cross section was formulated and solved by the point-matching technique in [1]. Kuttler [2] obtained the lower and upper bounds of the cutoff wavenumbers using different methods. Analytical formulations were also developed and used to calculate exact values of the cutoff wavenumbers in [3-5] employing different methodologies. Recently, Das and Vargheese employed a bilinear transformation to transform the two-wire and the eccentric transmission line into the concentric coaxial configuration [6].

Elliptical waveguides have been the subject of many investigations due to their wide applications in radar feed lines, multichannel communication and accelerator beam tubes. Another line of research [7] investigated elliptical waveguide loaded with ridges or a suspended strip. It was assumed that the ridges extended from the walls to the focal points. Recently Rozzi et al. [8] reported a complete analysis for a suspended strip in an elliptical cylindrical waveguide. They considered the case where the suspended strip extended between the focal points of the elliptical waveguide. He obtained

the cutoff wavelengths for different TEM, TE and TM modes using the separation of variables. An extension to Rozzi's analysis for the more general case of a strip of arbitrary width was reported in [9]. The strip width could be larger or smaller than the focal length of the elliptic cylinder.

The special case of suspended strip in a circular cylindrical waveguide has not been yet addressed. Results for such a special case can not be directly obtained from the general case reported in [9] due to singularity of the Mathieu functions when the outer ellipse of the waveguide has zero focal length. Meanwhile if the focal length is considered very small the resulting cutoff wavenumbers are not close to those of the special case because they are very sensitive to the geometrical dimensions. Accordingly, such a special case has to be treated separately. The problem involves two different coordinate systems, i.e. circular cylindrical (to fit the circular boundary of the outer waveguide) and elliptical coordinates (to fit the elliptical boundary of the strip) which reflects the use of both Bessel and Mathieu functions. This paper addresses such a problem and employs the transformation from Mathieu to Bessel functions [10] to facilitate the application of the boundary conditions. Some special cases are introduced first for comparison with published data to ensure that our program is correct then other new results are introduced.

Theory

Consider the two-dimensional cross-sectional geometry shown in Fig. 1. It consists of an infinitely long perfectly conducting circular waveguide with radius b . A perfectly conducting strip of width $2a$ and infinite length is placed such that its axes coincide with that of the circular waveguide. In order to facilitate our analysis, two coordinate systems are considered. The local elliptical coordinates (u_o, v_o, z) are at the center of the strip while the global circular coordinates

(ρ, ϕ, z) are considered at the center of the circular cylinder. The solution of the scalar Helmholtz wave equation in terms of elliptical coordinates can be written as

$$\psi(\zeta_o, \eta_o) = \sum_{n=0}^{\infty} \{Ae_n Je_n(c_o, \zeta_o) + Be_n Ne_n(c_o, \zeta_o)\} Se_n(c_o, \eta_o) e^{-j\beta z} \quad (1)$$

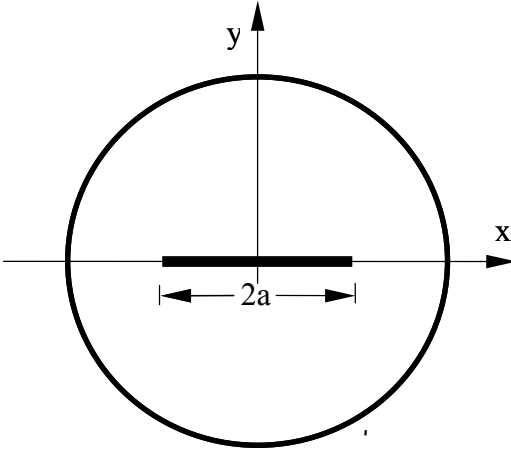


Fig. 1. Geometry of the problem.

for the even modes, and while for the odd modes,

$$\psi(\zeta_o, \eta_o) = \sum_{n=0}^{\infty} \{Ao_n Jo_n(c_o, \zeta_o) + Bo_n No_n(c_o, \zeta_o)\} So_n(c_o, \eta_o) e^{-j\beta z} \quad (2)$$

where $\zeta = \cosh u$, $\eta = \cos v$, $c_o = k_c a$ ($k_c^2 = k^2 - \beta^2$, k_c is the transverse component, while $k = 2\pi/\lambda$ is the free space wavenumber, λ is the wavelength and β is the propagation constant). Je_n and Ne_n are even modified radial Mathieu functions of the first and second kind, respectively, while Jo_n and No_n are their corresponding odd functions. Se_n and So_n are the even and odd angular Mathieu functions. Ae_n , Ao_n , Be_n and Bo_n are coefficients to be calculated by imposing the boundary conditions.

1. TE Case

These modes must satisfy the boundary condition of vanishing tangential components of the electric field ($E_v = 0$) on the perfectly conducting surfaces, i. e:

$$\frac{\partial \psi}{\partial u_o} \Big|_{u_o=0} = 0, \quad 0 \leq v_o \leq 2\pi \quad \text{and}$$

$$\frac{\partial \psi}{\partial \rho} \Big|_{\rho=b} = 0, \quad 0 \leq \phi \leq 2\pi. \quad (3)$$

Since we have even and odd modes in each case, one can consider them individually.

(a) TE Even Modes

Applying the first boundary condition

$$\frac{\partial \psi}{\partial u_o} \Big|_{u_o=0} = 0, \quad 0 \leq v_o \leq 2\pi, \quad \text{one can obtain}$$

$$Be_n = 0, \quad \text{which when substituting in (1) yields}$$

$$\psi(\zeta_o, \eta_o) = \sum_{n=0}^{\infty} Ae_n Je_n(c_o, \zeta_o) Se_n(c_o, \eta_o) e^{-j\beta z}. \quad (4)$$

Now in order to apply the second boundary condition $\psi(\zeta_o, \eta_o)$ must be transferred to the circular cylindrical coordinate system (ρ, ϕ, z) . This can be done using the addition theorem of Mathieu functions [10], which is simplified for this case as

$$\begin{aligned} Re_p^{(j)}(c_o, \zeta_o) Se_n(c_o, \eta_o) &= \sqrt{\frac{\pi}{2}} \sum_{l=0}^{\infty} (j)^{l-p} \\ Ro_p^{(j)}(c_o, \zeta_o) So_n(c_o, \eta_o) &= \sqrt{\frac{\pi}{2}} \sum_{l=0}^{\infty} (j)^{l-p} \\ &\quad \begin{matrix} De_l^p(c_o) & Z_l^{(i)}(k\rho) & \cos(l\alpha) \\ Do_l^p(c_o) & & \sin(l\alpha) \end{matrix} \end{aligned} \quad (5)$$

where $Re_p^{(j)}$ could be Je_n or Ne_n while $Ro_p^{(j)}$ is Jo_p or No_p and $Z_l^{(j)}$ is the Bessel function of the first or second kind, respectively. The constants De_m^n and Do_m^n are coefficients of the infinite series of angular Mathieu functions in terms of trigonometric functions defined in [9]. To apply the second boundary condition, (5) is employed in (4) as

$$\psi(\rho, \phi) = \sqrt{\frac{\pi}{2}} \sum_{n=0}^{\infty} \sum_{l=0}^{\infty} (j)^{l-n} De_l^n(c_o) J_l(k_c \rho) \cos(l\phi) e^{-j\beta z}. \quad (6)$$

Applying the second boundary condition and using the orthogonal property of the trigonometric functions, one obtains

$$\sum_{n=0}^{\infty} Ae_n (j)^{l-n} De_l^n(c_o) J_l'(k_c b) \quad l = 0, 1, 2, \dots \quad (7)$$

Equation (7) can be written in the following matrix form,

$$[Z_{l,n}] [Ae_n] = 0. \quad (8)$$

A non-trivial solution can be obtained if the determinant of the Z matrix vanishes. The solution

of the resulting determinant will give the values of k_c corresponding to the 1st, 2nd, ... and nth cutoff wavenumbers. Once the value of k_c is obtained for the ith cutoff wavenumber, the coefficients can be obtained and the field distribution inside the waveguide is then completely defined.

(b) *TE odd Modes*

Following the same procedure described for the TE even modes but with $\psi(\zeta_o, \eta_o)$ represented in terms of odd functions [equation (2)], one ends up with a matrix equation similar to that in (8), where the elements of the matrix are given by:

$$Z_{l,n} = (j)^{l-n} D o_l^n(c_o) \left\{ J_l'(k_c \rho) - \frac{J o_n'(c_o, 1)}{N o_n'(c_o, 1)} - N_l'(k_c \rho) \right\} \quad l = 1, 2, 3, \dots \quad (9)$$

and the coefficient vector is denoted as $A o_n$. Again the determinant of the matrix is equal to zero to obtain the cutoff wavenumbers.

2. *TM Case*

These modes must satisfy the boundary condition of vanishing tangential components of the electric field ($E_u = 0$) on the perfectly conducting surfaces, i.e.

$$\begin{aligned} \psi|_{u_o=0} &= 0, & 0 \leq v_o \leq 2\pi & \quad \text{and} \\ \psi|_{\rho=b} &= 0, & 0 \leq \phi \leq 2\pi. & \quad (10) \end{aligned}$$

Even and odd modes can be considered individually as follows:

(a) *TM Even Modes*

Applying the first boundary condition along with the orthogonal property of Mathieu functions yields

$$\begin{aligned} \psi(\zeta_o, \eta_o) &= \sum_{n=0}^{\infty} A e_n \left\{ J e_n(c_o, \zeta_o) - \frac{J e_n(c_o, 1)}{N e_n(c_o, 1)} \right. \\ &\quad \left. - N e_n(c_o, \zeta_o) \right\} S e_n(c_o, \eta_o) e^{-j\beta z}. \end{aligned} \quad (11)$$

Employing the addition theorem of the Mathieu functions and applying the second boundary condition along with the orthogonal property of the triangular Mathieu functions, one can get matrix equation similar to (8) with the elements of Z matrix given by

$$Z_{l,n} = (j)^{l-n} D e_l^n(c_o) \left\{ J_l(k_c b) - \frac{J e_n(c_o, 1)}{N e_n(c_o, 1)} - N_l(k_c b) \right\} \quad l = 0, 1, 2, \dots \quad (12)$$

(b) *TM odd Modes*

Following the same procedure described for the TM even modes but with $\psi(\zeta_o, \eta_o)$ represented in terms of odd functions [equation (2)], one ends up with a matrix equation similar to that in (8), where the elements of the matrix are given by:

$$Z_{l,n} = (j)^{l-n} D o_l^n(c_o) J_l(k_c b) \quad l = 1, 2, \dots \quad (13)$$

and the coefficient vector is denoted as $A o_n$.

Results and Discussion

To check the accuracy of our computations the cutoff wavelengths of the special case of circular waveguide is considered by assuming the strip width very small. The results obtained agreed very well with those published in [12].

For the general case, the effect of two parameters a and b (strip width and circular cylinder radius) on the cutoff wavelength was studied. The first cutoff wavenumber versus the strip width for different values of circular guide radius is illustrated in Fig. 2 for both even and odd TM modes. As one can see from Fig. 2(a), the cutoff wavenumber of the even mode increases when the strip width increases. On the other hand, one can see that for the odd TM case, the cutoff wavenumber is constant for all values of the strip width, which shows that the strip has no effect on the cutoff wavenumber for such a mode. This can be explained if one looks at the field distribution of the circular waveguide for the TM_{11} mode [12], where the electric field has no tangential component along one of the circular cylinder diameters at which the strip is going to be placed.

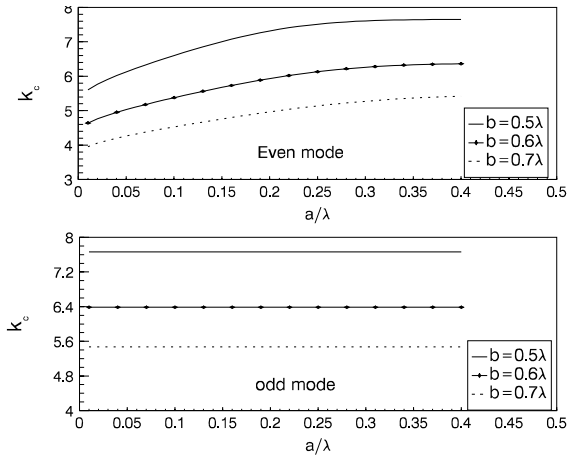


Fig. 2. The first cutoff wavelength versus strip width for even and odd TM modes.

Figure 3 illustrates the effect of the strip width, on the cutoff wavenumber for both even and odd TE modes for different values of circular guide radius. The cutoff wavenumber for the TE case is constant for even modes (Fig. 3(a)) and decreases with the increase of the strip width for odd modes, as shown in Fig. 3(b).

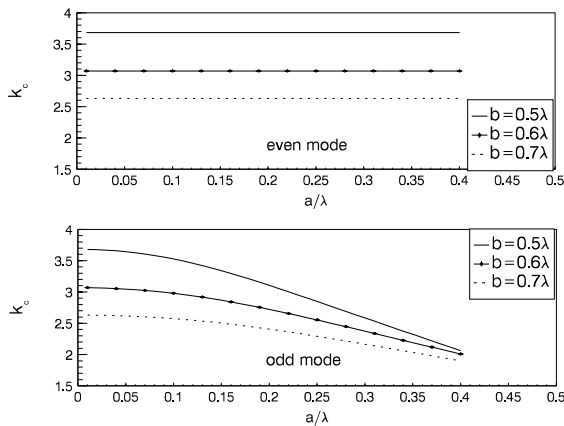


Fig. 3. The first cutoff wavelength versus strip width for even and odd TE modes.

The constant values of the cutoff wavenumbers for the even TE mode can also be realized when one considers the field distribution of such a mode for unloaded circular waveguide. The second cutoff wavenumber was also calculated for both odd and even TE and TM modes as illustrated in Fig. 4 and Fig. 5, respectively. Similar behavior for both TE and TM modes were found except that the rate of increase or decrease of the cutoff wavenumber with the strip width is lower than that corresponding to the first cutoff wavenumber.

Conclusion

The cutoff wavenumbers for both TE and TM cases of an arbitrary strip width suspended in a circular cylindrical waveguide have been calculated. It is found that the cutoff wavenumber increases with the strip width for even TM modes and decreases for odd TE modes.

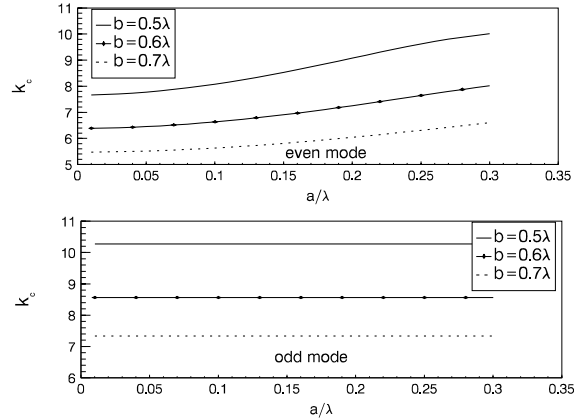


Fig. 4. The second cutoff wavelength versus strip width for even and odd TM modes.

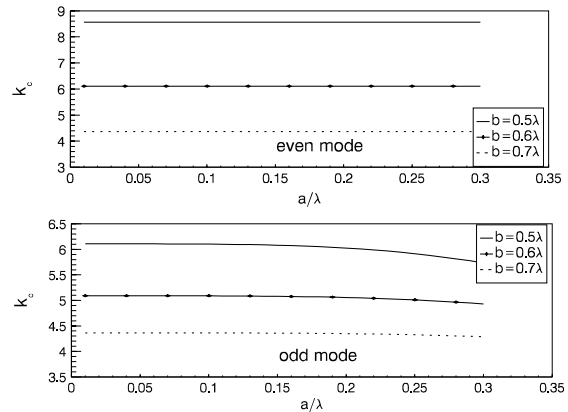


Fig. 5. The second cutoff wavelength versus strip width for even and odd TE modes.

Acknowledgement

The author wishes to thank King Fahd University of Petroleum and Minerals for providing the facilities required to perform this research.

Reference

[1] H. Y. Yee and N. F. Audeh, "Cutoff frequencies of eccentric waveguides", IEEE Trans. on Microwave Theory and Techniques, MTT-14, pp. 487-493, 1966.
 [2] J. R. Kuttler, "A new method for calculating TE and TM cutoff frequencies of uniform waveguide with lunar or eccentric cross

- section”, IEEE Trans. On Microwave Theory and Techniques, MTT-32, pp. 348-354, 1984.
- [3] A. Vishen, G. P. Srivastava and G. S. Singh, “Calculation of cutoff wavenumbers for TE and TM modes in tubular lines with offset center conductor”, IEEE Trans. On Microwave Theory and Techniques, MTT-34, pp. 292-294, 1986.
- [4] L. Zhang, J. Zhang and W. Wang, “Correct determination of TE and TM cutoff wavenumbers in transmission lines with circular outer conductors and eccentric circular inner conductor”, IEEE Trans. On Microwave Theory and Techniques, MTT-39, pp. 1416-1420, 1991.
- [5] G. I. Veselov and S. G. Semenov, “Theory of circular waveguide with eccentrically placed metallic conductor”, Radio Eng., Electron Phys., vol. 15, pp. 687-690, 1970.
- [6] B. N. Das and O. J. Vargheese, “Analysis of dominant and higher order modes for transmission lines using parallel cylinders”, IEEE Trans. On Microwave Theory and Techniques, MTT-42, pp. 681-683, 1994.
- [7] A. El-Sherbiny, “Cutoff Wavelengths of Ridged, Circular, and Elliptic Guides”, IEEE Trans. on Microwave Theory and Techniques, Vol. MTT-21, pp.7-12, 1973.
- [8] T. Rozzi, L. Luca and M. Ronzitti, “Analyses of the Suspended Strip in Elliptical Cross Section by Separation of Variables”, IEEE Trans. on Microwave Theory and Techniques, Vol. MTT-45, pp.1778-1784, 1997.
- [9] H. A. Ragheb, ”Analysis of a Nonconfocal Suspended Strip in an Elliptical Cylindrical Waveguide”, IEEE Trans. on Microwave Theory and Techniques, Vol. MTT-48, pp. 1148-1151, July 2000.
- [10] K. Saermark, “A note on addition theorems for Mathieu functions”, Z. Math. Phys., vol. 10, pp. 426-428, 1958.
- [11] P. M. Morse and H. Feshbach, “Methods of Theoretical Physics”, McGraw-Hill Book Company, Inc., 1953.
- [12] S. Y. Liao, “Microwave Devices and Circuits”, Prentice Hall, 1990.



Hassan Ragheb was born in Port-Said, Egypt, in 1953. He received the B. Sc. Degree in Electrical Engineering from Cairo University, Egypt, in 1977 and the M. Sc. and Ph. D. degrees in Electrical Engineering from the University of Manitoba, Winnipeg, Canada, in 1984 and 1987, respectively. From 1987 to 1989, he was a research assistant in the

Department of Electrical Engineering, University of Manitoba. In 1989, he joined the Department of Electrical Engineering at the King Fahd University of Petroleum and Minerals, where he is now as associate Professor of Electrical Engineering. His research interests include electromagnetic scattering by multiple and coated objects, microstrip antennas, phased arrays, slot and open-ended waveguide antennas.



Essam Hassan was born in Alexandria, Egypt 1947. He obtained his B. S. degree in electrical engineering, (highest honors) from Alexandria Univ. in 1970, and M. S. and Ph. D. from the University of Manitoba, Canada in 1974, 1978 respectively. After graduation, Dr. Hassan worked at Nortel (then Northern Telecom) from 1977 to 1979 as a senior R&D engineer in the digital switching division (DSD). He then joined KFUPM at Dhahran, Saudi Arabia in 1979 where he is currently a Professor of electrical engineering. Dr. Hassan is an author and coauthor of over 30 papers in various disciplines of electrical engineering. He was a visiting Professor at Concordia University, Canada and has served as a consultant in several electrical engineering projects.

RCS of Two Lossy Dielectric Loaded Semi-Elliptic Channels in a Conducting Plane

A-K. Hamid

Department of Electrical and Computer Eng.

University of Sharjah

P.O. Box 27272, Sharjah, U.A.E

email: akhamid@Sharjah.ac.ae

Abstract

Analytical solution to the problem of scattering of a plane electromagnetic wave by two lossy dielectric loaded semi-elliptic channels in a conducting plane is investigated using an iterative procedure to account for the interaction fields between the channels. The incident, scattered and transmitted fields in every region are expressed in terms of complex Mathieu functions. The translation addition theorem is used to compute the higher order scattered fields. Numerical results are presented for the far scattered field for different axial ratios, electrical separation distances, angles of incidence and loss of dielectric materials.

1. Introduction

The electromagnetic scattering from grooves, channels and cracks has many practical applications. The solution may be used to study the scattering by rough surfaces, nondestructive testing of materials, and to check the numerical accuracy of approximate and numerical methods of similar geometries.

Lately, there have been many analytical studies available in the literature on the scattering by hollow and dielectric loaded semi-circular channels [1-5]. Most of these studies are based on the exact dual-series eigenfunction solution. On the other hand, some numerical solutions based on the coupled integral equations for the induced currents were obtained by Senior et. al. [6-7].

Up to date, the analytical solutions available in the literature are for the case of scattering by single semi-elliptic channels loaded by a lossy or lossless dielectric material in a conducting ground plane [8-10]. In this paper, we extend the solution of scattering by a single lossy dielectric loaded semi-elliptic channel in a ground plane to the case of scattering by two adjacent lossy dielectric loaded semi-elliptic channels in a conducting ground plane.

2. Formulation of the scattering problem

Consider the case of a linearly polarized electromagnetic TM plane wave incident on a two lossy dielectric loaded semi-elliptic channels in a conducting ground plane at an angle ϕ_i with respect to the x axis, as shown in Figure 1. The major axes of the channels are denoted by a_1 and a_2 while the minor axes are denoted by b_1 and b_2 . The ground plane is assumed to be perfectly conducting. The time dependence $e^{j\omega t}$ is assumed and omitted throughout. The electric field component of the TM polarized plane wave of amplitude E_0 is given by

$$E_z^i = E_0 e^{jk\rho \cos(\phi - \phi_i)} \quad (1)$$

where k is the wave number in free space. The incident electric field may be expressed in terms of Mathieu functions around the origins o_1 and o_2 as follows

$$E_{1z}^i = \sum_{m=0}^{\infty} A_{1em} R_{em}^{(1)}(c_1, \xi_1) S_{em}(c_1, \eta_1) + \sum_{m=1}^{\infty} A_{1om} R_{om}^{(1)}(c_1, \xi_1) S_{om}(c_1, \eta_1) \quad (2)$$

$$E_{2z}^i = \sum_{m=0}^{\infty} A_{2em} R_{em}^{(1)}(c_2, \xi_2) S_{em}(c_2, \eta_2) + \sum_{m=1}^{\infty} A_{2om} R_{om}^{(1)}(c_2, \xi_2) S_{om}(c_2, \eta_2) \quad (3)$$

where η_1 and η_2 are the intrinsic impedance of ellipse 1 and 2, respectively, and

$$A_{om}^{1em} = E_0 j^m \frac{\sqrt{8\pi}}{N_{om}^{em}(c_1)} S_{om}^{em}(c_1, \cos \phi_i) \quad (4)$$

$$A_{om}^{2em} = E_0 j^m \frac{\sqrt{8\pi}}{N_{om}^{em}(c_2)} S_{om}^{em}(c_2, \cos \phi_i) e^{-jkd \cos(\phi_i)} \quad (5)$$

$$N_{em}(c_1) = \int_0^{2\pi} \int_{om} [S_{em}(c_1, \eta_1)]^2 dv \quad (6)$$

$$N_{em}(c_2) = \int_0^{2\pi} \int_{om} [S_{em}(c_2, \eta_2)]^2 dv \quad (7)$$

and $c_1 = k F_1$, $c_2 = k F_2$, F_1 and F_2 are the semi-focal length of channels one and two, S_{em} and S_{om} are the even and odd angular Mathieu functions of order m , respectively, $R_{em}^{(1)}$ and $R_{om}^{(1)}$ are the even and odd radial Mathieu functions of the first kind, N_{em} and N_{om} are the even and odd normalized functions [11], and d is the separation distance between the centers of the two channels. The scattered electric fields outside the two semi-elliptic channels are decomposed to two parts: reflected and diffracted fields. These fields should only be written in terms of odd Mathieu functions since the incident and scattered fields should vanish at the conducting plane, i.e. at $\eta = 0$ and $\eta = \pi$. This leads to

$$E_{1z}^{ref} = - \sum_{m=1}^{\infty} A_{1om} R_{om}^{(1)}(c_1, \xi_1) S_{om}(c_1, \eta_1), \text{ with} \\ \phi_{i=2\pi-\phi_i} \text{ in equations (4)} \quad (8)$$

$$E_{2z}^{ref} = - \sum_{m=1}^{\infty} A_{2om} R_{om}^{(1)}(c_2, \xi_2) S_{om}(c_2, \eta_2), \text{ with} \\ \phi_{i=2\pi-\phi_i} \text{ in equation (5)} \quad (9)$$

$$E_{1z}^{diff} = \sum_{m=1}^{\infty} B_{1om} R_{om}^{(4)}(c_1, \xi_1) S_{om}(c_1, \eta_1) \quad (10)$$

$$E_{2z}^{diff} = \sum_{m=1}^{\infty} B_{2om} R_{om}^{(4)}(c_2, \xi_2) S_{om}(c_2, \eta_2) \quad (11)$$

where B_{1om} and B_{2om} are the unknown odd scattered field expansion coefficients and $R_{om}^{(4)}$ is the odd radial Mathieu function of the fourth kind. The transmitted electric fields inside the two semi-elliptic channels can also be written in terms of Mathieu functions as

$$E_{1z}^t = \sum_{m=0}^{\infty} C_{1em} R_{em}^{(1)}(c_{11}, \xi_1) S_{em}(c_{11}, \eta_1) \\ + \sum_{m=1}^{\infty} C_{1om} R_{om}^{(1)}(c_{11}, \xi_1) S_{om}(c_{11}, \eta_1) \quad (12)$$

$$E_{2z}^t = \sum_{m=0}^{\infty} C_{2em} R_{em}^{(1)}(c_{22}, \xi_2) S_{em}(c_{22}, \eta_2) \\ + \sum_{m=1}^{\infty} C_{2om} R_{om}^{(1)}(c_{22}, \xi_2) S_{om}(c_{22}, \eta_2) \quad (13)$$

where $c_{11} = k_1 F_1$, $c_{22} = k_2 F_2$, $k_1 = \omega \sqrt{\mu_1 \epsilon_1}$, $k_2 = \omega \sqrt{\mu_2 \epsilon_2}$, $\epsilon_1 = \epsilon_1' - j\epsilon_1''$, $\epsilon_2 = \epsilon_2' - j\epsilon_2''$ while C_{1em} , C_{2em} and C_{1om} , C_{2om} are the even and odd unknown transmitted field expansion coefficients. The magnetic fields inside and outside the two loaded semi-elliptic channels can be obtained using Maxwell's equations.

3. First order scattered fields

The first order scattered fields result from the separate excitation of each semi-channel by the incident plane wave alone. The first order field expansion coefficients can be determined using the boundary conditions which require the total tangential electric field component inside the channels to vanish at the conducting parts, i.e. at $\xi = \xi_1$, $\xi = \xi_2$ and $\pi < \eta < 2\pi$, while the total tangential electric and magnetic field components to be continuous across the imaginary apertures at $\xi = \xi_1$, $\xi = \xi_2$ and $0 < \eta < \pi$. Using the partial orthogonality properties of the angular Mathieu functions, the first order odd scattered and even transmitted field coefficients can be written in matrix form as follows [10]

$$\begin{bmatrix} Q_1 & Q_2 \\ Q_3 & Q_4 \end{bmatrix} \begin{bmatrix} C_{1e}^1 \\ B_{1o}^1 \end{bmatrix} = \begin{bmatrix} V_1 \\ V_2 \end{bmatrix} \quad (14)$$

$$\begin{bmatrix} Q_5 & Q_6 \\ Q_7 & Q_8 \end{bmatrix} \begin{bmatrix} C_{2e}^1 \\ B_{2o}^1 \end{bmatrix} = \begin{bmatrix} V_3 \\ V_4 \end{bmatrix} \quad (15)$$

where

$$Q_1 = R_{em}^{(1)}(c_{11}, \xi_1) L_{1mn} - R_{em}^{(1)'}(c_{11}, \xi_1) \Delta_{1n} F_{1mn} \quad (16)$$

$$Q_2 = R_{om}^{(4)'}(c_1, \xi_1) M_{1mn} \Delta_{1n} \quad (17)$$

$$Q_3 = \left\{ R_{em}^{(1)}(c_{11}, \xi_1) - R_{em}^{(1)'}(c_{11}, \xi_1) \Delta_{1n} \right\} F_{1mn} \quad (18)$$

$$Q_4 = - \left\{ R_{om}^{(4)}(c_1, \xi_1) - R_{om}^{(4)'}(c_1, \xi_1) \Delta_{1n} \right\} M_{1mn} \quad (19)$$

$$V_1 = - \sum_{m=1}^{\infty} 2A_{1om} R_{om}^{(1)'}(c_1, \xi_1) M_{1mn} \Delta_{1n} \quad (20)$$

$$V_2 = \sum_{m=1}^{\infty} 2 \left\{ R_{om}^{(1)}(c_1, \xi_1) - R_{om}^{(1)'}(c_1, \xi_1) \Delta_{1n} \right\} A_{1om} M_{1mn} \quad (21)$$

$$M_{1mn} = \int_0^{\pi} S_{om}(c_{11}, \eta_1) S_{on}(c_1, \eta_1) dv \quad (22)$$

$$F_{1mn} = \int_0^{\pi} S_{em}(c_{11}, \eta_1) S_{on}(c_{11}, \eta_1) dv \quad (23)$$

$$L_{1mn} = \int_{-\pi}^{\pi} S_{em}(c_{11}, \eta) S_{on}(c_{11}, \eta) dv = -F_{1mn} \quad (24)$$

$$\Delta_{1n} = \frac{R_{on}^{(1)}(c_{11}, \xi_1)}{R_{on}^{(1)'}(c_{11}, \xi_1)} \quad (25)$$

and B_{1o}^1 , B_{2o}^1 , and C_{1e}^1 , C_{2e}^1 are the first order odd scattered and even transmitted field vector matrices. Matrices Q_5 , Q_6 , Q_7 , Q_8 , V_3 and V_4 correspond to the second semi-elliptic channel can be written similarly. Equations (14) and (15) may be solved by matrix inversion to obtain the first order scattered field coefficients for given electrical size of semi-elliptic channels, electrical separation, angle of incidence, and lossy dielectric material.

4. Higher order scattered fields

The second order scattered field results from the excitation of each semi-elliptic channel by the scattered field from the other semi-elliptic channel due to the initial incident field. To enforce the boundary conditions, the first order scattered field from the second semi-elliptic channel must be expressed in terms of the coordinate system of the first semi-elliptic channel and vice versa using the addition theorem of Mathieu functions [12], i.e.,

$$R_{om}^{(4)}(c_2, \xi_2) S_{om}(c_2, \eta_2) = \sum_{l=1}^{\infty} WO_{olm}^{2 \rightarrow 1} R_{ol}^{(1)}(c_1, \xi_1) S_{ol}(c_1, \eta_1) \quad (26)$$

where $WO_{olm}^{2 \rightarrow 1}$ is given by [12]. Again, the boundary conditions require the tangential electric field component inside the channels to vanish at $\xi = \xi_1$, $\xi = \xi_2$ and $\pi < \eta < 2\pi$, while the total tangential electric and magnetic fields components to be continuous across the imaginary apertures at $\xi = \xi_1$, $\xi = \xi_2$ and $0 < \eta < \pi$. Using the partial orthogonality properties of the angular Mathieu functions along with equation (26), we obtain the second order scattered field coefficients for semi-elliptic channel one in matrix form as

$$\begin{bmatrix} P_1 & P_2 \\ P_3 & P_4 \end{bmatrix} \begin{bmatrix} C_{1e}^2 \\ B_{1o}^2 \end{bmatrix} = \begin{bmatrix} G_1 & 0 \\ 0 & G_2 \end{bmatrix} \begin{bmatrix} B_{2o}^1 \\ B_{2o}^1 \end{bmatrix} \quad (27)$$

where

$$P_1 = -2 R_{em}^{(1)}(c_{11}, \xi_1) F_{1mn} \quad (28)$$

$$P_2 = R_{om}^{(4)}(c_1, \xi_1) M_{1mn} \quad (29)$$

$$P_3 = -2 \left[R_{em}^{(1)'}(c_{11}, \xi_1) + R_{em}^{(1)}(c_{11}, \xi_1) (1/\Delta_n) \right] F_{1mn} \quad (30)$$

$$P_4 = R_{om}^{(4)'}(c_1, \xi_1) M_{1mn} \quad (31)$$

$$G_1 = - \sum_{l=1}^{\infty} R_{ol}^{(1)}(c_1, \xi_1) WO_{olm}^{2 \rightarrow 1} M_{1ln} \quad (32)$$

$$G_2 = - \sum_{l=1}^{\infty} R_{ol}^{(1)'}(c_1, \xi_1) WO_{olm}^{2 \rightarrow 1} M_{1ln} \quad (33)$$

$$B_{2o}^1 = \begin{bmatrix} B_{2om}^1 \end{bmatrix} \quad (34)$$

and B_{1o}^2 and C_{1e}^2 are the second order scattered and transmitted field vector matrices for channel one. The vector field matrices C_{2e}^2 , B_{2o}^2 that correspond to the second channel can be obtained similarly.

To obtain a general solution, we solve similarly for the higher order scattered fields, which are sensitive to the electrical sizes and separation distances, angles of incidence and dielectric materials. The general expression for the k^{th} order scattered field coefficients of channel one may be written as

$$\begin{bmatrix} P_1 & P_2 \\ P_3 & P_4 \end{bmatrix} \begin{bmatrix} C_{1e}^k \\ B_{1o}^k \end{bmatrix} = \begin{bmatrix} G_1 & 0 \\ 0 & G_2 \end{bmatrix} \begin{bmatrix} B_{2o}^{k-1} \\ B_{2o}^{k-1} \end{bmatrix}. \quad (35)$$

It should be noted that the matrices in equation (35) are computed once (i.e., $k=2$) for the electrical size, dielectric material, and electrical separation considered and used for the subsequent iterations (i.e., $k=3,4,\dots$).

Once the scattered field coefficients are determined, the total far field from the two semi-elliptic channels due to the k^{th} order scattered fields can be determined.

5. Numerical Results

The scattered near and far fields can be calculated once the scattered field expansion coefficients are computed. The scattered far field expression may be written as follows

$$E_z^S = \left(\frac{j}{k\rho} \right)^{0.5} e^{-jk\rho} P(\phi) \quad (36)$$

where

$$P(\phi) = \sum_{k=1,2,\dots} \left\{ \sum_{m=1}^{\infty} j^m B_{1om}^k S_{om}(c_1, \cos \phi) + e^{-jkd \cos(\phi)} \sum_{m=1}^{\infty} j^m B_{2om}^k S_{om}(c_2, \cos \phi) \right\}. \quad (37)$$

In order to solve for the unknown scattered field coefficients, the infinite series are first truncated to include only the first N terms, where N in general is a suitable truncation number proportional to the channel electrical sizes, separation distances and the dielectric loading materials. In the computation, the value of N has been chosen to impose a convergence condition that provides solution accuracy with at least four significant figures [14]. It is found that increasing the electrical sizes of the channel will increase the total truncation number of N terms. Also, to set a criterion for terminating the iteration process, the scattered field after each iteration is calculated and divided by the total field scattered from the pervious iterations, and the process is terminated when the ratio is smaller than 10^{-4} .

The accuracy of the numerical results is checked against the special case of two semi-circular channels loaded with a lossless dielectric material [13]. Fig. 2 shows the normalized backscattered field versus the electrical size $ka_{1,2}$ for two identical loaded semi-circular channels with an incident angle $\phi_i = 90^\circ$, axial ratio $a_{1,2}/b_{1,2}=1.0$ and $d=8.0 a_{1,2}$. The electrical sizes are taken from 0.5 to 5.0. The solid line represents the solution of [13], which is in excellent agreement with our calculation represented by circles. Also, the dashed line represents the lossy dielectric circular channels from which we can see that the resonances start to disappear [14]. Figure 3 is similar to Fig. 2 except for semi-elliptic channels with axial ratio $a_{1,2}/b_{1,2}=2.0$. It can be seen that the location of the resonances has been changed when it is compared with the circular channels. It is worth mentioning that the numerical results given by [13] were only for loaded channels and no hollow cases. Figure 4 is similar to Fig. 3 except for the incident angle changed to 45 degrees. It can be seen that the number of resonances is increased significantly when the incident angle is changed from 90 to 45 degrees.

Fig. 5 shows the normalized backscattered field versus the electrical separation distance kd for two dielectric loaded

identical semi-elliptic channels with $ka_{1,2}=2.0$, $a_{1,2}/b_{1,2}=1.5$ and $\phi_i = 60^\circ$. The electrical separation is taken from 5.0 to 16.5. Fig. 6 shows the echo pattern width versus the scattering angle ϕ for two dielectric loaded identical

channels with $ka_{1,2}=1.5$, $a_{1,2}/b_{1,2}=2.0$, $kd=5.0$ and $\phi_i = 90^\circ$.

Fig. 7 is similar to 6 except for $\phi_i = 60^\circ$. Figure 8 shows the normalized backscattered field versus the incident angle ϕ_i for two dielectric loaded two channels with $ka_{1,2}=2.0$, $a_{1,2}/b_{1,2}=1.5$ and $kd=5.0$.

6. Conclusions

Analytical solution and numerical results of the electromagnetic scattering by a two lossy dielectric loaded semi-elliptic channels in a ground plane is obtained for the case of TM (transverse magnetic) polarization. The validity and accuracy of the obtained numerical results were verified against the special case of two lossless semicircular channels. It is worth mentioning that the number of higher order scattered fields used in the computation of numerical results was ranged from $k=2$ to 4. The agreement was excellent in all cases. It was shown that the presence of lossy and lossless dielectric materials in the channels has significantly changed the scattered field patterns when it was compared with the hollow case. The present work will be extended to the case of an infinite array of semi-elliptic channels in a ground plane since this would be useful for the study of scattering by rough surface.

ACKNOWLEDGEMENT

The author wishes to acknowledge the support provided by the University of Sharjah, U.A.E.

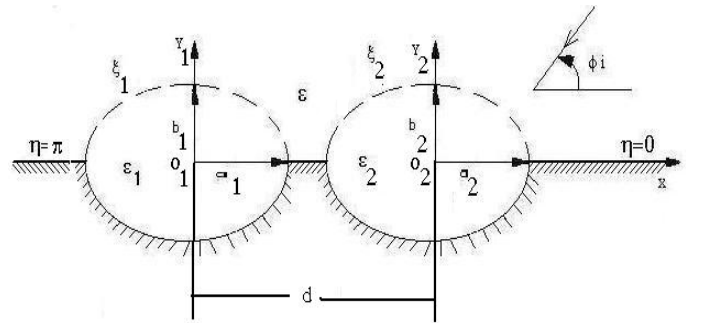


Figure 1. Scattering geometry of two lossy dielectric loaded semi-elliptic channels in a ground plane.

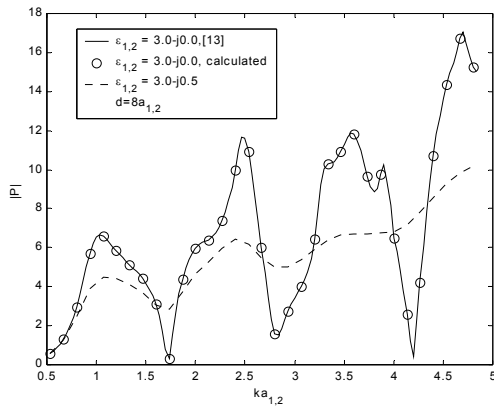


Figure 2. Backscattered field versus electrical size $ka_{1,2}$ for two dielectric loaded identical semi-circular channels with $a_{1,2}/b_{1,2}=1.0$ and $\phi_i = 90^\circ$.

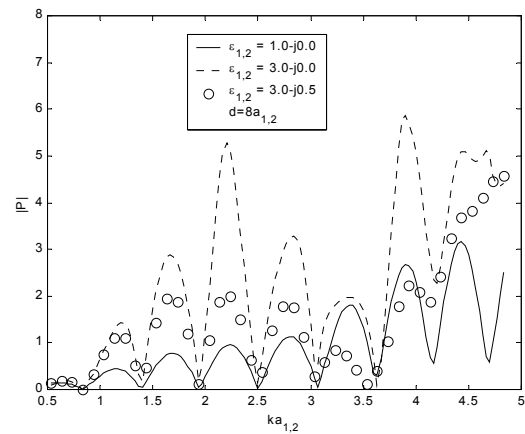


Figure 4. Backscattered field versus electrical size $ka_{1,2}$ for two dielectric loaded identical semi-elliptic channels with $a_{1,2}/b_{1,2}=2.0$ and $\phi_i = 45^\circ$.

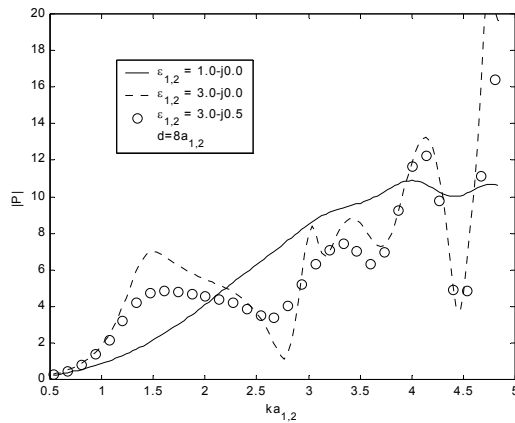


Figure 3. Backscattered field versus electrical size $ka_{1,2}$ for two dielectric loaded identical semi-elliptic channels with $a_{1,2}/b_{1,2}=2.0$ and $\phi_i = 90^\circ$.

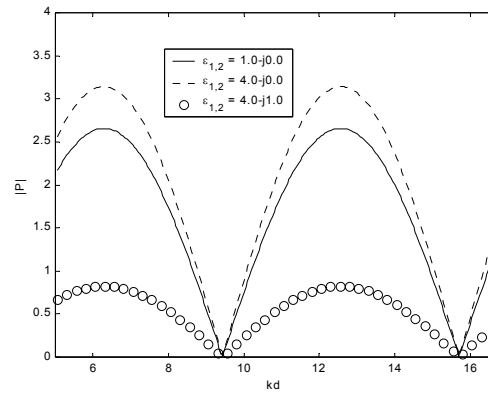


Figure 5. Backscattered field versus electrical separation distance kd for two dielectric loaded identical semi-elliptic channels with $ka_{1,2}=2.0$, $a_{1,2}/b_{1,2}=1.5$ and $\phi_i = 60^\circ$.

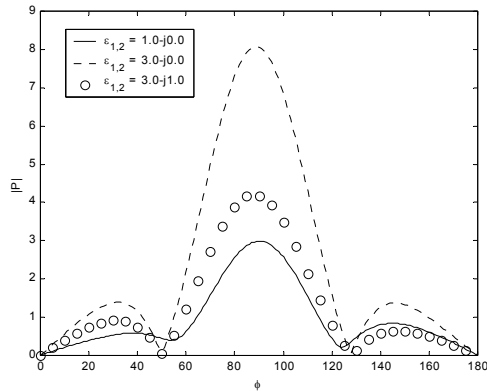


Figure 6. Echo pattern width versus the scattering angle ϕ for two dielectric loaded identical semi-elliptic channels with $ka_{1,2}=1.5$, $a_{1,2}/b_{1,2}=2.0$, $kd=5.0$ and $\phi_i = 90^\circ$.

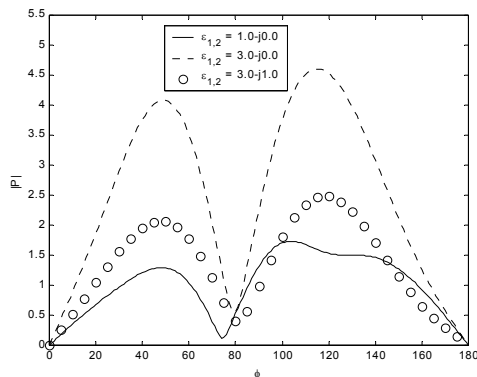


Figure 7. Echo pattern width versus the scattering angle ϕ for two dielectric loaded identical semi-elliptic channels with $ka_{1,2}=1.5$, $a_{1,2}/b_{1,2}=2.0$, $kd=5.0$ and $\phi_i = 60^\circ$.

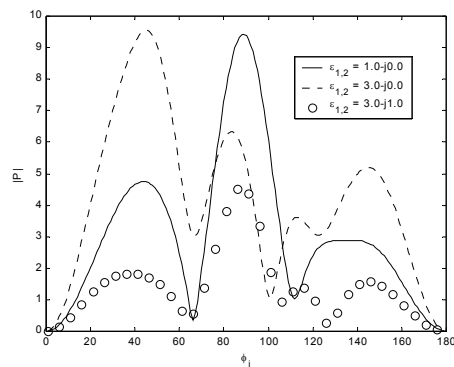


Figure 8. Backscattered field versus the incident angle ϕ_i for two dielectric loaded identical semi-elliptic channels with $ka_{1,2}=2.0$, $a_{1,2}/b_{1,2}=1.5$.

References

1. B. K. Sachdeva, and R. A. Hurd, "Scattering by a dielectric-loaded trough in a conducting plane," *J. Appl. Phys.*, vol. 48, no.4, pp. 1473-1476, 1977.
2. M. K. Hinders, and A. D. Yaghjian, "Dual-series solution to scattering from a semicircular channel in a ground plane," *IEEE Microwave Guided Wave Lett.*, vol. 1, no. 9, pp. 239-242, 1991.
3. T. J. Park, H. J. Eom, W.-M. Boerner, and Y. Yamaguchi, "TE-plane wave scattering from a dielectric-loaded semi-circular trough in a conducting plane," *J. Electromagnetic Waves Applicat.*, vol. 7, pp. 235-245, 1993.
4. H. A. Ragheb, "Electromagnetic scattering from a coaxial dielectric circular cylinder loading a semi channel gap in a ground plane," *IEEE Trans. Microwave Theory Tech.*, vol. 43, no. 6, pp. 1303-1309, 1995.
5. T. Shen, D. Dou, and Z. Sun, "Gaussian beam scattering from a semicircular channel in a conducting plane," *J. Electromagnetic Waves Applicat.*, vol. 16, pp. 67-85, 1997.
6. T. B. Senior and J. L. Volakis, "Scattering by gaps and cracks," *IEEE Trans. Antennas Propag.* Vol. 37, pp. 744-750, 1989.
7. T. B. Senior, K. Sarabandi, and J. Natzke, "Scattering by narrow gap," *IEEE Trans. Antennas Propag.* Vol. 38, pp. 1102-1110, 1990.
8. W. J. Byun, J. W. Yu, and N. H. Myung, "TM scattering from hollow and dielectric-filled semi elliptic channel with arbitrary eccentricity in a perfectly conducting plane," *IEEE Trans. Microwave Theory Tech.*, vol. 46, no. 9, pp. 1336-1339, 1998.
9. A-K. Hamid, "Scattering from dielectric coated elliptic cylinder loading a semi-elliptic channel in a ground plane," *J. of Electromagnetic Waves and Applications*, Vol. 19, No. 2, pp. 257-269, 2005.
10. A-K. Hamid, "Echo pattern width of a lossy dielectric loaded semi-elliptic channel in a ground plane," *Electromagnetics*. Submitted.
11. P. M. Morse and H. Feshbach, *Methods of theoretical physics*, vols. I and II. New York: McGraw-Hill, 1953.
12. A-K. Hamid and M. I. Hussein, "Iterative solution to the electromagnetic plane wave scattering by two parallel conducting elliptic cylinders," *J. of Electromagnetic Waves and Applications*, vol. 17, no. 6, pp. 813-828, 2003.
13. J-W. Yu, W. J. Byun and N. H. Myung, "Multiple scattering from two dielectric-filled semi-circular channels in a conducting plane: TM case," *IEEE Trans. Antennas Propag.* vol. 50, pp. 1250-1253, 2002.

14. A.-K. Hamid, M. I. Hussein, H. Ragheb, and M. Hamid, "Mathieu functions of complex arguments and their applications to the scattering by lossy elliptic cylinders," *Applied Computational Electromagnetics Society Journal*, vol. 17, no. 3, pp. 209-217, 2002.

A.-K. Hamid was born in Tulkarm, West Bank, on Sept. 9, 1963. He received the B.Sc. degree in Electrical Engineering from West Virginia Tech, West Virginia, U.S.A. in 1985. He received the M.Sc. and Ph.D. degrees from the University of Manitoba, Winnipeg, Manitoba, Canada in 1988 and 1991, respectively, all in Electrical Engineering. From 1991 to 1993, he was with Quantic

Laboratories Inc., Winnipeg, Manitoba, Canada, developing two and three dimensional electromagnetic field solvers using boundary integral method. From 1994 to 2000 he was with the Faculty of Electrical Engineering at King Fahd University of Petroleum and Minerals, Dhahran, Saudi Arabia. Since Sept. 2000 he has been an Associate Prof. in the Electrical/Electronics and Computer Engineering Department at the University of Sharjah, Sharjah, United Arab Emirates. His research interest includes EM wave scattering from two and three dimensional bodies, propagation along waveguides with discontinuities, FDTD simulation of cellular phones, and inverse scattering using neural networks.

DESIGN OF CIRCULAR POLARIZED ANTENNAS USING GENETIC ALGORITHM BASED ON CURVED WIRE ANALYSIS

Mohab A. Mangoud

Department of Electronics and Communications, College of Engineering, Arab Academy for Science and Technology, Alexandria 1029, Egypt, e-mail: mangoud@ieeee.org

Abstract—An efficient Method of Moments formulation using curved segmentation (MoM-CS) to model curl and helical antenna structures is implemented and compared to straight wire segmentation code. This integral equation solver is then employed in conjunction with genetic algorithm (GA) to design and optimize complex helical wire antennas such as Tapered Single Helical Antenna (TSHA), Single Elliptical Curl Antenna (SECA) and Tapered Quadrifilar Antenna (TQFA) mounted over infinite ground plane. An optimum gain, VSWR and circular polarization properties that make these antennas suitable to be used in satellite communications systems are obtained. The numerical results show that the hybrid GA/ MoM-CS produces superior antenna designs for such complex geometries with reduced computation time compared to codes that use straight wire segmentations.

Keywords- Method of Moments, curved segmentation, genetic algorithm, circular polarization.

I. INTRODUCTION

Many satellite and wireless communications systems require high efficiency, lightweight and low cost circularly polarized (CP) antennas. Due to the resonant characteristics, circular microstrip antennas have narrow bandwidth. However, the tapered helical, curl and quadrifilar are nonresonant antennas that radiate circularly polarized waves and they have wider bandwidth. Designing these kind of complex geometrical antennas is typically a slow haphazard process. Consequently, a numerical model and a numerical optimization of that model are important for developing realistic designs. Most of the previous work for GA / MoM formulation consider straight wires for fitness function calculations [1] and [2]. In this paper an efficient MoM algorithm is described using curved segmentation [3] to model the curved geometrical antennas, which is then run under a GA optimization routine to design an antenna with specific performance attributes similar to [4]. The use of curved segment keeps the computational time manageable

throughout the many runs required in this evolutionary procedure. The requirement of fewer segments gives the curved segment model a speed advantage therefore important when the MoM is combined with GA for optimization problems.

The organization of the paper is as follows: curved wire segmentations formulation is reported for the analysis of helical structures with its validation results in section II. In section III, GA and the MoM integration is described. In section IV the results of three circular polarized designs using the developed code are illustrated and discussed. Finally, conclusions are derived in section V.

II. CURVED WIRE SEGMENTATIONS

This section shows a novel formulation of MoM for simulation of helical structures with limited number of segments using the newly developed curved segment code. A polynomial basis current function with a Galerkin solution for both curved wire segments is applied and implemented. Helical antenna examples are studied using curved wire segments modeled using a newly implemented formulation and compared to straight wire code results.

A. Helical Antenna Description and Curved-Segment Formulation

The curved wire segment has the advantage of correcting the errors produced from integral current equations and junctions of straight segments. In this section the current distribution is assumed uniform over the wire surface transverse to the axis and therefore the approximated kernel solution is used. Curved wire geometry like the helical antenna is considered, the helical structure and its parameters being shown in Fig. 1. Z_o is the starting height of the helix, b is the helix radius and p is the pitch angle on the helix. Φ is the radial angle for the projection of helix points on the horizontal plane $z = 0$ and Φ_o is the initial radial angle describing the location of the starting point of the helix. The (x_h, y_h, z_h) coordinates of any point on the helix can be given by the following

$$\begin{aligned} x_h &= b \cos(\Phi + \Phi_o), \\ y_h &= b \sin(\Phi + \Phi_o), \quad z_h = \frac{p}{2\pi} \Phi + z_o \end{aligned} \quad (1)$$

where ($0 < \Phi_o < 2\pi$). As shown in Fig. 2 the length of one turn, L , and the pitch angle, α , can be written as $L = 2\pi b'$ and $\alpha = \tan^{-1} \frac{p}{2\pi b}$ where b' is the modified helix radius, defined as:

$$b' = \sqrt{b^2 + \left(\frac{p}{2\pi}\right)^2}. \quad (2)$$

The vector can describe the helical contour:

$$\hat{r} = x_h \hat{a}_x + y_h \hat{a}_y + z_h \hat{a}_z.$$

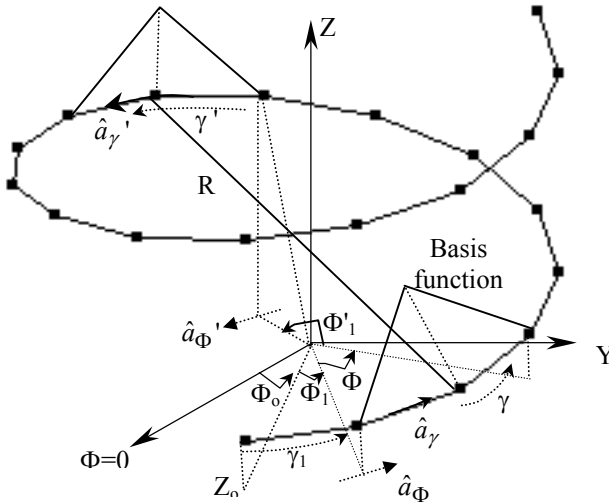


Fig. 1. Basis and weighting functions on curved segments of helical antenna.

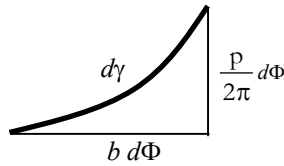


Fig. 2. Part of one curved segment showing γ and Φ .

The unit vector, \hat{a}_γ , which describes the contour of the helix is defined by

$$\hat{a}_\gamma = \frac{\partial}{\partial \Phi} \hat{r} / \left| \frac{\partial}{\partial \Phi} \hat{r} \right|. \quad (3)$$

Then it may be written as:

$$\begin{aligned} \hat{a}_\gamma &= -\cos \alpha \sin(\Phi + \Phi_o) \hat{a}_x \\ &\quad + \cos \alpha \cos(\Phi + \Phi_o) \hat{a}_y + \sin \alpha \hat{a}_z. \end{aligned}$$

The current is obtained on this general helical antenna geometry by using Galerkin type moment method for the electric field integral equation (EFIE). The surface current $J_s(r')$ is approximated as a line current given by $I(\gamma') \hat{a}_{\gamma'}$, where $\hat{a}_{\gamma'}$ is defined at the source point and follows the contour of the helix. Then, for Galerkin type functions the typical input impedance term can be written as:

$$Z_{ms} = j\omega\mu \iint_{\gamma' \gamma} \left[\begin{array}{c} f_m(\gamma) f_s(\gamma') (\hat{a}_\gamma \cdot \hat{a}_{\gamma'}) \\ -\frac{1}{k^2} \nabla_\gamma \cdot f_m(\gamma) \nabla_{\gamma'} \cdot f_s(\gamma') \end{array} \right] g(R) d\gamma d\gamma'.$$

This integral depends only on γ and γ' , the lengths of the wire contours for the source and the observation points and their corresponding \hat{a}_γ and $\hat{a}_{\gamma'}$. The basis and weighting functions for the helical antenna problem are chosen as two segments with first order polynomial (linear) functions, as shown in Fig. 1, can be given by:

$$f_s(\gamma') = \begin{cases} \frac{\gamma'}{\gamma'_{s1}} & \gamma' < \gamma'_{s1} \\ 1 - \frac{\gamma'}{\gamma'_{s2}} & \gamma' < \gamma'_{s2} \end{cases}, \quad f_m(\gamma) = \begin{cases} \frac{\gamma}{\gamma_{m1}} & \gamma < \gamma_{m1} \\ 1 - \frac{\gamma}{\gamma_{m2}} & \gamma < \gamma_{m2} \end{cases} \quad (4)$$

where γ_{m1} and γ_{m2} are the lengths of the two segments of the weighting function and γ'_{s1} and γ'_{s2} are the lengths of the two segments of the basis function.

B. Computation of the Integral Used in the Impedance Matrix Elements for Curved Segments

For computing the impedance matrix elements it can be expressed in terms of the radial horizontal angle Φ instead of the contour length γ as follows:

$$\begin{aligned} V_{factor} &= f_m(b'_m \Phi) f_s(b'_s \Phi') (\hat{a}_\gamma \cdot \hat{a}_{\gamma'}) \\ &\quad - \frac{1}{k^2} f_m(\gamma) \Big|_{b'_m \Phi} f_s(\gamma') \Big|_{b'_s \Phi'} \end{aligned}$$

$$Z_{ms} = j\omega\mu \iint_{\Phi' \Phi} [V_{factor}] g(R) b'_s b'_m d\Phi d\Phi' \quad (5)$$

where $\gamma' = b'_s \Phi'$ and $\gamma = b'_m \Phi$ as shown from Fig. 2 while b'_m and b'_s are defined in equation (1), and

$$f'_s(\gamma')|_{b_s, \Phi'} = \frac{\pm 1}{b'_s \Phi'_s} \text{ and } f'_m(\gamma')|_{b_m, \Phi} = \frac{\pm 1}{b'_m \Phi'_m} \quad (6)$$

where Φ'_s and Φ'_m are the radial horizontal angles covering the segments lengths over the basis and test functions, γ_s and γ_m respectively, assuming the use of curved segments with equal lengths. Before equation (3) can be implemented, the dot product ($\hat{a}_\gamma \cdot \hat{a}_{\gamma'}$) and the distance R between the source and the observation points on curved segments in terms of Φ and Φ' must be defined. The dot product term is given by:

$$\begin{aligned} \hat{a}_\gamma \cdot \hat{a}_{\gamma'} &= \cos^2(\alpha) \sin(\Phi + \Phi_1 + \Phi_o) \sin(\Phi' + \Phi'_1 + \Phi_o) \\ &+ \cos^2(\alpha) \cos(\Phi + \Phi_1 + \Phi_o) \cos(\Phi' + \Phi'_1 + \Phi_o) \quad (7) \\ &+ \sin^2(\alpha). \end{aligned}$$

The distance R can be written as

$$R = \sqrt{\begin{aligned} &(b \cos(\Phi + \Phi_1 + \Phi_o) - b \cos(\Phi' + \Phi'_1 + \Phi_o))^2 \\ &+ (b \sin(\Phi + \Phi_1 + \Phi_o) - b \sin(\Phi' + \Phi'_1 + \Phi_o))^2 \quad (8) \\ &+ \left(\frac{p\Phi}{2\pi} - \frac{p\Phi'}{2\pi}\right)^2 + a^2 \end{aligned}}$$

where Φ_1 and Φ'_1 are the starting radial angles for the source and observation curved segments, as shown in Fig. 1. Substituting equations (6), (7) and (8) into equation (5), makes the integral a function of Φ and Φ' only. A Fortran computer subroutine was written to solve this integral by dividing it into real and imaginary parts of the Green's function. The integral with respect to Φ' is solved numerically by using a Gaussian-Legendre Formula for 8-16 points, while two integrals over Φ for both real and imaginary parts are also solved numerically, that solves singular or pseudo-singular integral adaptively within 10^{-6} relative error. In this case, the approximated kernel is used, thus pseudo-singular integrals are considered.

The mathematical analysis and numerical solutions given in this section were simulated by the (MoM-CS) computer program. The results obtained from this MoM-CS code are compared with equivalent ones from the 'Numerical Electromagnetics Code' (NEC). It should be stated that NEC has different basis and weighting functions for its solution from those used in (MoM-CS). Also, unlike (MoM-CS), NEC uses straight wire approximations to model curved wire antennas. An investigation of the current distribution in wire antennas and especially normal-mode helical antennas (NMHA) will be demonstrated. The input resistance is particularly used to test (MoM-CS)

subroutines discussed earlier. Considering a center-fed normal mode helical antenna in free space with the following parameters; helix radius $b = 0.0273$ m; pitch $p = 0.03646$ m; number of turns $n = 10$; and wire radius $a = 0.001$ m. The helix is oriented along the z -axis and it starts from the x -axis ($\Phi = 0$).

Figure 3 shows the convergence plots of input resistance of the specified helix. It is seen that significantly fewer segments are needed when the curved segments of (MoM-CS) are used versus NEC straight wire segments representing the curved helix geometry. For straight wire segments, the accuracy of the thin-wire approximation for a wire of radius a and segment length Δ is acceptable, within 1% error, for the following condition; $8a < \Delta < 0.1\lambda$, while if the extended thin-wire kernel is used $2a < \Delta$ could be used [5]. NEC results are fairly well converged at 401 segments or 40 segments per turn. The (MoM-CS) models with curved segments are stable for numbers of 21 curved segments or 2 segments per turn, so it can be said that the number of segments is reduced by 20 times which means more efficiency in terms of unknowns and computer memory for modeling curved structures. Also one should be careful when modeling curved geometries using straight wire segments to avoid the unstable region when modeling the helix with small numbers of segments (51 segments in this example).

For testing (MoM-CS) over a wide band, the response of the input impedance of the previous ten-turn NMHA is presented in Fig. 4 for input reactance versus the frequency for various pitch distances. The results of 21 segmentations with (MoM-CS) agree well with those calculated using 401 segments with NEC. Three different pitch distances of 0.036, 0.045, and 0.054 m are used with fixed axial length for the helix, which means that the number of turns and the total length of the wire are changed. From the obtained results it can be concluded that MoM-CS routines performs well and the use of curved segments allows accurate modeling especially for normal mode helical antenna.

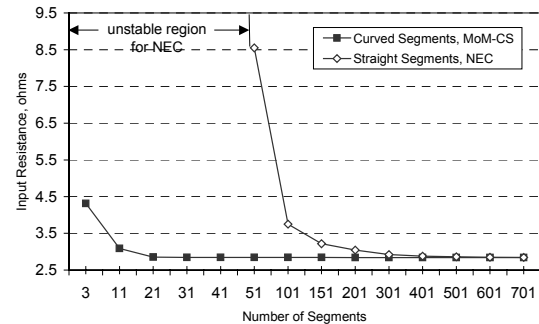


Fig 3. Normal mode center fed helix input resistance convergence versus number of segments.

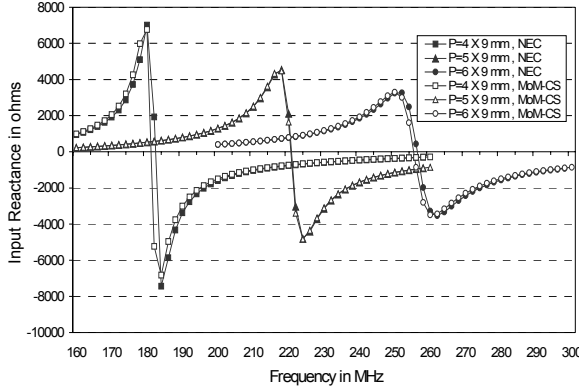


Fig. 4. The input reactance of a ten-turn NMHA for various pitch distances using MoM-CS and NEC.

III. GA AND THE METHOD OF MOMENTS INTEGRATION

The GA/MoM-CS integration program is developed to utilize the numerical calculations for the fitness function of the GA program by curved wire segmentation formula. That significantly reduces the computational cost of the optimization process compared to the MoM approach that uses linear segmentations. Fewer curved basis functions are required for an accurate representation of the spiral or curved contour and current distribution. Moreover, the speeds up of the matrix inversion process for the MoM technique, leading to a reduction in the cpu time and the used memory becomes increasingly important when the code is linked with the GA optimization procedures that need to run the MoM code many times.

In any optimization problem, candidate solutions are evaluated according to a fitness function. For antennas used in satellite systems, the optimization criteria targeted is a good CP main lobe at a specific angle with respect to the antenna axis with good gain and low VSWR (good matching). The objective (fitness) function for one iteration (chromosome) involves solving an electric field integral equation with the previously described curved segment formulation. The GA code initializes a random sample of individuals with different parameters that maps the antenna geometrical parameters that are optimized by evolution via survival of the fittest. That is calculated using the numerical technique of MoM-CS. The selection scheme used is tournament selection with a shuffling technique for choosing random pairs for mating. The routine includes binary coding for the individuals, jump mutation, creep mutation, and uniform crossover. Mutation caused small random changes in chromosomes so that the search doesn't trap

in a local optimum. The process is repeated till the algorithm converges.

IV. SIMULATIONS AND NUMERICAL RESULTS

The efficiency of the developed hybrid GA/MoM-CS code is illustrated by using it to design three different complex helical structures for mobile satellite applications. These antennas are optimized to have good circular polarization properties with a high gain and minimum VSWR values. The antennas are Tapered Single Helical Antenna (TSHA), Single Elliptical Curl Antenna (SECA) and Tapered Quadrifilar Antenna (TQFA) mounted over infinite ground plane. For these antennas, the GA/MoM-CS is allowed to search for the optimum configuration that will produce the desired properties. The fitness function of GA is obtained by MoM-CS to evaluate the average gain over the elevation angles (Av-gain), average axial ratio over the elevation angles (AR) and average voltage standing wave ratio over the operating frequencies (VSWR) in terms of the optimization parameters is given as:

$$\frac{1}{NM} \sum_f \left(\sum_{\theta} A \times \text{gain}(f, \theta) + \sum_{\theta} B \times \text{Axia}(f, \theta) \right) + \frac{N \times C}{\sum_f \text{VSWR}(f)}$$

where A, B and C are constants chosen by user, N is the number of frequency steps, f is the frequency. M is the number of elevation angle steps, θ is the elevation angle. We chose to weight the axial ratio and the gain more heavily than the VSWR as it is possible to enhance the VSWR by using a matching technique. This fitness Function is constrained such that the average VSWR lies between 1 and 10 and if it is not satisfied the fitness function resets to zero and the population is discarded. For the following examples, 1.8 GHz is selected here as a convenient operating frequency because it falls close to the transmitting and receiving bands (L and S band) of the LEO personal satellite systems. However, dual band optimization could be performed.

A. Tapered Single Helical Antenna (TSHA):

Figure 5 defines the basic geometric parameters of the TSHA over the ground plane on elevation and side view angles. The helix has overall length h_1 and tapers from a radius of r_o at the base to r_1 at the top, a taper angle β and a pitch p . The wire has a radius r and a tilted wire feeds the helix over the ground with a height h_2 . The six parameters p, h_1, r_o, r_1, r and h_2 are encoded

each into 6 bit genes. The parameters of the GA are number of population = 8, discard rate = 0.5 and mutation rate = 0.1, number of generations = 500. That means that for each run the GA routine requires 4000 evaluations of the fitness function obtained by the numerical MoM-CS technique. The gain and axial ratio are samples every 30-degree in elevation. From $\theta = -90$ to 90 for azimuth angle $\phi = 0$ at operating frequency of 1800 MHz. It is found that 30-degree increments yield better circular polarization performance than 5, 10 and 20-degree sampling steps. Then the gain and AR is averaged over the angles and frequencies for dual and tri band designs. The six optimization parameters are as shown in the table 1

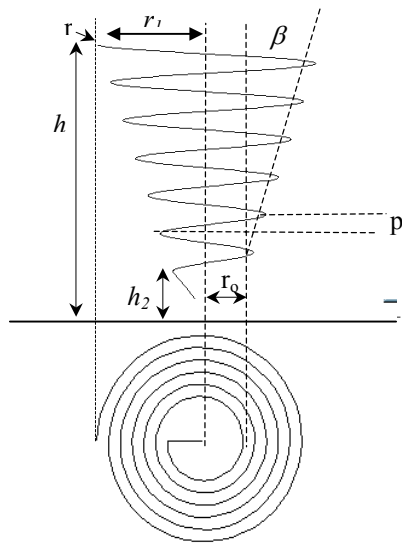


Fig. 5. Tapered Single Helical Antenna (TSHA) configuration and optimization parameters.

The genes used along with their permitted range variations are shown in Table 1. The highest ranked chromosome has characteristics determined by the genes in the right hand column of the table.

Table 1. TSHA optimization Genes and optimum results

Genes	Range		Optimum
	From	To	
Pitch	0.001	0.05	0.028222
Total length	0.001	0.05	0.049222
Base radius	0.001	0.05	0.025111
Top radius	0.001	0.05	0.028222
Wire radius	0.001	0.005	0.001063
Feeder height	0.01	0.05	0.013174
Av. gain = 2.05	Av. AR = 0.57		VSWR = 3.25

The optimized average gain, average axial ratio from -90 to 90 and VSWR over the operating band for the best chromosome are illustrated in the last row in Table 1. Clearly these values are acceptable and show good circular polarization properties. Other ranked individual chromosomes may have higher values for one of the three-design parameters; but the chosen one has the highest fitness function for the three-scaled values combined together.

B. Single Elliptical Curl Antenna (SECA)

The type of curl antenna investigated here is an elliptical spiral antenna with a single arm fed by a 5 cm prob against infinite perfectly conducting ground plane. The general configuration of the SECA is shown in Fig. 6. It is made of a thin wire of radius r and is bent and curled above the ground plane. The antenna is composed of a straight vertical and horizontal and a curled horizontal section. Generally, the curled section can take the shape as shown in Fig 6.

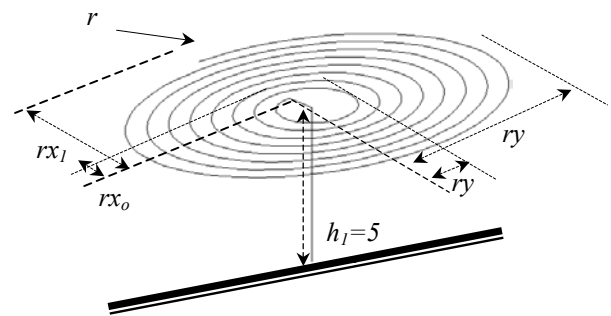


Fig. 6. General Configuration of Elliptical curl antenna and top view with optimization parameters.

The curved equation of the curled section is: $x = a \phi \cos(\phi)$, $y = a \phi \sin(\phi)$, where a and b are constants if $a=b$ this antenna will be a circular curl antenna. ϕ is the winding angle starting at ϕ_0 , and ending at $\phi_1 = \phi_0 + 2\pi \times$. A range of parameters is assigned to find the design that gives the optimum characteristics. These parameters are as shown in Fig. 6, where N : number of turns, rx_0 : inner radius in x-axis; rx_1 : outer radius in x-axis, ry_0 : inner radius in y-axis, ry_1 : outer radius in y-axis and r : wire radius. The GA/MoM-CS described earlier is used to optimize the values. Different segments were tested to evaluate the stability of the results. The constraints on the designed parameters are given in table 2. The maximum antenna dimension is chosen to be 10 cm in radius that can be changed depending on the required volume.

The program initializations and the chromosomes structures are similar to the previous TSHA runs. Also, the same fitness function is applied to obtain the minimum VSWR, maximum average axial ratio and maximum average gain over the ± 90 angular angles

from the zenith in the x-z elevation plane sampled each 30-degree at 1800 MHz. The results of GA/MoM-CS for the optimum design configuration and best fitness functions values are illustrated at the left column and bottom row of Table 2. Good circular polarization properties with nearly similar values of gain, AR and VSWR to the previous antenna are obtained. It is found that the best design has the same value for the outer radius in x and y-axis, which produces circular curl geometry.

Table 2. SECA optimization Genes and optimum results

Genes	Range		Optimum
	From	To	
Number of turns	1	10	4
Inner radius: x-axis	0.001	0.01	0.001143
Outer radius: x-axis	0.015	0.1	0.098651
Inner radius: y-axis	0.001	0.01	0.001429
Outer radius: y-axis	0.015	0.1	0.098651
Wire radius	0.001	0.005	0.003731
Av. Gain =6.2	Av. AR=0.55		VSWR=7.4

C. Tapered Quadrifilar Antenna (TQFA):

One of the best candidates for the satellite applications is the quadrifilar antenna. Thus, Tapered Quadrifilar Antenna (TQFA) with nonuniform radius is chosen to be optimized by the developed GA/MoM-CS code. The TQFA of Fig. 7 has the following geometrical parameters: r_o , r_1 , r , p and h_1 respectively for base radius, top radius, wire radius, pitch and total length.

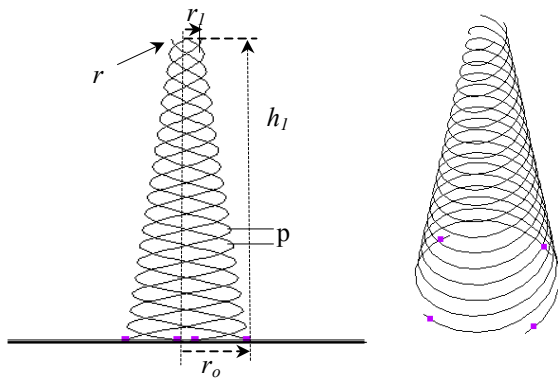


Fig. 7. Tapered quadrifilar helical antenna 3D and side view with optimization parameters.

The above five parameters are optimized using GA/MoM-CS employing 30 bit chromosomes, 8 populations and 500 generations. The rest of the GA parameters are the same as the previous two cases. The Quadrifilar structure with its four helices required many basis functions to represent the vector direction of the current along the meandering wire. That means more computational time and memory is required for this structure. However, the results of the optimum designs are shown in the left column and the last row of Table 3.

These results indicates that this antenna has high average axial ratio = 0.71 for the zenith coverage and it better than the previous two designs. The average computational run time is about 1 h on a Pentium IV processor.

Table 3. TQFA optimization Genes and optimum results

Genes	Range		Optimum
	0.01	0.02	
Pitch	0.01	0.02	0.018095238
Total length	0.02	0.05	0.044761905
Base radius	0.001	0.05	0.029777778
Top radius	0.001	0.05	0.008777778
Wire radius	0.001	0.005	0.004936508
Av. Gain =2.11	Av. AR=0.71		VSWR=4.63

Finally, the best three designs for the previous case studies are compared together. Figure 8 shows the axial ratio versus the elevation angle θ for the three antennas mounted on infinite ground plane at 1800 MHz and at $\phi=0$. Generally, true circular polarization is achieved for wide angular coverage. The polarization purity is acceptable for the axial ratio under 3 dB level. Thus TSHA has good circular polarization characteristics for the θ in the range between -37° and 65° . However, this range is between -45° and 55° for SECA. The best result is found to be for the TQHA that provides low axial ratio in the symmetric range $\pm 77^\circ$.

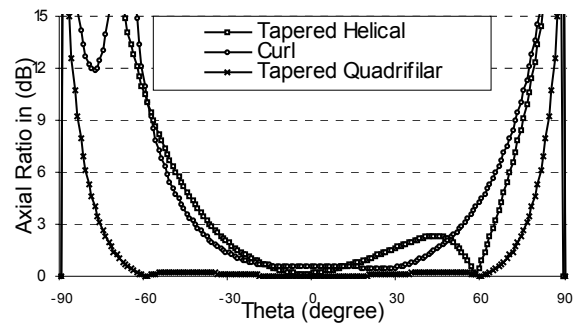


Fig. 8. Computed axial ratio versus the elevation angle. θ for the three antennas mounted on infinite ground plane.

Figure 9 illustrates the power gain pattern for the elevation cut corresponding to azimuth angle of 0° . We note that for these three cases the coverage is excellent over most of the $\pm 90^\circ$ zenith range. The previous result indicates that TQHA gives the best circular polarization and that the developed GA/MoM-CS performs well in designing such antennas.

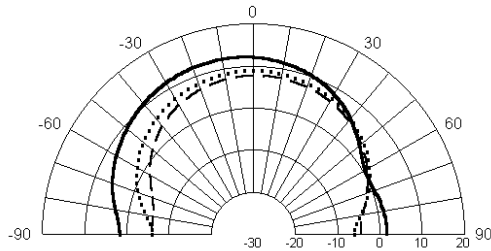


Fig. 9. Power gain in the xz plane for the three antennas at 1800 MHz. (— SECA, TSHA, - - - TQHA).

V. CONCLUSION

Tapered Single Helical Antenna (TSHA), Single Elliptical Curl Antenna (SECA) and Tapered Quadrifilar Antenna (TQFA) mounted over infinite conducting ground plane have been designed using GA with MoM-CS optimization technique. Good circular polarization properties, high zenith gain and minimum VSWR were considered in the evaluation of the numerical fitness function to produce optimum geometrical parameters of these antennas. Such combination of antenna characteristics would be difficult to achieve through extensive runs for MoM alone especially for complex helical and curl structures. It is concluded that the efficient GA/MoM-CS holds much promise in the development of new designs for satellite antenna applications with its circular polarization requirements.

ACKNOWLEDGEMENTS

The author gratefully acknowledges Prof. P. S. Excell and Dr. R. A. Abd-Alhameed at university of Bradford, UK, for their support in developing the MoM-CS code.

REFERENCES

- [1] E. E. Altshuler, "Design of a vehicular antenna for GPS /Iridium using a genetic algorithm", *IEEE Trans. on Antennas and Propagation*, vol. 48, no. 6, pp. 968 – 972, June 2000.
- [2] S. R. Rengarajan, "On the cross-polarization characteristics of crooked wire antennas designed

by genetic algorithms" *proceeding of IEEE APS Symposium*, vol. 1, pp.706 – 709, June 2002.

- [3] R. A. Abd-Alhameed, P. S. Excell, "Complete surface current distribution in a normal-mode helical antenna using a Galerkin solution with sinusoidal basis functions", *IEE Proceedings Science, Measurement and Technology*, vol. 149, no. 5, pp. 272 – 276, Sept. 2002
- [4] R. M. Edwards, G. G. Cook, S. K. Khamas, R. J. Aidley, "Design of circularly polarized printed spiral antenna using dual objective genetic algorithm" *Electronics Letters*, vol. 34, no. 7, pp. 608 - 609, April 1998.
- [5] G. J. Burke and A. J. Poggio, "Numerical electromagnetics code (NEC): method of moments," US Naval Ocean Systems Centre, San Diego, Rep. no. TD116, 1981.



Mohab A. Mangoud (S'97-M'01) was born in Alexandria, Egypt, in 1971. He received the B.Sc. and M.Sc. degrees, both in electrical engineering, from Alexandria University, Egypt, in 1993 and 1996 respectively, and the Ph.D. degree in electrical and Electrical Engineering, University of Bradford, UK in 2001. He

is currently an Assistant Professor in the Electronics and Communications Engineering Department, Arab Academy for Science and Technology and Maritime Transport (AAST), Alexandria, Egypt, where he worked since 1993. He is responsible for teaching antennas and wireless communications courses. His research interests include modeling of electromagnetic systems, antenna design and smart antennas.

Comparison of return loss calculations with measurements of narrow-band microstrip patch antennas

Hossam Abdallah, Wasyl Wasylkiwskyj

Department of Electrical and Computer Engineering, The George Washington University
Washington DC 20037, USA

Kunal Parikh, Amir Zaghloul

Department of Electrical and Computer Engineering, Virginia Polytechnic Institute and State University
VA 22043, USA

Abstract: The return loss of rectangular, single layer, coax fed patch antennas designed to resonate at 1904 MHz was computed using WIPL-D and HFSS and the results compared with experiment. Both codes predicted the bandwidth at -10 dB return loss points with good accuracy but not the resonant frequency and the corresponding return loss. It was also found that the resonant frequency predicted by WIPL-D was substantially closer to the experimental value than that predicted by HFSS.

1. INTRODUCTION

With growing use of microstrip antennas in a variety of applications, there is a great need for modeling and analysis software packages that can accurately and efficiently predict the performance of these antennas. The cost, ease of use, and the time spent in both the design and calculations are additional and important key factors in selecting a software package. A number of microstrip antennas modeling software packages are compared in [1] where it is shown that custom-written codes are more accurate than standard commercial packages. In this paper designs of single-layer coax fed rectangular microstrip patch antennas are examined using WIPL-D and HFSS (High-Frequency Structure Simulator) software packages and the results compared with experiment.

WIPL-D is a frequency domain moment method program that models metallic and/or dielectric/magnetic structures (antennas, scatterers, passive microwave circuits, etc.) [2]. The geometry of the structure is defined in an interactive way using a combination of wires, plates and material objects. HFSS is a frequency domain finite element code. The version used in this paper is Agilent Version 5.6.

Instead of using the performance measures introduced in [1] here comparisons of computed and experimental results employ the return loss as a function of frequency.

The initial patch dimensions and substrate thickness were chosen on the basis of a standard simplified

transmission line model [3], [4] and subsequently adjusted in accordance with repeated applications of WIPL-D. Once the dimensions and feed point position that yield a match at the desired resonant frequency (1904 MHz) were determined the return loss was computed as a function of frequency. Both a single patch and a 3-element linear patch array were modeled. The calculations were then repeated with HFSS. Several patch antennas were fabricated with dimensions held to within 10 microns of the values used in the calculations. Special care was exercised to duplicate the physical parameters of the coaxial feed used in the computer models. Measurements of return loss were carried out using a carefully calibrated HP 8722D network analyzer.

2. PATCH GEOMETRY AND COAXIAL FEED

Fig. 1 shows the geometry of a single-layer patch antenna, where L denotes the length and W the width. The patch is fed by a coaxial line (Fig. 2) with the feed point located at x_r and $y_r = W/2$. The dimensions of the rectangle defining the extent of the ground plane are denoted by u and v . Figure 2 shows the cross-section of the rectangular patch and substrate in the E-plane. The length of the coaxial line is T and the radii of the inner and outer conductors are r_0 and r_1 , respectively. The dielectric constant of the coaxial line is ϵ_1 and only the inner conductor is extended into the substrate. The coaxial line characteristic impedance was kept at 50 Ohms with r_0 and r_1 as well as the dielectric constant chosen to corresponding to a standard SMA connector.

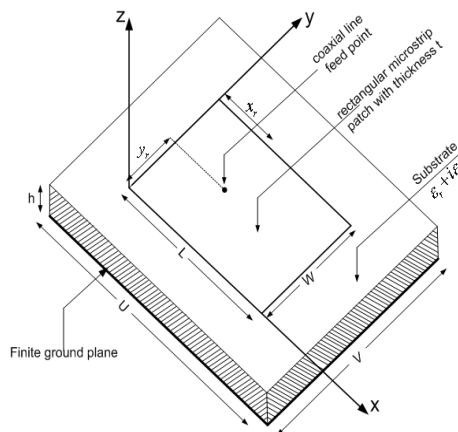


Fig. 1. Rectangular microstrip patch.

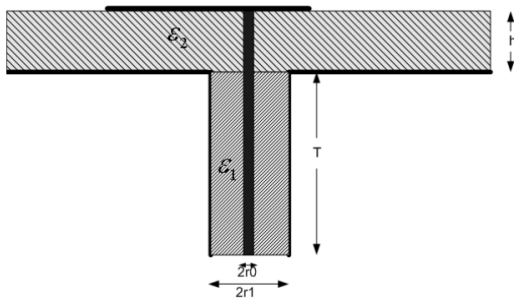


Fig. 2. Rectangular microstrip patch, E-plane cut.

3. COMPARISON OF RETURN LOSS COMPUTED USING WIPL-D AND HFSS

The computations assumed perfectly conducting patches with a thickness of 35 microns. The substrate material was RT/duroid 5880 with manufacturer's specified dielectric constant $\epsilon_2 = 2.2(1 - i0.0009)$ (where the loss tangent corresponds to vendor's measured value at 10GHz) and a thickness $h = 1.575mm$. It is worth mentioning that WIPL-D simulations with loss tangents between 0.0009 and 0.0004 (the vendor's value at 1 MHz) yielded negligible differences both in regard to bandwidth and resonant frequency. Calculations were performed for a single patch radiator and a linear array of three identical patches aligned in the E-plane. Referring to Fig. 2 the pertinent dimensions for the single patch were $L=51.22\text{ mm}$, $W=60\text{ mm}$, $X_r=0.35L$, $Y_r = W/2$, $u=L+40h$, and $v=W+40h$.

The accuracy levels in WIPL were chosen to be enhanced 2 for both the current expansion and integral accuracy. In addition, double edging (finer resolution) around the patch edges were specified [2]. In HFSS, the *port* boundary condition is used. Furthermore, the *ground plane* boundary condition is used in the model. The final calculations of the field and the S-parameters depend on the precision of the mesh and hence mesh refinement is performed. The frequency of refinement was chosen in such a manner that the return loss at this frequency is expected to be 10 dB or better.



Fig. 3. Top and bottom views of typical test patches.

Two sets of identical patches and arrays were

fabricated. A panel comprised of 35 micron (1 oz) rolled copper on both sides with RT/5880 Duroid 0.062" substrate sandwiched in between was used for this purpose. One side of the panel was etched to produce patch radiators with the desired dimensions while on the other side SMA flanged 50 Ohm connectors were attached with screws to 1/4 inch thick copper extenders that were glued to the 35 micron copper ground plane using a highly conducting epoxy. The top and bottom of the resulting configurations are shown in Fig. 3. The return loss was measured using the HP 8722D network analyzer. The three-element array was centered on a ground plane/substrate with dimensions $u=114.2\text{ mm}$ and $v=304.8\text{ mm}$, as shown in Fig. 4.

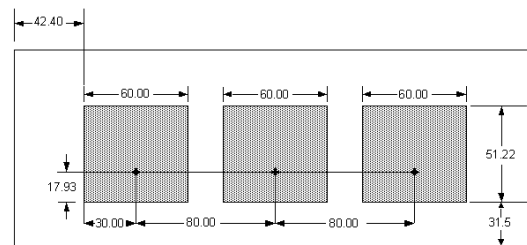


Fig. 4. 3-element patch array.

To test for measurement repeatability and for effects of possible dimensional deviations two sets of identical configurations were fabricated and measured. No differences were discerned in the measured return loss. In Fig. 5 the plots of the return loss for the single element patch antenna computed by WIPL-D and HFSS are compared with the experimental curve. The measured results show that the patch resonates at 1909 MHz. Clearly the resonances predicted by both WIPL-D (1904 MHz) and HFSS (1886 MHz) deviate from the experimental value.

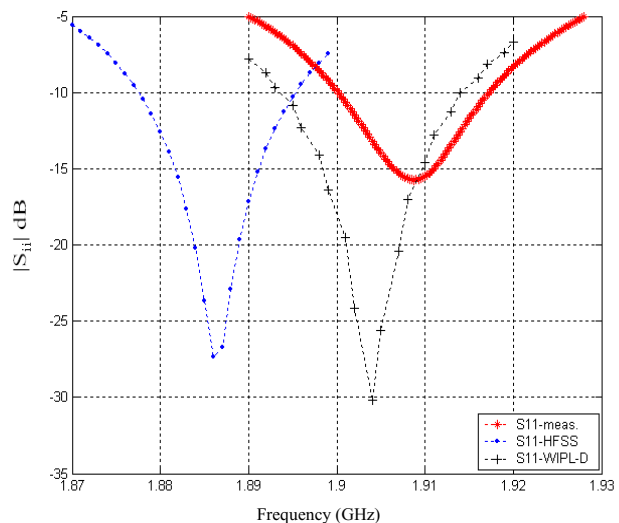


Fig. 5. Return loss predicted by WIPL-D and HFSS with for a single patch compared with experiment.

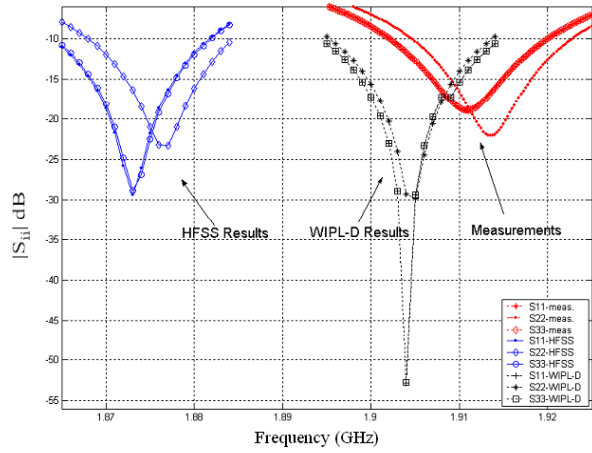


Fig. 6. Return loss predicted by WIPL-D and HFSS with for a 3-element patch compared with experiment.

The extent to which the disagreements of calculations with measurement can be attributed to deviations of the dielectric constant from its nominal value of 2.20 was investigated by carrying out the return loss computations with WIPL-D over the full tolerance range (2.19-2.22) certified by the vendor (Rogers Corp.) The results are plotted in Fig. 7. As shown in the figure, the predicted resonant frequency varied from 1.896 GHz to 1.908 GHz (The return loss curve corresponding to the nominal value of 2.2 is indicated by the thick solid line.).

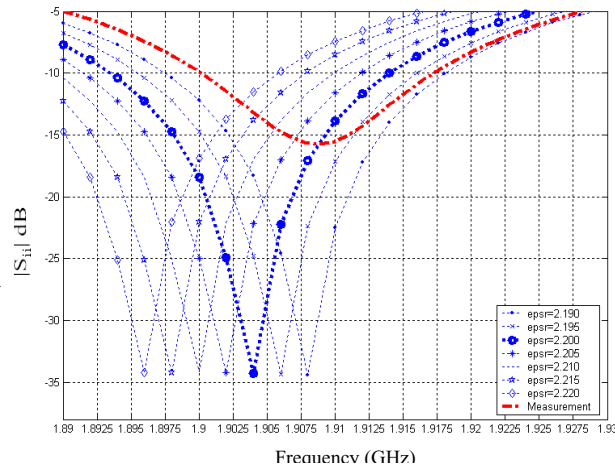


Fig. 7. WIPL-D calculations showing the change in the resonant frequency when the substrate dielectric constant was varied over the tolerance range certified by the vendor.

4. CONCLUDING REMARKS

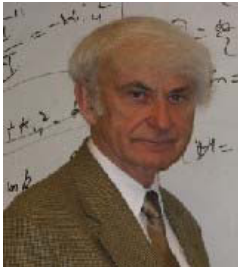
The plots in Figs. 5 and 6 show noticeable differences between WIPL-D and HFSS modeling capabilities, with WIPL-D results closer to experimental data.

5. REFERENCES

- [1] D. M. Pozar, S. M. Duffy, S. D. Targonski, N. Herscovici, "A comparison of commercial software packages for microstrip antenna analysis", *Antennas and Propagation Society International Symposium, IEEE*, vol. 1, pp. 152 –155, July 2000.
- [2] B. Kolundzija, J. S. Ognjanovic, T. K. Sakar, *WIPL-D: Electromagnetic Modeling of Composite Metallic and Dielectric Structures - Software and User's Manual*, Artech House Inc., 2000.
- [3] P. Bhartia, Inder Bahl, R. Garg, A. Ittipiboon, *Microstrip Antenna Design Handbook*, Artech House Inc., 2001.
- [4] P. Perlmutter, S. Shtrikman, D. Treves, "Electric surface current model for the analysis of a microstrip rectangular element", *Antennas and Propagation Society International Symposium*, vol. 22, pp. 577–580, Jun 1984.



Hossam A. Abdallah was born in Alexandria, Egypt, in 1973. He received his Bachelor of Science degree in computer science in 1995 from Alexandria University, Alexandria, Egypt. In 2001 he received his MSc degree in Engineering Mathematics from Twente University, Enschede, The Netherlands. Since August 2001, Mr. Abdallah is pursuing his PhD degree in the area of array signal processing and also working as a research assistant at the Department of Electrical and Computer Engineering, The George Washington University, Washington DC, USA. His current research activities are computational electromagnetics and array signal processing.



Wasyl Wasyliwskyj (F'97) received his BEE degree from the City University of New York in 1957 and the MS and Ph.D. degrees in electrical engineering from the Polytechnic University in 1965 and 1968, respectively. His past research and industrial experience covers a broad spectrum of electromagnetics, including microwave components and techniques, phased array antennas, propagation and scattering, radar cross-section modeling as well as modeling of geophysical and oceanographic electromagnetic phenomena. In addition, he has extensive experience in ocean and structural acoustics with applications to active SONAR. Since 1985 Dr. Wasyliwskyj has held the position of Professor of Engineering and Applied Science at the George Washington University, Washington, DC. His current research activities are primarily in numerical electromagnetics and array antennas for direction-of-arrival estimation.



Kunal Parikh was born on June 14, 1980 in Ahmedabad, India. He earned his Bachelors of Engineering degree in Electronics & Communications from Nirma Institute of Technology affiliated with the Gujarat University in 2001. He then joined the Blacksburg campus of Virginia Tech as a Master's student in the Bradley Department of Electrical and Computer Engineering. In the summer of 2002, he moved to the Alexandria Research Institute of the Northern VA campus, where he worked as a Graduate Research Assistant for the rest of his program. This work was carried out as part of his Master's thesis. Kunal is now an employee of LCC International, Inc. and works as an RF Design & Optimization engineer.



Amir I. Zaghloul received the Ph.D. and M.A.Sc degrees from the University of Waterloo, Canada in 1973 and 1970, respectively, and the B.Sc. degree (Honors) from Cairo University, Egypt in 1965, all in electrical engineering. In 2001 he joined Virginia Polytechnic Institute and State University (Virginia Tech) as Professor in the Bradley Department of Electrical and Computer Engineering. Prior to Virginia Tech., he was at COMSAT Laboratories for 24 years performing and directing R&D efforts on satellite communications and antennas, where he received several research and patent awards, including the Exceptional Patent Award. He held positions at the University of Waterloo, Canada (1968-1978), University of Toronto, Canada (1973-74), Aalborg University, Denmark (1976) and Johns Hopkins University, Maryland (1984-2001). He is a Fellow of the IEEE and the recipient of the 1986 Wheeler Prize Award for Best Application Paper in the IEEE Transactions on Antennas and Propagation. He is also an Associate Fellow for The American Institute of Aeronautics and Astronautics (AIAA), a Member of Commissions A & B of the International Union of Radio Science (URSI), and member of the IEEE Committee on Communications and Information Policy (CCIP). Dr. Zaghloul is the general chair of the upcoming "IEEE International Symposium on Antennas and Propagation and USNC/URSI Meeting," which will take place in Washington, D.C. in 2005.

ADAPTIVE NEURO-FUZZY INFERENCE SYSTEM FOR COMPUTING THE RESONANT FREQUENCY OF CIRCULAR MICROSTRIP ANTENNAS

Kerim Guney¹ and Nurcan Sarikaya²

¹ Department of Electronics Engineering, Faculty of Engineering, Erciyes University, 38039, Kayseri, Turkey,
e-mail: kguney@erciyes.edu.tr

² Department of Aircraft Electrical and Electronics, Civil Aviation School, Erciyes University, 38039, Kayseri,
Turkey, e-mail: nurcanb@erciyes.edu.tr

ABSTRACT: A new method for computing the resonant frequency of the circular microstrip antenna, based on the adaptive neuro-fuzzy inference system (ANFIS), is presented. A hybrid learning algorithm is used to identify the parameters of ANFIS. The results of the new method are in excellent agreement with the experimental results reported elsewhere.

1. INTRODUCTION

Microstrip antennas (MSAs) have many attractive features such as low profile, light weight, ease of manufacture, conformability to curved surfaces, low production cost, and compatibility with integrated circuit technology [1-5]. These attractive features have recently increased the application of MSAs and stimulated greater effort to investigate their performances. MSAs have been used in various configurations: square, rectangular, circular, triangular, trapezoidal, elliptical etc. Circular microstrip patches can be used as resonant antennas, and also as planar resonators for oscillators and filters in microwave integrated circuits. In circular MSA designs, it is important to determine the resonant frequencies of the antenna accurately because MSAs have narrow bandwidths and can only operate effectively in the vicinity of the resonant frequency. Thus, a model to determine the resonant frequency is helpful in antenna designs. Several methods [1-29], varying in accuracy and computational effort, have been proposed and used to calculate the resonant frequency of circular MSAs. These methods can be broadly classified into two categories: analytical and numerical methods. The analytical methods, based on some fundamental simplifying physical assumptions regarding the radiation mechanism of antennas, are the most useful for practical designs as well as for providing a good intuitive explanation of the operation of MSAs. However, these methods are not suitable for many structures, in particular, if the thickness of the substrate is not very thin. The numerical methods are mathematically complex, take tremendous computational efforts, still can not make a practical antenna design feasible within a reasonable period of time, require strong background knowledge and have time-consuming numerical calculations which need very expensive software packages. So, they are not very attractive for the interactive computer aided design (CAD) models. In

general, the numerical methods are based on an electromagnetic boundary problem, which leads to expression as an integral equation, using proper Green's function, either in the spectral domain, or directly in the space domain, using moment methods. Without any initial assumption, the choice of test functions and the path integration appear to be more critical during the final, numerical solution. The numerical methods also suffer from the fact that any change in the geometry (patch shape, feeding method, addition of a cover layer, etc.) requires the development of a new solution. Furthermore, the theoretical resonant frequency results calculated from the curve-fitting formulas [18], [21] based on the rigorous numerical methods are not in good agreement with the experimental results [6], [8], [11], [14-17]. However, the results of these curve-fitting formulas are in very good agreement with the results of numerical methods [1-5].

In this paper, a new method based on the adaptive neuro-fuzzy inference system (ANFIS) [30], [31] is presented to calculate accurately the resonant frequencies of the circular MSAs. First, the antenna parameters related to the resonant frequencies are determined, and then the resonant frequencies depending on these parameters are calculated by using the ANFIS. The ANFIS is a class of adaptive networks which are functionally equivalent to fuzzy inference systems (FISs). It combines the powerful features of FISs with those of artificial neural networks (ANNs). A hybrid learning algorithm [30, 31], which combines the least-square method and the backpropagation algorithm, is used to determine optimally the values of ANFIS parameters. Fast and accurate learning, excellent explanation facilities in the form of semantically meaningful fuzzy rules, the ability to accommodate both data and existing expert knowledge about the problem, and good generalization capability features have made neuro-fuzzy systems popular in recent years [30-34]. Because of these attractive features, the ANFIS in this paper is used to model the relationship between the parameters of the circular MSAs and the measured resonant frequency results.

In previous works [35-37], we successfully used ANFIS to calculate the resonant frequency of triangular MSAs and the input resistance of rectangular and circular MSAs. We also proposed FISs [38], [39] and ANNs [40-50] for computing

accurately the various parameters of the rectangular, circular, and triangular MSAs, and pyramidal horn antennas. In the following sections, the resonant frequency of a circular MSA and the ANFIS are described briefly, and the application of ANFIS to the computation of the resonant frequency of a circular MSA is then explained.

2. RESONANT FREQUENCY OF A CIRCULAR MICROSTRIP ANTENNA

Figure 1 shows a circular patch of radius r_o over a ground plane with a substrate of thickness h and a relative dielectric constant ϵ_r . The resonant frequency of this circular MSA for the TM_{nm} mode is expressed as

$$f_{nm} = \frac{\alpha_{nm} c_o}{2\pi r_o \sqrt{\epsilon_r}} \quad (1)$$

where α_{nm} is the m th zero of the derivative of the Bessel function of order n and c_o is the velocity of electromagnetic waves in free space. The dominant mode is TM_{11} ($n = m = 1$), for which $\alpha_{11} = 1.84118$. Equation (1) is based on the assumption of a perfect magnetic wall and neglects the fringing fields at the open-end edge of the microstrip patch. Several suggestions have been presented in the literature [1-29] to account for these fringing fields. A survey of the literature [1-29] clearly shows that the resonant frequency of a circular MSA for TM_{11} mode strongly depends on r_o , h , and ϵ_r . Therefore, the effect of the size of the dielectric substrate is not considered in calculating the resonant frequency. In this work, the resonant frequency of the circular MSA is computed by using a method based on the ANFIS. Only three parameters, r_o , h , and ϵ_r , are used in calculating the resonant frequency.

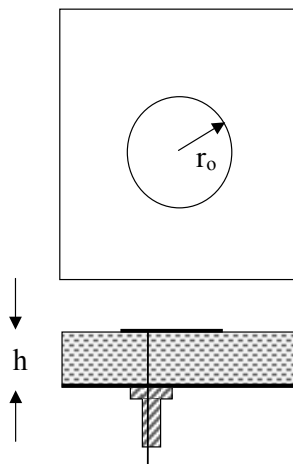


Fig. 1. Geometry of a circular microstrip antenna.

3. ADAPTIVE NEURO-FUZZY INFERENCE SYSTEM (ANFIS)

The ANFIS is a FIS implemented in the framework of an adaptive fuzzy neural network, and is a very powerful approach for building complex and nonlinear relationship between a set of input and output data [30], [31]. It combines the explicit knowledge representation of FIS with the learning power of ANNs. Usually, the transformation of human knowledge into a fuzzy system (in the form of rules and membership functions) does not give exactly the target response. So, the optimum values of the FIS parameters should be found. The main objective of the ANFIS is to determine the optimum values of the equivalent FIS parameters by applying a learning algorithm using input-output data sets. The parameter optimization is done in such a way that the error between the target and the actual output is minimized.

The ANFIS architecture consists of fuzzy layer, product layer, normalized layer, de-fuzzy layer, and summation layer. A typical ANFIS architecture is shown in Figure 2, in which a circle indicates a fixed node, whereas a square indicates an adaptive node. For simplicity, we assume that the FIS under consideration has two inputs x and y and one output z . The ANFIS used in this work implements a first-order Sugeno fuzzy model. Among many FIS models, the Sugeno fuzzy model is the most widely applied one for its high interpretability and computational efficiency, and built-in optimal and adaptive techniques. For a first-order Sugeno fuzzy model, a common rule set with two fuzzy if-then rules can be expressed as

Rule 1: If x is A_1 and y is B_1 , then $z_1 = p_1x + q_1y + r_1$ (2a)

Rule 2: If x is A_2 and y is B_2 , then $z_2 = p_2x + q_2y + r_2$ (2b)

where A_i and B_i are the fuzzy sets in the antecedent, and p_i , q_i , and r_i are the design parameters that are determined during the training process. As in Figure 2, the ANFIS consists of five layers:

Layer 1: Every node i in this layer is an adaptive node with a node function:

$$O_i^1 = \mu_{A_i}(x), \quad i = 1, 2 \quad (3a)$$

$$O_i^1 = \mu_{B_{i-2}}(y), \quad i = 3, 4 \quad (3b)$$

where x (or y) is the input of node i . $\mu_{A_i}(x)$ and $\mu_{B_{i-2}}(y)$ can adopt any fuzzy membership function (MF). In general, the types of the MFs are determined by trial-and-error method and/or operator's experience. After this determination, the parameters of MFs and the number of fuzzy rules can be optimally obtained by using optimization techniques.

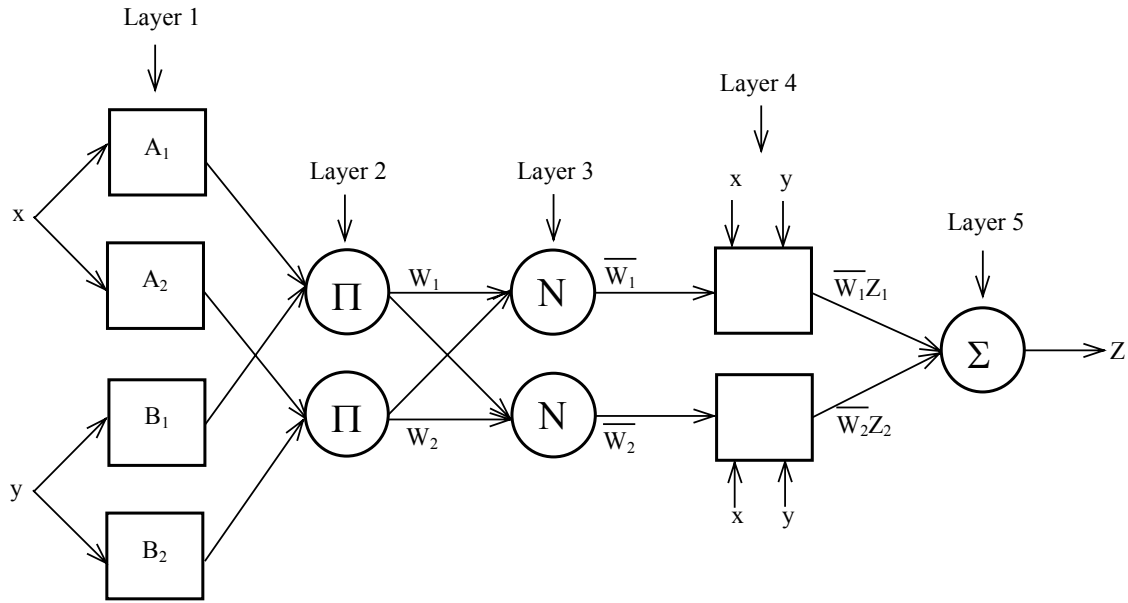


Fig. 2. Architecture of ANFIS.

In this paper, the following MFs are obtained by using trial-and-error methods:

- i) Gaussian MFs

$$gaussian(x; c, \sigma) = e^{-\frac{1}{2} \left(\frac{x-c}{\sigma} \right)^2} \quad (4a)$$

- ii) Triangular MFs

$$triangle(x; a, b, c) = \begin{cases} 0, & x \leq a \\ \frac{x-a}{b-a}, & a \leq x \leq b \\ \frac{c-x}{c-b}, & b \leq x \leq c \\ 0, & c \leq x \end{cases} \quad (4b)$$

where \$\{a_i, b_i, c_i, \sigma_i\}\$ is the parameter set that changes the shape of the MF. Parameters in this layer are named *the premise parameters*.

Layer 2: Every node in this layer is a fixed node labeled \$\Pi\$, which multiplies the incoming signals and outputs the product:

$$O_i^2 = \omega_i = \mu_{A_i}(x) \mu_{B_i}(y), \quad i = 1, 2 \quad (5)$$

Each node output represents the firing strength of a rule.

Layer 3: Every node in this layer is a fixed node labeled \$N\$. The \$i\$th node calculates the ratio of the \$i\$th rule's firing strength to the sum of all rules' firing strengths:

$$O_i^3 = \bar{\omega}_i = \frac{\omega_i}{\omega_1 + \omega_2}, \quad i = 1, 2 \quad (6)$$

where \$\bar{\omega}_i\$ is referred to as *the normalized firing strength*.

Layer 4: Every node \$i\$ in this layer is an adaptive node with a node function:

$$O_i^4 = \bar{\omega}_i z_i = \bar{\omega}_i (p_i x + q_i y + r_i), \quad i = 1, 2 \quad (7)$$

where \$\bar{\omega}_i\$ is the output of layer 3, and \$\{p_i, q_i, r_i\}\$ is the parameter set. Parameters in this layer are referred to as *the consequent parameters*.

Layer 5: The single node in this layer is a fixed node labeled \$\Sigma\$, which computes the overall output as the summation of all incoming signals:

$$O_1^5 = \sum_{i=1}^2 \bar{\omega}_i z_i = \frac{\omega_1 z_1 + \omega_2 z_2}{\omega_1 + \omega_2}. \quad (8)$$

It can be seen from the ANFIS architecture that when the values of the premise parameters are fixed, the overall output can be expressed as a linear combination of the consequent parameters:

$$z = (\bar{\omega}_1 x) p_1 + (\bar{\omega}_1 y) q_1 + (\bar{\omega}_1) r_1 + (\bar{\omega}_2 x) p_2 + (\bar{\omega}_2 y) q_2 + (\bar{\omega}_2) r_2. \quad (9)$$

The optimal values of the consequent parameters can be found by using the least-squares method (LSM). When the premise parameters are not fixed, the search space becomes larger and the convergence of training becomes slower. The hybrid learning algorithm combining the LSM and the backpropagation (BP) algorithm [51] can be used to solve this problem. This algorithm converges much faster since it reduces the dimension of the search space of the BP algorithm. During the learning process, the premise parameters in layer 1 and the consequent parameters in layer 4 are tuned until the desired response of the FIS is achieved.

The hybrid learning algorithm has a two-step process. First, while holding the premise parameters fixed, the functional signals are propagated forward to layer 4, where the consequent parameters are identified by the LSM. Then the consequent parameters are held fixed while the error signals, the derivative of the error measure with respect to each node output, are propagated from the output end to the input end, and the premise parameters are updated by the standard BP algorithm. The weight of each input variable to output is also determined by utilizing the hybrid-learning algorithm.

4. ANFIS FOR RESONANT FREQUENCY COMPUTATION

In this paper, the ANFIS has been used to calculate the resonant frequencies of circular MSAs. For the ANFIS, the inputs are r_o , h , and ϵ_r , and the output is the measured resonant frequencies f_{me} . The ANFIS model used in computing the resonant frequencies is illustrated in Figure 3.

There are two types of data generators for antenna applications. These data generators are measurements and simulations. The selection of a data generator depends on the application and the availability of the data generator. The training and test data sets used in this paper have been obtained from the previous experimental works published in seven sources [6], [8], [11], [14-17], and are given in Table 1. The 17 data sets in Table 1 were used to

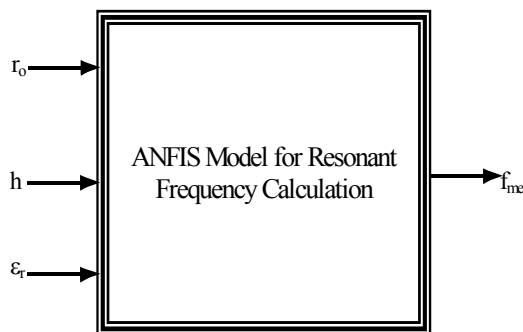


Fig. 3. ANFIS model for resonant frequency calculation.

Table 1. The measured resonant frequencies and the resonant frequencies obtained from the ANFIS proposed in this paper for circular microstrip antennas.

Patch No	r_o (cm)	h (cm)	ϵ_r	h/λ_d	Measured f_{me} (MHz)	Present ANFIS Method (MHz)
1	6.800	0.08000	2.32	0.003392	835 [□]	835
2*	6.800	0.15900	2.32	0.006692	829 [□]	832
3	6.800	0.31800	2.32	0.013159	815 [□]	815
4	5.000	0.15900	2.32	0.009106	1128 [△]	1128
5	3.800	0.15240	2.49	0.011567	1443 [▽]	1443
6	4.850	0.31800	2.52	0.018493	1099 [×]	1099
7	3.493	0.15880	2.50	0.013140	1570 [*]	1570
8	1.270	0.07940	2.59	0.017336	4070 [*]	4070
9	3.493	0.31750	2.50	0.025268	1510 [*]	1510
10	4.950	0.23500	4.55	0.013785	825	825
11	3.975	0.23500	4.55	0.017210	1030	1030
12*	2.990	0.23500	4.55	0.022724	1360	1360
13	2.000	0.23500	4.55	0.033468	2003	2003
14	1.040	0.23500	4.55	0.062659	3750	3750
15	0.770	0.23500	4.55	0.082626	4945	4945
16	1.150	0.15875	2.65	0.038118	4425 [†]	4425
17	1.070	0.15875	2.65	0.040684	4723 [†]	4723
18*	0.960	0.15875	2.65	0.045006	5224 [†]	5225
19	0.740	0.15875	2.65	0.057146	6634 [†]	6634
20	0.820	0.15875	2.65	0.052300	6074 [†]	6074

[□]These frequencies are measured by Dahele and Lee [14]; [△]this frequency is measured by Dahele and Lee [15]; [▽] this frequency is measured by Carver [11]; [×] this frequency is measured by Antoszkiewicz and Shafai [17]; ^{*}these frequencies are measured by Howell [8]; [†] these frequencies are measured by Itoh and Mittra [6]; the remainder are measured by Abboud et al. [16]. *Test data sets.

train the ANFIS. Three data sets, marked with an asterisk in Table 1, were used for testing. The values of electrical thickness, defined as h/λ_d where λ_d is the wavelength in the substrate, are also given in Table 1. The training and test data sets used in this paper are the same as those used for ANNs in [41], [47]. The antennas given in Table 1 vary in patch radius from 0.74 cm to 6.80 cm, and in physical thickness from 0.0794 cm to 0.318 cm, and operate over the frequency range 815 MHz - 6634 MHz.

Training an ANFIS by using the hybrid learning algorithm to calculate the resonant frequency involves presenting it sequentially with different sets (r_o, h, ϵ_r) and corresponding measured values f_{me} . Differences between the target output f_{me} and the actual output of the ANFIS are evaluated by the hybrid learning algorithm. The adaptation is carried out after the presentation of each set (r_o, h, ϵ_r) until the calculation accuracy of the ANFIS is deemed satisfactory according to some criterion (for example, when the error between f_{me} and the actual output for all the training sets falls below a given threshold) or when the maximum allowable number of epochs is reached.

The number of epochs was 100 for training. The number of MFs for the input variables r_o , h , and ϵ_r are 8, 2, and 6, respectively. The number of rules is then 96 ($8 \times 2 \times 6 = 96$). The type of MF is gaussian for r_o and triangular for h and ϵ_r . It is clear from eq. (4) that the gaussian and triangular MFs are specified by two and three parameters, respectively. Therefore, the ANFIS used here contains a total of 424 fitting parameters, of which 40 ($8 \times 2 + 2 \times 3 + 6 \times 3 = 40$) are the premise parameters and 384 ($4 \times 96 = 384$) are the consequent parameters.

5. RESULTS AND CONCLUSIONS

The resonant frequencies computed by using ANFIS presented in this paper for different circular MSAs are listed in Table 1. For comparison, the results obtained by using the conventional methods [8], [10], [11], [16], [18-21], [24-27] and by using the neural models [41, 47] based on the multilayered perceptrons and the radial basis function networks are given in Tables 2 and 3, respectively. BP, EDBD, DBD, QP, DRS, GA, and RBFN in Table 3 represent, respectively, the resonant frequencies calculated by using multilayered perceptrons trained by backpropagation (BP) [51], extended delta-bar-delta (EDBD) [52], delta-bar-delta (DBD) [53], quick propagation (QP) [54], directed random search (DRS) [55], and genetic algorithms (GA) [56], [57], and calculated by using the radial basis function network (RBFN) [58-60] trained by EDBD algorithm. The sum of the absolute errors between the theoretical and experimental results in Tables 1, 2, and 3 for every method is also listed in Table 4.

In Table 2, the results of Carver [11] were obtained by using the modal expansion technique. The formula based on the cavity model with a perfect magnetic wall was used by Howell [8]. The accuracy of the cavity model can be improved by taking modal and fringing field effects into consideration. In [10], the results were determined from the combination of the effective patch radius formula suggested by Shen et al. [9] and the relative dielectric constant. Abboud et al. [16] computed the resonant frequencies by using the dynamic permittivity constant expression presented by Wolff and Knoppik [7] and the effective patch radius expression derived from the static fringing capacitance formula presented by Chew and Kong [12].

The resonant frequency can be obtained rigorously using the vector Hankel transform method [13] in terms of vector dual integral equations. This method is mathematically complex and requires high performance large-scale computer resources and a very large number of computations. For this reason, Liu and Chew [18] proposed a Fortran program of curve-fitting formula for the resonant frequency. This formula was obtained by using a database built by Galerkin's method, based on the formulation by Chew and Kong [13]. Close agreement was obtained

between the results of the curve-fitting formula and the results of Galerkin's method. However, the results of the curve-fitting formula are not in very good agreement with the experimental results, as shown in Tables 2 and 4.

Roy and Jecko [19] calculated the resonant frequencies by using a curve-fitting formula based on the computed data of existing theory. For this formula, it is not necessary to compute the zeros of the derivative of the Bessel function, however, it is clear from Tables 2 and 4 that the results obtained from the formula are not in very good agreement with the experimental results. The results of Güney [20] were determined by using the effective values for both the patch radius and the substrate permittivity.

The moment-method is one of the most widely used methods in analyzing the performance of MSAs. This method is not practical as a quick antenna design aid because its computational cost is high due to the evaluation of the slowly decaying integrals and the iterative nature of the solution process. Because of this problem, Lee and Fan [21] presented the curve-fitting formulas based on the moment-method results. These relatively simple formulas allow designers to calculate the resonant frequencies for a given design without having to develop or run the moment-method code themselves. It was shown in [21] that the resonant frequencies predicted by the curve-fitting formulas agree well with the moment-method results. However, it is apparent from Tables 2 and 4 that the results of these formulas are not in very good agreement with the experimental results.

In [24], [25], the simple effective patch radius expressions obtained from the tabu search and genetic algorithms have been presented for calculating the resonant frequency. The tabu search and genetic algorithms were used to determine optimally the unknown coefficient values of the models chosen for the effective patch radius expressions.

Gürel and Yazgan [26] computed the resonant frequencies by using an effective patch radius expression combined with the proper effective permittivity formula. In order to improve the accuracy of the calculations in [26], a modified dynamic permittivity formula was also used by Gürel and Yazgan [27].

It can be clearly seen from Tables 2 and 4 that the conventional methods give comparable results. Some cases are in good agreement with measurements, and others are far off. The best result among conventional methods is obtained from the formulas proposed by Akdagli and Güney [25].

As it is seen from Tables 2, 3, and 4, the results of all neural models are better than those predicted by the conventional methods. These results clearly show the superiority of ANNs over the conventional methods. When the performances of neural models presented in [41], [47] are compared with each other, the highest accuracy was achieved with the ANN trained by the EDBD algorithm.

Table 2. Resonant frequencies obtained from conventional methods available in the literature [8, 10, 11, 16, 18-21, 24-27] for circular microstrip antennas.

Patch No	Measured f_{me} (MHz)	Conventional Methods in the Literature											
		[11]	[8]	[10]	[16]	[18]	[19]	[20]	[21]	[24]	[25]	[26]	[27]
1	835	845	849	840	842	844	838	841	840	843	840	842	839
2	829	842	849	833	837	839	831	836	832	838	831	837	833
3	815	834	849	821	826	829	819	826	818	828	815	827	824
4	1128	1141	1154	1127	1133	1136	1124	1132	1125	1135	1123	1133	1129
5	1443	1445	1466	1427	1436	1439	1423	1435	1423	1438	1432	1436	1431
6	1099	1115	1142	1098	1105	1109	1095	1105	1091	1107	1100	1107	1103
7	1570	1565	1580	1545	1555	1559	1541	1554	1539	1558	1550	1556	1550
8	4070	4203	4290	4145	4175	4187	4134	4173	4120	4183	4168	4179	4163
9	1510	1539	1580	1513	1522	1529	1509	1523	1498	1524	1510	1525	1520
10	825	818	833	818	827	827	816	825	817	824	823	827	823
11	1030	1014	1037	1016	1027	1027	1013	1026	1013	1024	1022	1028	1023
12	1360	1339	1379	1344	1358	1360	1340	1359	1336	1355	1352	1361	1355
13	2003	1972	2061	1990	2009	2012	1984	2012	1966	2007	2002	2015	2009
14	3750	3627	3963	3749	3744	3737	3739	3752	3634	3750	3750	3750	3751
15	4945	4722	5353	5001	4938	4922	4987	4943	4817	4948	4945	4932	4944
16	4425	4461	4695	4399	4413	4437	4388	4422	4328	4422	4413	4423	4415
17	4723	4776	5046	4712	4723	4749	4699	4731	4630	4730	4722	4733	4725
18	5224	5289	5625	5223	5226	5257	5209	5237	5121	5231	5224	5237	5231
19	6634	6733	7297	6679	6644	6684	6661	6658	6499	6634	6636	6652	6651
20	6074	6125	6585	6063	6047	6084	6046	6061	5920	6046	6043	6057	6054

Table 3. Resonant frequencies obtained by using artificial neural networks (ANNs) presented in [41, 47] for circular microstrip antennas.

Patch No	Measured f_{me} (MHz)	Artificial Neural Networks (ANNs) [41, 47]						
		BP	EDBD	DBD	QP	DRS	GA	RBFN
1	835	835	835	835	835	835	930	835
2	829	828	828	828	828	828	932	812
3	815	815	815	815	815	815	816	815
4	1128	1128	1128	1128	1126	1126	944	1129
5	1443	1443	1443	1443	1446	1443	1435	1440
6	1099	1099	1099	1099	1100	1098	1081	1099
7	1570	1570	1570	1570	1568	1572	1582	1572
8	4070	4070	4070	4070	4070	4070	4028	4070
9	1510	1510	1510	1510	1509	1510	1516	1510
10	825	825	825	825	826	828	885	826
11	1030	1030	1030	1030	1029	1024	1013	1029
12	1360	1361	1361	1364	1357	1362	1198	1399
13	2003	2003	2003	2003	2003	2007	1996	2004
14	3750	3750	3750	3750	3750	3747	3751	3749
15	4945	4945	4945	4945	4945	4947	4943	4946
16	4425	4425	4428	4425	4426	4413	4471	4427
17	4723	4723	4720	4723	4721	4732	4690	4719
18	5224	5233	5224	5232	5225	5261	5184	5230
19	6634	6634	6634	6634	6633	6617	6632	6630
20	6074	6074	6075	6074	6075	6094	6078	6080

Table 4. Sum of absolute errors between measured and calculated resonant frequencies.

Methods		Total absolute deviations from the measured data (MHz)
ANFIS	Present Method	4
Conventional Methods in the Literature	[11]	965
	[8]	3341
	[10]	337
	[16]	253
	[18]	383
	[19]	380
	[20]	253
	[21]	1047
	[24]	253
	[25]	207
Artificial Neural Networks (ANNs) [41, 47]	[26]	275
	[27]	235
	BP	11
	EDBD	9
	DBD	13
	QP	21
	DRS	224
	GA	892
	RBFN	89

It is evident from Tables 1-4 that the results of ANFIS show better agreement with the experimental results as compared to the results of the conventional methods [8], [10], [11], [16], [18-21], [24-27] and the ANN models [41], [47]. The excellent agreement between the experimental results and our computed resonant frequency results supports the validity of the ANFIS model proposed in this paper.

For accurately computing the various parameters of complicated antenna structures, the ANFIS can be used but it should be trained by using appropriate training data sets. The training data sets should contain desired input/output data pairs of the target antenna to be modeled. A prominent advantage of the ANFIS model is that, after proper training, ANFIS completely bypasses the repeated use of complex iterative processes for new cases presented to it. Even if training takes a few minutes, the test process takes only a few microseconds to produce the resonant frequency. ANFIS are also less susceptible to the noise inherent in measured data and antenna imperfections [61].

In the last decade, ANNs have been widely used to solve antenna and electromagnetic engineering problems as a fast, accurate, and flexible method [62], [63]. However, better results can be obtained by using the ANFIS in solving these problems because the ANFIS is a very effective modeling scheme combining the benefits of both ANNs and FISs in a single model. We expect that the ANFIS will find a

wide application area in antenna and electromagnetic engineering as ANNs did.

In this study, the ANFIS is trained and tested with the experimental data taken from the previous experimental works [6], [8], [11], [14-17]. It is apparent from Tables 2 and 4 that the theoretical resonant frequency results of the conventional methods are not in very good agreement with the experimental results. For this reason, the theoretical data sets obtained from the conventional methods are not used in this work. Only the measured data set is used for training and testing the ANFIS. It also needs to be emphasized that better results may be obtained from the ANFIS either by choosing different training and test data sets from the ones used in the paper or by supplying more input data set values for training.

In this paper, only the lowest resonant frequency f_{11} for the TM_{11} mode is calculated by using the ANFIS because this circular microstrip patch mode is widely used in MSA applications. However, the ANFIS can be easily adapted to compute the resonant frequencies of higher-order modes of practical interest if the data sets for these modes are available. It must also be emphasized that the proposed ANFIS method is not limited to the resonant frequency calculation of circular MSAs. This method can be easily applied to other antenna and microwave engineering problems. Accurate, fast, and reliable ANFIS models can be developed from measured/simulated antenna data. Once developed, these ANFIS models can be used in place of computationally intensive numerical models to speed up antenna design.

As a result, the ANFIS trained by means of the measured data is presented to calculate accurately the resonant frequency of circular MSAs with substrates with $2.32 \leq \epsilon_r \leq 4.55$ and $0.0794 \text{ cm} \leq h \leq 0.318 \text{ cm}$. A hybrid learning algorithm is used to optimize the parameters of ANFIS. The results of ANFIS are in excellent agreement with the measurements, and better accuracy with respect to the previous conventional methods and neural models is obtained. The ANFIS offers an accurate and efficient alternative to previous methods for the calculation of the resonant frequencies.

REFERENCES

- [1] I. J. Bahl and P. Bhartia, *Microstrip Antennas*, Artech House, Dedham, MA, 1980.
- [2] K. C. Gupta and A. Benalla (Eds.), *Microstrip Antenna Design*, Artech House, Canton, MA, 1988.
- [3] J. R. James and P. S. Hall, *Handbook of Microstrip Antennas*, IEE Electromagnetic Wave Series, Peter Peregrinus Ltd., London, Vols. 1 and 2, No. 28, 1989.

- [4] D. M. Pozar and D. H. Schaubert (Eds.), *Microstrip Antennas-The Analysis and Design of Microstrip Antennas and Arrays*, IEEE Press, New York, 1995.
- [5] R. Garg, P. Bhartia, I. Bahl, and A. Ittipiboon, *Microstrip Antenna Design Handbook*, Artech House, Canton, MA, 2001.
- [6] T. Itoh and R. Mittra, "Analysis of a Microstrip Disk Resonator," *AEU-International Journal of Electronics and Communications*, Vol. 27, pp. 456-458, 1973.
- [7] I. Wolff and N. Knoppik, "Rectangular and Circular Microstrip Disk Capacitors and Resonators," *IEEE Trans. Microwave Theory Technology*, Vol. MTT-22, pp. 857-864, 1974.
- [8] J. Q. Howell, "Microstrip Antennas," *IEEE Trans. Ant. Propagat.*, Vol. AP-23, pp. 90-93, 1975.
- [9] L. C. Shen, S. A. Long, M. R. Allerding, and M. D. Walton, "Resonant Frequency of a Circular Disc, Printed-Circuit Antenna," *IEEE Trans. Ant. Propagat.*, Vol. AP-25, pp. 595-596, 1977.
- [10] A. G. Derneryd, "Analysis of the Microstrip Disk Antenna Element," *IEEE Trans. Ant. Propagat.*, Vol. AP-27, pp. 660-664, 1979.
- [11] K. R. Carver, "Practical Analytical Techniques for the Microstrip Antenna," *Proc. Workshop Printed Circuit Antenna Technology*, Las Cruces, New Mexico, pp. 7.1-7.20, 1979.
- [12] W. C. Chew and J. A. Kong, "Effects of Fringing Fields on the Capacitance of Circular Microstrip Disk," *IEEE Trans. Microwave Theory Technology*, Vol. MTT-28, pp. 98-104, 1980.
- [13] W. C. Chew and J. A. Kong, "Resonance of Axial and Non-Axial Symmetric Modes in Circular Microstrip Disk Antenna," *IEEE AP-S Int. Symp. Dig.*, Quebec, Canada, pp. 621-625, 1980.
- [14] J. S. Dahele and K. F. Lee, "Effect of Substrate Thickness on the Performance of a Circular-Disk Microstrip Antenna," *IEEE Trans. Ant. Propagat.*, Vol. AP-31, pp. 358-364, 1983.
- [15] J. S. Dahele and K. F. Lee, "Theory and Experiment on Microstrip Antennas with Airgaps," *IEE Proc. Pt. H.*, Vol. 132, pp. 455-460, 1985.
- [16] F. Abboud, J. P. Damiano, and A. Papiernik, "New Determination of Resonant Frequency of Circular Disc Microstrip Antenna: Application to Thick Substrate," *Electronics Letters*, Vol. 24, pp. 1104-1106, 1988.
- [17] K. Antoszkiewicz and L. Shafai, "Impedance Characteristics of Circular Microstrip Patches," *IEEE Trans. Ant. Propagat.*, Vol. AP-38, pp. 942-946, 1990.
- [18] Q. Liu and W. C. Chew, "Curve-Fitting Formulas for Fast Determination of Accurate Resonant Frequency of Circular Microstrip Patches," *IEE Proc. Pt. H.*, Vol. 135, pp. 289-292, 1988.
- [19] J. S. Roy and B. Jecko, "A Formula for the Resonance Frequencies of Circular Microstrip Patch Antennas Satisfying CAD Requirements," *International Journal of Microwave and Millimeter-Wave Computer-Aided Engineering*, Vol. 3, pp. 67-70, 1993.
- [20] K. Guney, "Resonant Frequency of Electrically-Thick Circular Microstrip Antennas," *International Journal of Electronics*, Vol. 77, pp. 377-386, 1994.
- [21] K. F. Lee and Z. Fan, "CAD Formulas for Resonant Frequencies of TM_{11} Mode of Circular Patch Antenna with or without Superstrate," *Microwave and Optical Technology Letters*, Vol. 7, pp. 570-573, 1994.
- [22] P. Mythili and A. Das, "Simple Approach to Determine Resonant Frequencies of Microstrip Antennas," *IEE Proc. Pt. H.*, Vol. 145, pp. 159-162, 1998.
- [23] K. P. Ray and G. Kumar, "Determination of the Resonant Frequency of Microstrip Antennas," *Microwave and Optical Technology Letters*, Vol. 23, pp. 114-117, 1999.
- [24] N. Karaboga, K. Guney, and A. Akdagli, "A New Effective Patch Radius Expression Obtained by Using a Modified Tabu Search Algorithm for the Resonant Frequency of Electrically Thick Circular Microstrip Antenna," *International Journal of Electronics*, Vol. 86, pp. 825-835, 1999.
- [25] A. Akdagli and K. Guney, "Effective Patch Radius Expression Obtained Using a Genetic Algorithm for the Resonant Frequency of Electrically Thin and Thick Circular Microstrip Antennas," *IEE Proc. Pt. H.*, Vol. 147, pp. 156-159, 2000.
- [26] C. S. Gurel and E. Yazgan, "Resonant Frequency of an Air Gap Tuned Circular Disc Microstrip Antenna," *International Journal of Electronics*, Vol. 87, pp. 973-979, 2000.
- [27] C.S. Gurel and E. Yazgan, "New Determination of Dynamic Permittivity and Resonant Frequency of Tunable Circular Disk Microstrip Structures," *International Journal of RF and Microwave Computer-Aided Engineering*, Vol. 10, pp. 120-126, 2000.
- [28] D. Guha, "Resonant Frequency of Circular Microstrip Antennas with and without Air Gaps," *IEEE Trans. Ant. Propagat.*, Vol. AP-49, pp. 55-59, 2001.
- [29] A. K. Verma and Nasimuddin, "Analysis of Circular Microstrip Antennas on Low- and High-Relative-Permittivity Substrates," *Microwave and Optical Technology Letters*, Vol. 34, pp. 75-80, 2002.
- [30] J.-S.R. Jang, "ANFIS: Adaptive-Network-Based Fuzzy Inference System," *IEEE Trans. Systems Man and Cybernetics*, Vol. 23, pp. 665-685, 1993.

- [31] J.-S.R. Jang, C. T. Sun, and E. Mizutani, *Neuro-Fuzzy and Soft Computing: A Computational Approach to Learning and Machine Intelligence*, Prentice-Hall, Upper Saddle River, NJ, 1997.
- [32] V. A. Constantin, *Fuzzy Logic and Neuro-Fuzzy Applications Explained*, Prentice-Hall, Englewood Cliffs, NJ, 1995.
- [33] C. T. Lin and C. S. G. Lee, *Neural Fuzzy Systems: A Neuro-Fuzzy Synergism to Intelligent Systems*, Prentice-Hall, Upper Saddle River, NJ, 1996.
- [34] J. Kim and N. Kasabov, "HyFIS: Adaptive Neuro-Fuzzy Inference Systems and Their Application to Nonlinear Dynamical Systems," *Neural Networks*, Vol. 12, pp. 1301-1319, 1999.
- [35] K. Güney and N. Sarıkaya, "Computation of Resonant Frequency for Equilateral Triangular Microstrip Antennas with the Use of Adaptive Neuro-Fuzzy Inference System," *International Journal of RF and Microwave Computer-Aided Engineering*, Vol. 14, pp. 134-143, 2004.
- [36] K. Güney and N. Sarıkaya, "Adaptive Neuro-Fuzzy Inference System for the Input Resistance Computation of Rectangular Microstrip Antennas with Thin and Thick Substrates," *Journal of Electromagnetic Waves and Applications (JEWA)*, Vol. 18, pp. 23-39, 2004.
- [37] K. Güney and N. Sarıkaya, "Input Resistance Calculation for Circular Microstrip Antennas Using Adaptive Neuro-Fuzzy Inference System," *International Journal of Infrared and Millimeter Waves*, Vol. 25, pp. 703-716, 2004.
- [38] S. Ozer, K. Güney, and A. Kaplan, "Computation of the Resonant Frequency of Electrically Thin and Thick Rectangular Microstrip Antennas with the Use of Fuzzy Inference Systems," *International Journal of RF and Microwave Computer-Aided Engineering*, Vol. 10, pp. 108-119, 2000.
- [39] A. Kaplan, K. Güney, and S. Ozer, "Fuzzy Associative Memories for the Computation of The Bandwidth of Rectangular Microstrip Antennas with Thin and Thick Substrates," *International Journal of Electronics*, Vol. 88, pp. 189-195, 2001.
- [40] S. Sagirolu and K. Güney, "Calculation of Resonant Frequency for an Equilateral Triangular Microstrip Antenna with the Use of Artificial Neural Networks," *Microwave and Optical Technology Letters*, Vol.14, pp. 89-93, 1997.
- [41] S. Sagirolu, K. Güney, and M. Erler, "Resonant Frequency Calculation for Circular Microstrip Antennas Using Artificial Neural Networks," *International Journal of RF and Microwave Computer-Aided Engineering*, Vol. 8, pp. 270-277, 1998.
- [42] S. Sagirolu, K. Güney, and M. Erler, "Calculation of Bandwidth for Electrically Thin and Thick Rectangular Microstrip Antennas with the Use of Multilayered Perceptrons," *International Journal of RF and Microwave Computer-Aided Engineering* (Special Issue: Applications of Artificial Neural Networks to RF and Microwave Design), Vol. 9, pp. 277-286, 1999.
- [43] D. Karaboga, K. Güney, S. Sagirolu, and M. Erler, "Neural Computation of Resonant Frequency of Electrically Thin and Thick Rectangular Microstrip Antennas," *IEE. Proc. Pt. H.*, Vol. 146, pp. 155-159, 1999.
- [44] K. Güney, M. Erler, and S. Sagirolu, "Artificial Neural Networks for the Resonant Resistance Calculation of Electrically Thin and Thick Rectangular Microstrip Antennas," *Electromagnetics*, Vol. 20, pp. 387-400, 2000.
- [45] K. Güney, S. Sagirolu, and M. Erler, "Comparison of Neural Networks for Resonant Frequency Computation of Electrically Thin and Thick Rectangular Microstrip Antennas," *Journal of Electromagnetic Waves and Applications (JEWA)*, Vol. 15, pp. 1121-1145, 2001.
- [46] K. Güney, S. Sagirolu, and M. Erler, "Generalized Neural Method to Determine Resonant Frequencies of Various Microstrip Antennas," *International Journal of RF and Microwave Computer-Aided Engineering* (Special Issue: Applications of Artificial Neural Networks to RF and Microwave Design), Vol. 12, pp. 131-139, 2002.
- [47] C. Yildiz, S. S. Gultekin, K. Güney, and S. Sagirolu, "Neural Models for the Resonant Frequency of Electrically Thin and Thick Circular Microstrip Antennas and the Characteristic Parameters of Asymmetric Coplanar Waveguides Backed with a Conductor," *AEU-International Journal of Electronics and Communications*, Vol. 56, pp. 396-406, 2002.
- [48] K. Güney, S. Sagirolu, and M. Erler, "Design of Rectangular Microstrip Antennas with the Use of Artificial Neural Networks," *Neural Network World*, Vol. 4, pp. 361-370, 2002.
- [49] K. Güney and N. Sarıkaya, "Artificial Neural Networks for Calculating the Input Resistance of Circular Microstrip Antennas," *Microwave and Optical Technology Letters*, Vol. 37, pp. 107-111, 2003.
- [50] K. Güney and N. Sarıkaya, "Artificial Neural Networks for the Narrow Aperture Dimension Calculation of Optimum Gain Pyramidal Horns," *Electrical Engineering*, Vol. 86, pp. 157-163, 2004.
- [51] D. E. Rumelhart and J. L. McClelland, *Parallel Distributed Processing*, Vol.1, The MIT Press, Cambridge, 1986.
- [52] A. A. Minai and R. D. Williams, "Acceleration of Backpropagation Through Learning Rate and Momentum Adaptation," *International Joint*

Conference on Neural Networks, Vol. 1, pp. 676-679, 1990.

- [53] R. A. Jacobs, "Increased Rate of Convergence Through Learning Rate Adaptation," *Neural Networks*, Vol. 1, pp. 295-307, 1988.
- [54] S. E. Fahlman, "Fast Learning Variations on Back Propagation: An Empirical Study," In D. S. Touretzky, G. E. Hinton and T. J. Sejnowski (Eds.), *Proc. of the 1988 Connectionist Models Summer School*, San Mateo, CA, Morgan Kaufmann, pp. 38-51, 1988.
- [55] J. Matyas, "Random Optimization," *Automation and Remote Control*, Vol. 26, pp. 246-253, 1965.
- [56] J. H. Holland, *Adaptation in Natural and Artificial Systems*, The University of Michigan Press, Ann Arbor, MI, 1975.
- [57] L. Davis, *Handbook of Genetic Algorithms*, Van Nostrand Reinhold, NY, 1991.
- [58] D. S. Broomhead and D. Lowe, "Multivariable Functional Interpolation and Adaptive Networks," *Complex Systems*, Vol. 2, pp. 321-355, 1988.
- [59] J. Moody and C. Darken, "Fast-Learning in Networks of Locally-Tuned Processing Units," *Neural Computation*, Vol. 1, pp. 281-294, 1989.
- [60] S. Chen, C. F. N. Cowan and P. M. Grant, "Orthogonal Least Squares Learning Algorithm for Radial Basis Function Networks," *IEEE Trans. Neural Networks*, Vol. 4, pp. 302-309, 1991.
- [61] E. Bokshtein, D. Shmaltz, O. Herbst, H. Bunke and A. Kandel, "Monopulse Amplitude Direction-Finding Using Neuro-Fuzzy Approach," *Robotics and Autonomous Systems*, Vol. 33, pp. 125-134, 2000.
- [62] Q. J. Zhang and K. C. Gupta, *Neural Networks for RF and Microwave Design*, Artech House, Boston, MA, 2000.
- [63] C. G. Christodoulou and M. Georgiopoulos, *Application of Neural Networks in Electromagnetics*, Artech House, MA, 2001.



Kerim Guney was born in Isparta, Turkey, on February 28, 1962. He received the B.S. degree from Erciyes University, Kayseri, in 1983, the M.S. degree from Istanbul Technical University, in 1988, and the Ph.D. degree from Erciyes University, in 1991, all in electronics engineering. From 1991 to 1995 he was an assistant professor and now is a professor at the Department of Electronics Engineering, Erciyes University, where he is working in the areas of optimization techniques

(the genetic, the tabu search, the differential evolution, and the ant colony optimization algorithms), fuzzy inference systems, neural networks, their applications to antennas, microstrip and horn antennas, and antenna pattern synthesis. He has published more than 170 journal and conference papers.



Nurcan Sarikaya was born in Kayseri, Turkey, on October 04, 1978. She received the B.S. degree from Erciyes University, Kayseri, in 2001, and the M.S. degree from Erciyes University, in 2003, both in electronics engineering. Currently, she is a Ph.D. student and research assistant at the Department of Aircraft Electrical and Electronics of Civil Aviation School, Erciyes University. Her current research activities include neural networks, fuzzy inference systems, and their applications to antennas.

MODELISATION OF PROBE FEED EXCITATION USING ITERATIVE METHOD

H. Zairi*, A. Gharsallah*, A. Gharbi*, H. Baudrand**

* Department of Physics, Faculty of Sciences of Tunis

2092 El Manar Tunisia, e-mail: Ali.gharsallah@fst.rnu.tn

** ENSEEIHT, Toulouse, France

ABSTRACT

This paper presents an implementation of an iterative method based on the waves concept for analyzing patch antennas fed by coaxial probes. This method includes a two-dimensional fast Fourier transform (FFT-2D) in a wave guide environment. The method has the advantage of simplicity in that it does not involve basis functions and inversion of matrices, as used in other calculation methods. Therefore, it is capable of analyzing larger bodies than other classical techniques. An implementation of the iterative calculation is shown for the extraction of S parameters of microwave components and antennas. The good agreement between simulation results and experimental published data justifies the design procedure and validates the present analysis approach.

INDEX TERMS : Iterative method, fast Fourier transform in waveguide environment, probe feed.

I- INTRODUCTION

Microstrip patch antennas are widely used in wireless communication because of their advantages, such as being low profile, light weight, and conformal. Different numerical electromagnetic analysis techniques such as the method of moments [1], the finite elements method [2], and the finite difference time domain method can be used to accurately simulate the microstrip antenna [3]. In most cases those numerical techniques are not practical to use

directly in CAD software for design and optimisation purposes, due to the enormous amount of computer time required. Circuit simulators on the other hand are very fast. However, models of microwave integrated circuits used in circuit simulators are often inaccurate or even invariable. To overcome these difficulties, the use of the iterative method, which is based on the concept of waves, has been proposed. It consists of generating a recursive relationship between incident waves and reflected waves at the interface containing the circuit which is divided into cells [4]. A high computational speed has been achieved by using 2D fast Fourier Transform in wave-guide environment [5].

In this paper, a general implementation of the iterative method is proposed to treat microstrip patch antennas. The theory as well as its procedure implementation is described. The numerical results are compared to measured data [8] to establish the validity and usefulness of the iterative method given in this study.

II- GENERAL FORMULATION OF ITERATIVE METHOD

We consider the shielded microstrip circuit, assumed to be loss-less, presented in Fig. 1.

The air-dielectric interface π is divided into cells denoted by three sub-domains corresponding to metal, source and dielectric.

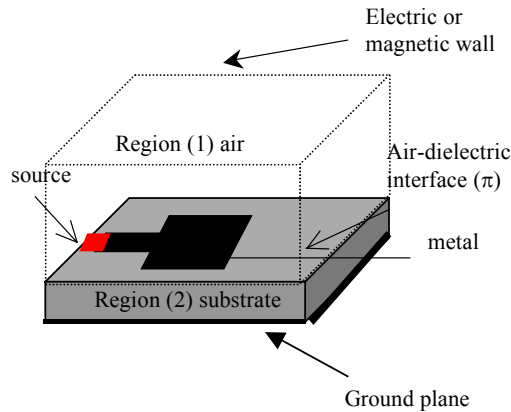


Figure 1. Typical planar circuit.

The wave concept is introduced by writing the transverse (plane π) electric field E_i and current density J_i in terms of incident and reflected waves [5]. It leads to the following set of equations:

$$\begin{cases} A_i = \frac{1}{2\sqrt{Z_{0i}}} (E_i + Z_{0i} J_i) \\ B_i = \frac{1}{2\sqrt{Z_{0i}}} (E_i - Z_{0i} J_i) \end{cases} \quad (1)$$

J_i is defined as follows:

$$J_i = H_i \times n, \quad n \text{ is oriented as the incident waves } A_i.$$

Z_{0i} is the characteristic impedance of the medium i ($i = 1, 2$). It is equal to:

$$Z_{0i} = \sqrt{\frac{\mu_0}{\epsilon_0 \epsilon_{ri}}}$$

In order to generate two waves, B_{ix} and B_{iy} , in the space domain, the structure is excited by an electric planar source. The model of the source is an electric field E_{oi} equivalent to a magnetic current density.

The Fast Fourier Transform (FFT-2D) in waveguide environment is then used to obtain two spectral waves B_i^{TE} and B_i^{TM} in each region. Then, these spectral waves are reflected in the spectral domain of the Region(1) and Region(2) as described in Fig. 2.

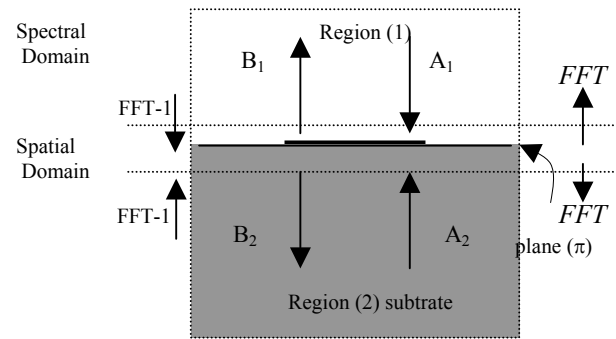


Figure 2. Definition of incident and diffracted waves.

The travelling part of these waves is then stored in memory, whereas the evanescent part constitutes the incident waves for the second iteration. The implementation of the iterative process consists of establishing a recursive relationship between waves (incident and reflected) at the q and $q-1$ iteration.

Initially, the interface circuit (plane π) on which the boundary conditions have to be satisfied (spatial domain) must be meshed.

Let us note H_d and H_m the indicator functions of respectively the dielectric and metal. These are equal to one in the considered domain and zero elsewhere. Due to the continuity relationship ($E_{t1}=E_{t2}$ and $J_{1+} + J_{2-}=0$ on the dielectric, $E_{t1}=E_{t2}=0$ on the metal) in each point of the discontinuity plane, it is easy to deduce from the equation (1) and (2) the following system:

$$\begin{bmatrix} B_1 \\ B_2 \end{bmatrix} = \begin{bmatrix} -H_m \frac{1-N_2}{1+N_2} H_d & \frac{2N}{1+N_2} H_d \\ \frac{2N}{1+N_2} H_d & -H_m \frac{1-N_2}{1+N_2} H_d \end{bmatrix} \begin{bmatrix} A_1 \\ A_2 \end{bmatrix} \quad (3)$$

Then the scattering matrix corresponding to the metal and dielectric domains can be expressed as follows:

$$\Gamma\pi = \begin{bmatrix} -H_m - \frac{1-N^2}{1+N^2} H_d & \frac{2N}{1+N^2} H_d \\ \frac{2N}{1+N^2} H_d & -H_m - \frac{1-N^2}{1+N^2} H_d \end{bmatrix}$$

$H_m=1$ on the source and 0 elsewhere.

$H_d=1$ on the source and 0 elsewhere.

$$N = \sqrt{\frac{Z_{o1}}{Z_{o2}}}$$

• Sub-domain of the source

There are numerous possibilities for choosing the source. The most simple consist in a realistic description of the excitation by a microstrip line (Fig.1).

This source generates two waves on both sides of the interface. The boundary condition on the source can be written as follows:

$$\begin{bmatrix} B_1 \\ B_2 \end{bmatrix} = \begin{bmatrix} -1 & 0 \\ 0 & -1 \end{bmatrix} \begin{bmatrix} A_1 \\ A_2 \end{bmatrix} + \begin{bmatrix} \frac{E_0}{\sqrt{Z_{o1}}} \\ \frac{E_0}{\sqrt{Z_{o2}}} \end{bmatrix}$$

$$E_1 = E_2 = E_0 - Z_0(J_1 + J_2).$$

Then the scattering matrix on the sub-domain source is expressed as

The drawback of this source is that we must use a box with electric walls to connect the source to the ground plane.

Another technique of spatial excitation is described in Section (III).

The waves B_i^α are reflected on the upper and lower parts of the structure. Consequently, in spectral domain the relation between waves become:

$$\begin{bmatrix} A_i^{TE} \\ A_i^{TM} \end{bmatrix} = \begin{bmatrix} \rho_i^{TE} & 0 \\ 0 & \rho_i^{TM} \end{bmatrix} \begin{bmatrix} B_i^{TE} \\ B_i^{TM} \end{bmatrix} \quad (4)$$

where the reflection coefficient in the dielectric substrate is:

$$\rho_i^\alpha = \frac{1 - Z_{oi}^\alpha Y_{mn,i}^\alpha \text{Coth}(\gamma_{m,n,i} h_i)}{1 + Z_{oi}^\alpha Y_{mn,i}^\alpha \text{Coth}(\gamma_{m,n,i} h_i)} \quad (i=2)$$

and the reflection coefficient in the free space (region 1) is:

$$\rho_i^\alpha = \frac{1 - Z_{oi}^\alpha Y_{mn,i}^\alpha}{1 + Z_{oi}^\alpha Y_{mn,i}^\alpha} \quad (i=1)$$

(α is TE or TM mode) with

$$Y^{TE} = \frac{\gamma_{mn,i}}{j\omega\mu_0}; \quad Y^{TM} = \frac{j\omega\epsilon_0\epsilon_r}{\gamma_{mn,i}}$$

where k_0 is the space wave number.

$$\gamma_{mn,i}^2 = \left[\frac{m\pi}{a} \right]^2 + \left[\frac{n\pi}{b} \right]^2 - k_0^2 \epsilon_r$$

III- MODELISATION OF PROBE FEED

The coaxial current probe offers a more realistic method to excite currents on a patch antenna [9]-[10]. The coaxial probe is connected through the ground plane with the centre conductor embedded vertically and terminated on the patch surface, where the outer conductor of the coax is connected to the ground plane. Figure 3 shows the attachment of the coaxial probe to the patch antenna surface.

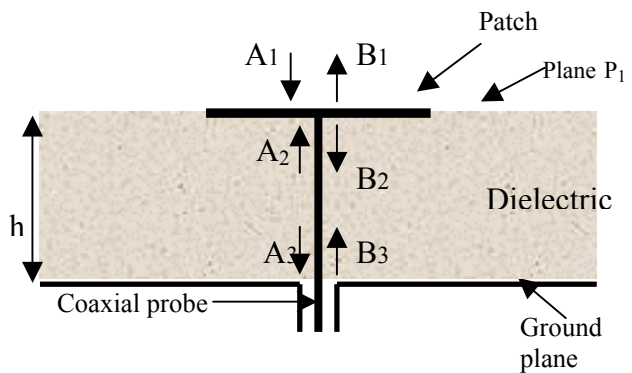


Figure 3. Microstrip patch antenna excited by coaxial probe feed.

The purpose is to determine the relationship between B_1, B_2 and A_1, A_2 on the sub-domain source.

We suppose that there are four metallic cells on the discontinuity plane (P_1) which are connected to the via hole. In this case the current density distribution is illustrated in Fig.4.

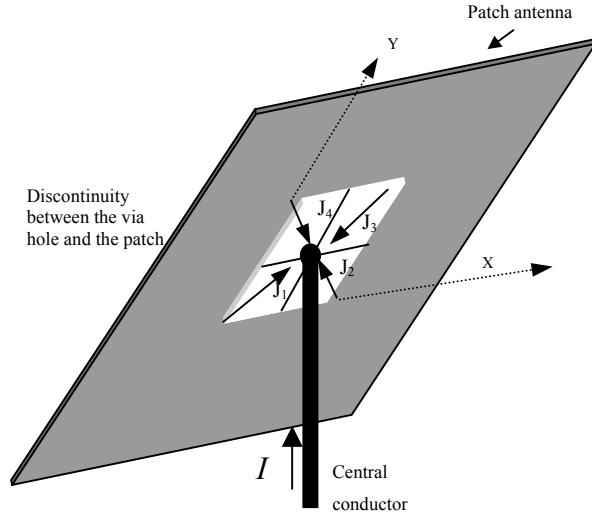


Figure 4. Bottom view of the patch antenna: Distribution of magnetic field on the discontinuity patch-via hole.

Let us note that I is the current excitation that verifies the following relationship:

$$J \times h = I \quad (5)$$

According to Fig.4, it is possible to establish the following relationship:

$$J_1 + J_2 + J_3 + J_4 = J \quad (6)$$

The vector J which characterizes the current distribution on the pixels of the discontinuity (via hole-patch) is given by:

$$J = \frac{1}{\sqrt{8}}(1, 1, -1, 1, -1, -1, 1, -1)_{(x,y)}^T \quad (7)$$

In order to modelize the discontinuity (via hole –plane P_1), we assume that only fundamental mode can be propagated in the via hole and the other modes are evanescent. The passage from four cells characterizing the current density J to modes and vice versa can be considered as multi-port network depicted in Fig. 5.

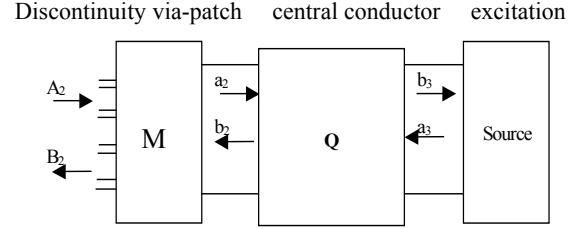


Figure 5. Coupling of Cells-Modes, Modes-Cells in the discontinuities between the via hole and the planes P_1, P_2 .

Q is a two-port network which characterizes the via hole, using the theory of transmission lines.

The scattering matrix of this two-port network is given by:

$$[S] = \begin{bmatrix} 0 & e^{j\theta} \\ e^{j\theta} & 0 \end{bmatrix}, \theta = k_0 h; k_0 = \frac{2\pi}{\lambda_0} \quad (8)$$

λ_0 : length wave in the free space.

Consequently, the relationship between waves $a_2, a_3, b_2,$ and $b_3,$ can be deduced:

$$\begin{bmatrix} b_2 \\ b_3 \end{bmatrix} = [S] \begin{bmatrix} a_2 \\ a_3 \end{bmatrix} \quad (8)$$

The expression of the matrix M characterizing the multi-port network is demonstrated in reference [6]. It is given by the following equation:

$$[M] = \begin{bmatrix} JJ^T & J \\ J^T & 0 \end{bmatrix}$$

Therefore, the relationship between incident and reflected waves is:

$$\begin{bmatrix} B_2 \\ a_2 \end{bmatrix} = \begin{bmatrix} JJ^T - 1 & J \\ J^T & 0 \end{bmatrix} \begin{bmatrix} A_2 \\ b_2 \end{bmatrix} \quad (9)$$

The source can be modeled by the equivalent circuit illustrated in Fig. 6.

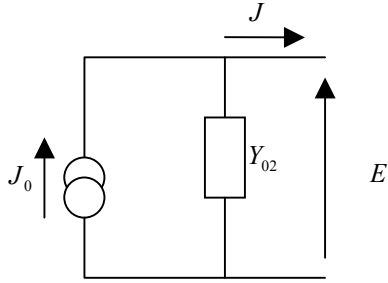


Figure 6. Equivalent circuit of the source.

As is known from the equivalent circuit given in fig.6, it is possible to deduce:

$$J = J_0 - Y_{02}E, \quad (10)$$

where Y_{02} is the admittance of Region (2),

$$Z_{02} = Y_{02}^{-1}.$$

Let us assume that the source excites the mode a_3 . However the magnitude of $b_3 = 0$. Using the equations (5) and (6) we deduce:

$$B_2 = (JJ^t - 1)A_2 + e^{j\theta} J a_3. \quad (11)$$

According to equations (7) and (11) we deduce:

$$a_3 = \frac{1}{2h} \sqrt{Z_{02}} I_0. \quad (12)$$

In the region (1), if we suppose that we have a metal domain, it is possible to establish: $B_1 = -A_1$.

According to the equations (11) and (12), we can deduce the relationship between incident and diffracted waves on the sub-domain source:

$$\begin{bmatrix} B_1 \\ B_2 \end{bmatrix} = \begin{bmatrix} -1 & 0 \\ 0 & JJ^t - 1 \end{bmatrix} \begin{bmatrix} A_1 \\ A_2 \end{bmatrix} + \begin{bmatrix} 0 \\ \frac{1}{2} \sqrt{Z_{02}} J_0 e^{j\theta} J \end{bmatrix}. \quad (13)$$

The complete scattering matrix can be expressed as follows

$$\begin{cases} \begin{bmatrix} B_1 \\ B_2 \end{bmatrix} = \begin{bmatrix} -Hm - \frac{1-N2}{1+N2} Hd & \frac{2N}{1+N2} Hd \\ \frac{2N}{1+N2} Hd & -Hm - \frac{1-N2}{1+N2} Hd \end{bmatrix} \begin{bmatrix} A_1 \\ A_2 \end{bmatrix} & \text{On sub-domains metal and dielectric} \\ \begin{bmatrix} B_1 \\ B_2 \end{bmatrix} = \begin{bmatrix} -1 & 0 \\ 0 & JJ^t - 1 \end{bmatrix} \begin{bmatrix} A_1 \\ A_2 \end{bmatrix} + \begin{bmatrix} 0 \\ \frac{1}{2} \sqrt{Z_{02}} J_0 e^{j\theta} J \end{bmatrix} & \text{On sub-domain source} \end{cases}$$

At K^{th} iteration, it is possible to calculate the electric field and current density at interface plane:

$$J_i^k = \frac{1}{\sqrt{Z_{0i}}} (A_i^k - B_i^k) \quad (15)$$

$$E_i^k = \sqrt{Z_{0i}} (A_i^k + B_i^k). \quad (16)$$

IV- RESULTS AND DESIGN EXAMPLES

As an application, we are interested in characterizing two different shapes of patch antennas. We have developed a program to calculate the input impedance and the reflection coefficient of each antenna.

1. Rectangular patch antenna:

The first example is a rectangular patch antenna deposited on substrate with relative dielectric constant $\epsilon_r = 2.2$. The coaxial probe is attached to the patch antenna at (x_c, y_c) .

In this case, the circuit plane is meshed with 64x64 square cells.

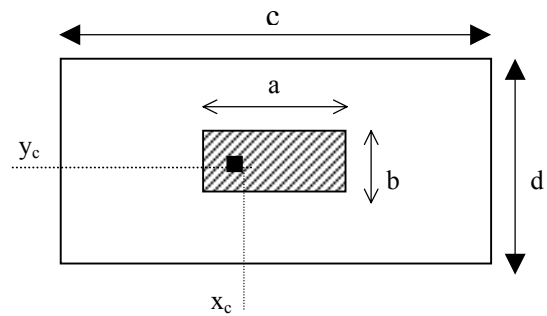


Figure 7. Rectangular patch antenna structure $c=100\text{mm}$, $d=76\text{mm}$, $a=25\text{mm}$, $b=19\text{mm}$, $x_c=45,5\text{mm}$, $y_c=34,5\text{mm}$, $\epsilon_r=2.2$.

First, the convergence of parameters is tested. In Fig. 8, The real part of Z_{in} is illustrated as function of the iteration number. It is seen that convergence is achieved for 160 iterations. The iterative process is terminated when the convergence is reached.

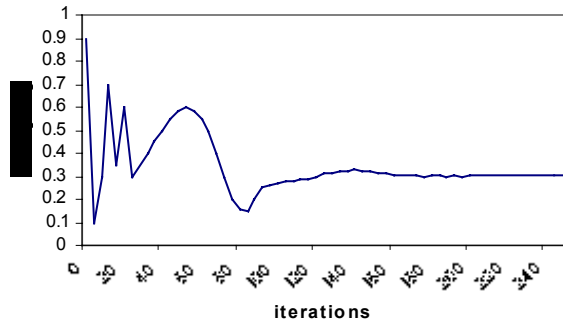


Figure 8: Real part of Z_{in} as function of the iteration number.

Figure 9. show the comparison between simulation and measured data reference [7]. It is seen that the error between them is 5 to 7%. The error can be minimized by meshing the structure with high resolution (128x128 pixels).

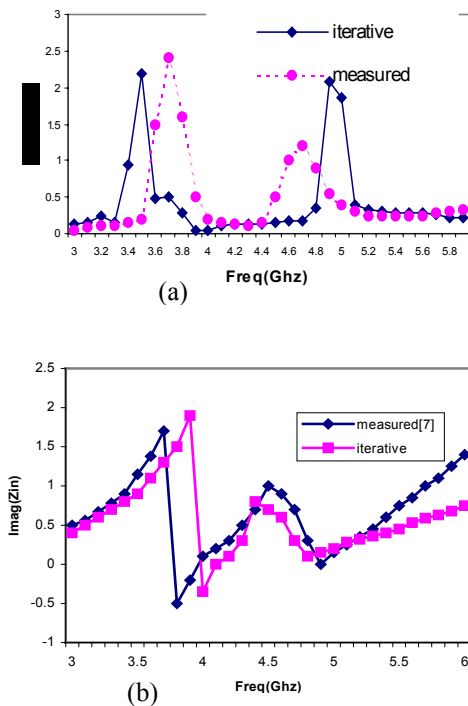


Figure 9. Input impedance of a rectangular patch antenna as a function of frequency, (a) real part and (b) imaginary part.

Figure 10 shows that the second resonance frequency is eliminated when the position of probe feed excitation is at the center of the patch antenna

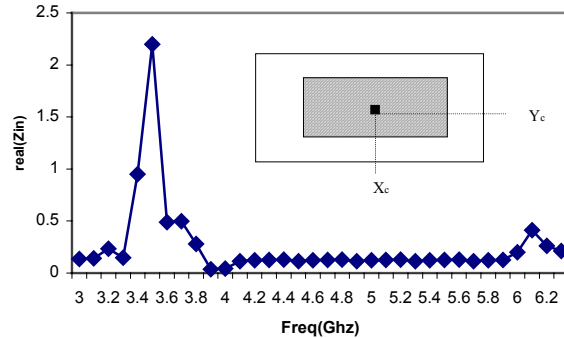
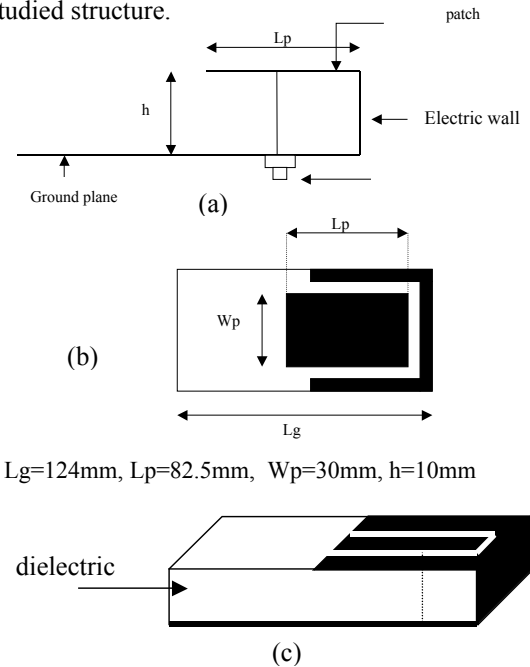


Figure 10. Input impedance of rectangular patch antenna $c=100\text{mm}$, $d=76\text{mm}$, $a=25\text{mm}$, $b=19\text{mm}$, $x_c=0$, $y_c=0$, $\epsilon_r=2.2$.

2. Patch Inverted-F Antenna (PIFA):

The antenna was printed on a thin, flexible Mylar substrate. The end of the ground plane is wrapped around the former, reducing the overall length of the antenna by the height without affecting the antenna performance.

Figure 11 shows the geometries and dimensions of the studied structure.



$L_g=124\text{mm}$, $L_p=82.5\text{mm}$, $W_p=30\text{mm}$, $h=10\text{mm}$

Figure 11. (a) Side view of the antenna (b) top view of the antenna (c) schematic view on the antenna.

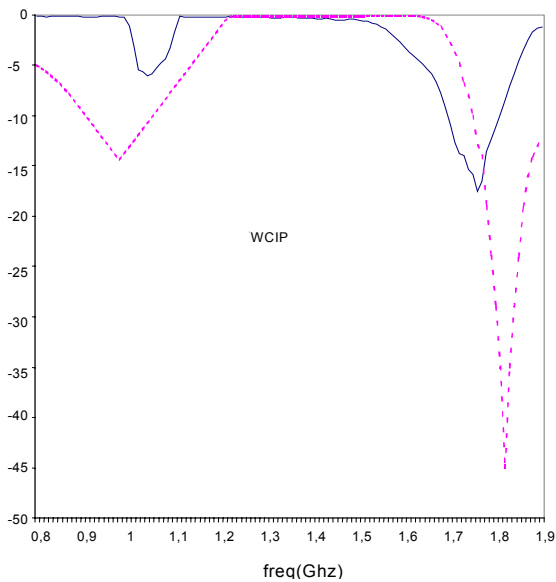


Figure 12. Reflection coefficient against frequency for the pifa antenna WCIP [8].

Finally the reflection coefficient is extracted and compared in Fig. 12 to the measured response given in reference [8], an agreement between them is observed.

IV- CONCLUSION

An iterative technique based on the concept of waves has been used for the simulation of the input impedance of rectangular patch antenna and the reflection coefficient of PIFA antenna. Thanks to its simplicity, the presented method does not involve bases functions and inversion of matrix. The good agreement between computed and published results justifies the design procedure and validates the present analysis approach. Consequently, the present approach will be investigated for further new applications such as air bridges, diodes, active elements.

REFERENCES

- [1] R. F. Harrington, "Field Computation by Moment Methods", New York, Macmillan, 1968.
- [2] O. Axelsson and V.A. Barker, "Finite Element Solution of boundary value problems", *Theory and Computation, New York, Academic Press*, 1984.
- [3] D. M. Sheen, S. M. D. Abouzahra, and J. A. Kong, "Application of the three-dimensional finite-difference time-domain method to the analysis of

planar micro-strip circuit", *IEEE, MTT*, vol.38, pp.849-857, July 1990.

- [4] M. Azizi, Boussouis, H. Aubert, H. Baudrand, "Three dimensional analysis of planar discontinuities by an iterative method". *Microwave and Optical Techniques Letters* 1996, 20:372-376.
- [5] A. Gharsallah, A. Gharbi, L. Desclos and H. Baudrand, "Analysis of interdigital capacitor and quasi-lumped miniaturized filters using iterative method," *Int. J. Numer. Model*, 2002. 15: 169-179. (DOI: 10,1002/jnm, 448)
- [6] A. Mami, H. Zairi, A. Gharsallah and H. Baudrand. "Analysis of micro-strip spiral inductor by using iterative method", *Microwave and optical technology Letters*. vol. 35, no. 4 , November 2002.
- [7] I. Proust, thesis, "Contribution à l'étude des discontinuités en guides d'ondes coaxiaux. Application aux antennes planaires", *INP Toulouse, France*, 1995.
- [8] K. F. Lee, Y. X. Guo, J. A. Hawkins, R. Chair and K. M. Luk. "Theory and experiment on microstrip patch antennas with shorting walls". *IEE Proc-Microwave Antennas propag.* vol. 147, no. 6, December 2000.
- [9] J. P. Damiano, A. Papiernik, "Survey of analytical and numerical models for probe-fed microstrip antennas", *IEE Proc. Microwave Antennas propag.*, vol. 141, no. 1, pp. 15-22, February 1994.
- [10] E. Lier, "Improved formulas for input impedance of coax-fed microstrip patch antennas" *IEE Proceeding*, vol. 129, no. 4, pp. 161-164, August 1992.



Hassen Zairi received his master's degree in physics from the Faculty of Sciences, Tunis, Tunisia, in 2002. He is currently working toward his PhD degree at the Faculty of Sciences, Tunis. His research interests include antenna

for wireless communication and microwave integrated circuits.



Ali Gharsallah received the degrees in radio-electrical engineering from the Ecole Supérieure de Télécommunication de Tunis in 1986 and the PhD degree in 1994 from the Ecole Nationale d'Ingénieurs de Tunis.

Since 1991, he was with the Department of Physics at the Faculty of Sciences, Tunis. His current research interests include antennas, multilayered structures and microwave integrated circuits.



Gharbi Abdelhafidh Professor in the Faculty of Sciences of Tunis, his current research interests are in the areas of dielectric and electromagnetic fields.



Baudrand Henri professor of Electromagnetism and microwave circuits at the Ecole Nationale Supérieure d'Electronique Electrotechnique Informatique of Toulouse, France. Baudrand is specialized in modelization of

passive and active circuits and antennas. He is the author and co-author of three books:

- Introduction au calcul des éléments de circuits microondes
- Optimisation des circuits non linéaires
- Calcul des circuits microondes par les schémas équivalents-exercices CEPADUES Editions). He co-signed over 100 publications in journals and 250 communication in international conferences.
- Dr Baudrand is a member of 'Electromagnetism Academy', senior member of IEE societies. President of URSI France commission B for 6 years (1993-1999), member and past president of IEEE-MTT-ED French chapter. He is a awarded officier des Palmes académiques, and Director Honoris causa of Iasi University, he is the Director of GREMO (Groupe de Recherche en Electromagnétisme et Microondes de Toulouse).

ACES COPYRIGHT FORM

This form is intended for original, previously unpublished manuscripts submitted to ACES periodicals and conference publications. The signed form, appropriately completed, MUST ACCOMPANY any paper in order to be published by ACES. PLEASE READ REVERSE SIDE OF THIS FORM FOR FURTHER DETAILS.

TITLE OF PAPER:

RETURN FORM TO:

Dr. Atef Z. Elsherbeni
University of Mississippi
Dept. of Electrical Engineering
Anderson Hall Box 13
University, MS 38677 USA

AUTHORS(S)

PUBLICATION TITLE/DATE:

PART A - COPYRIGHT TRANSFER FORM

(NOTE: Company or other forms may not be substituted for this form. U.S. Government employees whose work is not subject to copyright may so certify by signing Part B below. Authors whose work is subject to Crown Copyright may sign Part C overleaf).

The undersigned, desiring to publish the above paper in a publication of ACES, hereby transfer their copyrights in the above paper to The Applied Computational Electromagnetics Society (ACES). The undersigned hereby represents and warrants that the paper is original and that he/she is the author of the paper or otherwise has the power and authority to make and execute this assignment.

Returned Rights: In return for these rights, ACES hereby grants to the above authors, and the employers for whom the work was performed, royalty-free permission to:

1. Retain all proprietary rights other than copyright, such as patent rights.
2. Reuse all or portions of the above paper in other works.

3. Reproduce, or have reproduced, the above paper for the author's personal use or for internal company use provided that (a) the source and ACES copyright are indicated, (b) the copies are not used in a way that implies ACES endorsement of a product or service of an employer, and (c) the copies per se are not offered for sale.

4. Make limited distribution of all or portions of the above paper prior to publication.

5. In the case of work performed under U.S. Government contract, ACES grants the U.S. Government royalty-free permission to reproduce all or portions of the above paper, and to authorize others to do so, for U.S. Government purposes only.

ACES Obligations: In exercising its rights under copyright, ACES will make all reasonable efforts to act in the interests of the authors and employers as well as in its own interest. In particular, ACES REQUIRES that:

1. The consent of the first-named author be sought as a condition in granting re-publication permission to others.
2. The consent of the undersigned employer be obtained as a condition in granting permission to others to reuse all or portions of the paper for promotion or marketing purposes.

In the event the above paper is not accepted and published by ACES or is withdrawn by the author(s) before acceptance by ACES, this agreement becomes null and void.

AUTHORIZED SIGNATURE

TITLE (IF NOT AUTHOR)

EMPLOYER FOR WHOM WORK WAS PERFORMED

DATE FORM SIGNED

Part B - U.S. GOVERNMENT EMPLOYEE CERTIFICATION

(NOTE: if your work was performed under Government contract but you are not a Government employee, sign transfer form above and see item 5 under Returned Rights).

This certifies that all authors of the above paper are employees of the U.S. Government and performed this work as part of their employment and that the paper is therefor not subject to U.S. copyright protection.

AUTHORIZED SIGNATURE

TITLE (IF NOT AUTHOR)

NAME OF GOVERNMENT ORGANIZATION

DATE FORM SIGNED

PART C - CROWN COPYRIGHT

(NOTE: ACES recognizes and will honor Crown Copyright as it does U.S. Copyright. It is understood that, in asserting Crown Copyright, ACES in no way diminishes its rights as publisher. Sign only if ALL authors are subject to Crown Copyright).

This certifies that all authors of the above Paper are subject to Crown Copyright. (Appropriate documentation and instructions regarding form of Crown Copyright notice may be attached).

AUTHORIZED SIGNATURE

TITLE OF SIGNEE

NAME OF GOVERNMENT BRANCH

DATE FORM SIGNED

Information to Authors

ACES POLICY

ACES distributes its technical publications throughout the world, and it may be necessary to translate and abstract its publications, and articles contained therein, for inclusion in various compendiums and similar publications, etc. When an article is submitted for publication by ACES, acceptance of the article implies that ACES has the rights to do all of the things it normally does with such an article.

In connection with its publishing activities, it is the policy of ACES to own the copyrights in its technical publications, and to the contributions contained therein, in order to protect the interests of ACES, its authors and their employers, and at the same time to facilitate the appropriate re-use of this material by others.

The new United States copyright law requires that the transfer of copyrights in each contribution from the author to ACES be confirmed in writing. It is therefore necessary that you execute either Part A-Copyright Transfer Form or Part B-U.S. Government Employee Certification or Part C-Crown Copyright on this sheet and return it to the Managing Editor (or person who supplied this sheet) as promptly as possible.

CLEARANCE OF PAPERS

ACES must of necessity assume that materials presented at its meetings or submitted to its publications is properly available for general dissemination to the audiences these activities are organized to serve. It is the responsibility of the authors, not ACES, to determine whether disclosure of their material requires the prior consent of other parties and if so, to obtain it. Furthermore, ACES must assume that, if an author uses within his/her article previously published and/or copyrighted material that permission has been obtained for such use and that any required credit lines, copyright notices, etc. are duly noted.

AUTHOR/COMPANY RIGHTS

If you are employed and you prepared your paper as a part of your job, the rights to your paper initially rest with your employer. In that case, when you sign the copyright form, we assume you are authorized to do so by your employer and that your employer has consented to all of the terms and conditions of this form. If not, it should be signed by someone so authorized.

NOTE RE RETURNED RIGHTS: Just as ACES now requires a signed copyright transfer form in order to do "business as usual", it is the intent of this form to return rights to the author and employer so that they too may do "business as usual". If further clarification is required, please contact: The Managing Editor, R. W. Adler, Naval Postgraduate School, Code EC/AB, Monterey, CA, 93943, USA (408)656-2352.

Please note that, although authors are permitted to re-use all or portions of their ACES copyrighted material in other works, this does not include granting third party requests for reprinting, republishing, or other types of re-use.

JOINT AUTHORSHIP

For jointly authored papers, only one signature is required, but we assume all authors have been advised and have consented to the terms of this form.

U.S. GOVERNMENT EMPLOYEES

Authors who are U.S. Government employees are not required to sign the Copyright Transfer Form (Part A), but any co-authors outside the Government are.

Part B of the form is to be used instead of Part A only if all authors are U.S. Government employees and prepared the paper as part of their job.

NOTE RE GOVERNMENT CONTRACT WORK: Authors whose work was performed under a U.S. Government contract but who are not Government employees are required so sign Part A-Copyright Transfer Form. However, item 5 of the form returns reproduction rights to the U. S. Government when required, even though ACES copyright policy is in effect with respect to the reuse of material by the general public.

January 2002

INFORMATION FOR AUTHORS

PUBLICATION CRITERIA

Each paper is required to manifest some relation to applied computational electromagnetics. **Papers may address general issues in applied computational electromagnetics, or they may focus on specific applications, techniques, codes, or computational issues.** While the following list is not exhaustive, each paper will generally relate to at least one of these areas:

- 1. Code validation.** This is done using internal checks or experimental, analytical or other computational data. Measured data of potential utility to code validation efforts will also be considered for publication.
- 2. Code performance analysis.** This usually involves identification of numerical accuracy or other limitations, solution convergence, numerical and physical modeling error, and parameter tradeoffs. However, it is also permissible to address issues such as ease-of-use, set-up time, run time, special outputs, or other special features.
- 3. Computational studies of basic physics.** This involves using a code, algorithm, or computational technique to simulate reality in such a way that better, or new physical insight or understanding, is achieved.
- 4. New computational techniques,** or new applications for existing computational techniques or codes.
- 5. “Tricks of the trade”** in selecting and applying codes and techniques.
- 6. New codes, algorithms, code enhancement, and code fixes.** This category is self-explanatory, but includes significant changes to existing codes, such as applicability extensions, algorithm optimization, problem correction, limitation removal, or other performance improvement. **Note: Code (or algorithm) capability descriptions are not acceptable, unless they contain sufficient technical material to justify consideration.**
- 7. Code input/output issues.** This normally involves innovations in input (such as input geometry standardization, automatic mesh generation, or computer-aided design) or in output (whether it be tabular, graphical, statistical, Fourier-transformed, or otherwise signal-processed). Material dealing with input/output database management, output interpretation, or other input/output issues will also be considered for publication.
- 8. Computer hardware issues.** This is the category for analysis of hardware capabilities and limitations of various types of electromagnetics computational requirements. Vector and parallel computational techniques and implementation are of particular interest.

Applications of interest include, but are not limited to, antennas (and their electromagnetic environments), networks, static fields, radar cross section, shielding, radiation hazards, biological effects, electromagnetic pulse (EMP), electromagnetic interference (EMI), electromagnetic compatibility (EMC), power transmission, charge transport, dielectric, magnetic and nonlinear materials, microwave components, MEMS technology, MMIC technology, remote sensing and geometrical and physical optics, radar and communications systems, fiber optics, plasmas, particle accelerators, generators and motors, electromagnetic wave propagation, non-destructive evaluation, eddy currents, and inverse scattering.

Techniques of interest include frequency-domain and time-domain techniques, integral equation and differential equation techniques, diffraction theories, physical optics, moment methods, finite differences and finite element techniques, modal expansions, perturbation methods, and hybrid methods. This list is not exhaustive.

A unique feature of the Journal is the publication of unsuccessful efforts in applied computational electromagnetics. Publication of such material provides a means to discuss problem areas in electromagnetic modeling. Material representing an unsuccessful application or negative results in computational electromagnetics will be considered for publication only if a reasonable expectation of success (and a reasonable effort) are reflected. Moreover, such material must represent a problem area of potential interest to the ACES membership.

Where possible and appropriate, authors are required to provide statements of quantitative accuracy for measured and/or computed data. This issue is discussed in “Accuracy & Publication: Requiring, quantitative accuracy statements to accompany data,” by E. K. Miller, *ACES Newsletter*, Vol. 9, No. 3, pp. 23-29, 1994, ISBN 1056-9170.

EDITORIAL REVIEW

In order to ensure an appropriate level of quality control, papers are peer reviewed. They are reviewed both for technical correctness and for adherence to the listed guidelines regarding information content.

JOURNAL CAMERA-READY SUBMISSION DATES

March issue	deadline 8 January
July issue	deadline 20 May
November issue	deadline 20 September

Uploading an acceptable camera-ready article after the deadlines will result in a delay in publishing this article.

STYLE FOR CAMERA-READY COPY

The ACES Journal is flexible, within reason, in regard to style. However, certain requirements are in effect:

1. The paper title should NOT be placed on a separate page. The title, author(s), abstract, and (space permitting) beginning of the paper itself should all be on the first page. The title, author(s), and author affiliations should be centered (center-justified) on the first page.
2. An abstract is REQUIRED. The abstract should be a brief summary of the work described in the paper. It should state the computer codes, computational techniques, and applications discussed in the paper (as applicable) and should otherwise be usable by technical abstracting and indexing services.
3. Either British English or American English spellings may be used, provided that each word is spelled consistently throughout the paper.
4. Any commonly-accepted format for referencing is permitted, provided that internal consistency of format is maintained. As a guideline for authors who have no other preference, we recommend that references be given by author(s) name and year in the body of the paper (with alphabetical listing of all references at the end of the paper). Titles of Journals, monographs, and similar publications should be in italic font or should be underlined. Titles of papers or articles should be in quotation marks.
5. Internal consistency shall also be maintained for other elements of style, such as equation numbering. As a guideline for authors who have no other preference, we suggest that equation numbers be placed in parentheses at the right column margin.
6. The intent and meaning of all text must be clear. For authors who are NOT masters of the English language, the ACES Editorial Staff will provide assistance with grammar (subject to clarity of intent and meaning).
7. Unused space should be minimized. Sections and subsections should not normally begin on a new page.

PAPER FORMAT

The preferred format for initial submission and camera-ready manuscripts is 12 point Times Roman font, single line spacing and double column format, similar to that used here, with top, bottom, left, and right 1 inch margins. Manuscripts should be prepared on standard 8.5x11 inch paper.

Only camera-ready electronic files are accepted for publication. The term “**camera-ready**” means that the material is neat, legible, and reproducible. Full details can be found on ACES site, Journal section.

ACES reserves the right to edit any uploaded material, however, this is not generally done. It is the author(s)

responsibility to provide acceptable camera-ready pdf files. Incompatible or incomplete pdf files will not be processed, and authors will be requested to re-upload a revised acceptable version.

SUBMITTAL PROCEDURE

All submissions should be uploaded to ACES server through ACES web site (<http://aces.ee.olemiss.edu>) by using the upload button, journal section. Only pdf files are accepted for submission. The file size should not be larger than 5MB, otherwise permission from the Editor-in-Chief should be obtained first. The Editor-in-Chief will acknowledge the electronic submission after the upload process is successfully completed.

COPYRIGHTS AND RELEASES

Each primary author must sign a copyright form and obtain a release from his/her organization vesting the copyright with ACES. Copyright forms are available at ACES, web site (<http://aces.ee.olemiss.edu>). To shorten the review process time, the executed copyright form should be forwarded to the Editor-in-Chief immediately after the completion of the upload (electronic submission) process. Both the author and his/her organization are allowed to use the copyrighted material freely for their own private purposes.

Permission is granted to quote short passages and reproduce figures and tables from and ACES Journal issue provided the source is cited. Copies of ACES Journal articles may be made in accordance with usage permitted by Sections 107 or 108 of the U.S. Copyright Law. This consent does not extend to other kinds of copying, such as for general distribution, for advertising or promotional purposes, for creating new collective works, or for resale. The reproduction of multiple copies and the use of articles or extracts for commercial purposes require the consent of the author and specific permission from ACES. Institutional members are allowed to copy any ACES Journal issue for their internal distribution only.

PUBLICATION CHARGES

ACES members are allowed 12 printed pages per paper without charge; non-members are allowed 8 printed pages per paper without charge. Mandatory page charges of \$75 a page apply to all pages in excess of 12 for members or 8 for non-members. Voluntary page charges are requested for the free (12 or 8) pages, but are NOT mandatory or required for publication. A priority courtesy guideline, which favors members, applies to paper backlogs. Authors are entitled to 15 free reprints of their articles and must request these from the Managing Editor. Additional reprints are available to authors, and reprints available to non-authors, for a nominal fee.

ACES Journal is abstracted in INSPEC, in Engineering Index, and in DTIC.